CZECH TECHNICAL UNIVERSITY IN PRAGUE

Faculty of Nuclear Sciences and Physical Engineering

Department of Physics

Master's thesis

Analysis of b-Jets in p+Pb collisions at 5 TeV

Bc. Lukáš Kramárik

Supervisor: Mgr. Jaroslav Bielčík, Ph.D.

Prague, 2016

ČESKÉ VYSOKÉ UČENÍ TECHNICKÉ
V PRAZE
Fakulta Jaderná a Fyzikálně Inženýrská
Katedra Fyziky

Diplomová práce

Analýza b-jetů v p+Pb srážkách s energií 5 TeV

Bc. Lukáš Kramárik

Vedoucí práce: Mgr. Jaroslav Bielčík, Ph.D.

Praha, 2016

Prehlásenie

Prehlasujem, že som svoju diplomovú prácu vypracoval samostatne a použil som len podklady (literatúru, publikácie, projekty, software a iné) uvedené v priloženom zozname.

Nemám závažný dôvod proti použitiu tohoto školského diela v zmysle §60 Zákona č.121/1200Sb., o autorskom práve, o právach súvisiacich s autorským právom a o zmene niektorých zákonov (autorský zákon).

V Prahe dňa

Acknowledgement

I would like to express my gratitude to my supervisor Mgr. Jaroslav Bielčík, Ph.D. for his guidance and useful comments which greatly helped to produce not only this thesis, but the whole analysis and to Elena Bruna, Ph.D. for her patience and unvaluable help and discussions. I would like to thank the Faculty of Nuclear Sciences and Physical Engineering (FNSPE) of CTU Prague for their support through my studies, and to the whole collective of students and colleagues not only for unambiguous help anytime it was needed, but also for creating friendly and funny environment.

Last but not least, special thanks go to my parents Helena and Anton, my girlfriend Lenka, brother Matúš and the whole family for their continuous support not only during my studies. I could not have done this without the encouragement and patience of them all. *Ďakujem za všetko.*

Názov práce: **Analýza b-jetů v p+Pb srážkách s energií 5 TeV**
Autor: Bc. Lukáš Kramárik

Odbor: Experimentální jaderná a částicová fyzika
Druh práce: Diplomová práce
Vedúci práce: Mgr. Jaroslav Bielčík, Ph.D.
Katedra fyziky, Fakulta jaderná a fyzikálně inženýrská,
České vysoké učení technické v Praze

Abstrakt:

Hustá a horúca jadrová hmota, kvarkovo-gluónová plazma, môže byť vytvorená v ultrarelativistických jadrových zrážkach. Ťažké kvarky, pôvabný c a krásny b, prechádzajú touto hmotou a testujú ju už od jej vzniku. Práve preto sú tieto kvarky výbornou soundou na štúdium vlastností tejto hmoty. Hlavným cieľom tejto práce je vyhľadávanie jetov z fragmentácie b kvarku. Na to sa využíva veľká doba života, veľká hmota B hadrónov a vysoký počet častíc z ich rozpadov. Takisto ukážeme vlastnosti algoritmu vyhľadávajúceho b jety použitím vlastností druhotných vrcholov v p-Pb zrážkach pri energií $\sqrt{s_{\rm NN}} = 5.02$ TeV zmeraných na experimente ALICE v CERN. Získali sme čistotu označenej vzorky. Spolu s efektivitou algoritmu sú použité na výpočet zlomku b-jetov v p-Pb zrážkach, ktorý bol na základe našich meraní stanovenný ako 1-6% pre jety priečnou hybnosťou od 20 GeV/c do 60 GeV/c.

Kľúčové slová: kvarkovo-gluónová plazma, druhotný vrchol, jet, b-jet, ALICE, LHC

Title: **Analysis of b-Jets in p+Pb collisions at 5 TeV**
Author: Bc. Lukáš Kramárik

Field of study: Experimental Nuclear and Particle Physics
Type of project: Master's thesis
Supervisor: Mgr. Jaroslav Bielčík, Ph.D.
Faculty of Nuclear Sciences and Physical Engineering,
Czech Technical University in Prague

Abstract:

In ultrarelativistic heavy-ion collisions, the hot and dense medium, the quark-gluon plasma, is created. Heavy quarks, charm and beauty, pass through created medium and probe it from early phases. Therefore, they are a great tool to study medium properties. The main goal of this thesis is to identify jets from b quark fragmentation. Search of b-jets exploits from long lifetime, large multiplicity of decay products and large mass of beauty hadron. Performance of the b-tagging algorithm based on properties of the secondary vertices in p-Pb collisions at $\sqrt{s_{\rm NN}} = 5.02$ TeV measured by the ALICE in CERN is studied. Purity of b-jets in tagged sample is extracted by template fits. Efficiency and purity of the tagger are used for calculation of b-jet fraction in p-Pb, that is determined to be 1-6% for jets with transverse momentum from 20 GeV/c to 60 GeV/c.

Keywords: quark-gluon plasma, secondary vertex, jet, b-jet, ALICE, LHC

Contents

List of Figures

List of Tables

Preface

The main goal of physicists involved in basic research is to solve the fundamental problems, such as what are the smallest elements of matter and their interactions or how universe was created. Over the past decades, not only different particle species, but also the new state of hot and dense nuclear matter, the quark-gluon plasma (QGP), have been studied by collider experiments. This state most likely existed shortly after the Big Bang and it is investigated by laboratories, that are able to collide ultrarelativistic heavy ions, since large energy is needed for its creation. Understanding properties of the QGP could as well result in more precise theoretical description of the strong interaction of elementary particles and of their creation.

The topic of this thesis is heavy-flavour probe of the QGP. Jets, collimated sprays of hadron, resulting from fragmentation of heavy b quark, may provide information about the in-medium scatterings, energy losses and other properties of the QGP. Heavy quarks are not created as an effect of the medium, they are created in early phases of the collisions, thus they test the medium in all of the stages. To quantitative understanding of its properties, reference studies in hadron-nucleus and hadron-hadron collisions are needed. In addition, hadron-nucleus collisions study interesting effect of the Cold Nuclear Matter. Identification of b-jets could be done by algorithms exploiting properties of beauty decays, occurring in displaced vertices.

At the LHC (Large Hadron Collider) in CERN, the first results from b-jet studies measurements in pp, p-Pb and Pb-Pb collisions for high jet transverse momentum region have been published by the CMS (Compact Muon Solenoid) experiment. However, due to calorimeter limitations and smaller recorded data sample at ALICE (A Large Ion Collider Experiment) detector, ALICE collaboration has not yet completed any b-jet spectra, b-jet suppression or b-jet fraction measurements. The aim of the ALICE is to extend CMS results towards smaller transverse momentum ranges than those at the CMS. The goal of this thesis is to present detailed performance of the secondary vertex b tagging algorithm and first results of b-jet fraction in p-Pb collisions at $\sqrt{s_{\mathrm{NN}}} = 5.02$ TeV recorded by the ALICE experiment.

In the first chapter, very short introduction to particle physics and its experimental goals and possible near-future discoveries is presented. The next chapter describes the ALICE experiment at the LHC. Performance of detection systems involved in our study during Run 1 is shortly discussed, together with short summary of the upgrades of the system before and after the Run 2.

The ALICE experiment is dedicated to test QCD matter in extreme condition of heavy-ion collisions. The QGP, created in such collisions is described in Chapter 3. This matter is not studied only at the LHC experiments, but also at, for example, experiments at the RHIC (Relativistic Heavy Ion Collider) in BNL (Brookhaven National Laboratory). Experiments in CERN and BNL measured many evidences of existence of the QGP, few of them are shown in this chapter.

Nowadays, there are no doubts about the existence of the QGP. However, many of its properties have not yet been satisfyingly experimentally investigated, thus studies of large number of experimental probes are ongoing. As already mentioned, heavy-flavour is the very important one. Few heavy-flavour experimental results from various experiments are shown in Chapter 4.

Then, jets, used for studying several QCD aspects in hadronic and nucleus collisions, and algorithm reconstructing them are presented. In addition, algorithms tagging b-jets used at the LHC and more particularly in our analysis are described. Study completed by the CMS, using algorithm tagging b-jets by secondary vertices, is as well referred. Analysis steps in this analysis are nearly the same, as in our performance study.

Finally, analysis of b-jets at the ALICE experiment, performed by the author of this thesis, is presented in the last chapter. Performance of secondary vertex tagging algorithm in p-Pb collisions is shown for different selection criteria. Three samples, tagged by different criteria are used for further studies of b purity in these samples. All of the steps in this study are controlled by performing the same steps in the simulations of collisions. The main result, the b-jet fraction in p-Pb collisions, and stability of its measurements are discussed.

Chapter 1

Introduction to particle physics

Nuclear and particle physics are disciplines on the cutting edge of human knowledge not only from point of view of theories describing them, but also from the technological one. In order to be confirmed or denied, many theories need large, but very fast and precise machines. Many phenomena are not successfully understood, such as dark matter and dark energy, and need both new theory and new experiment.

Nowadays, the most relevant theory to study elementary particles and interactions is the Standard Model. It was formed in 1970s and it has already been experimentally confirmed. This theory describes particles forming matter (leptons and quarks) and carriers of fundamental interactions, gauge bosons. In addition, Higgs mechanism generating mass of W^+, W^-, Z^0 bosons and photon γ is included in the Standard Model.

The theory describing interaction of charged particles between each other and with electromagnetic field is quantum electrodynamics (QED). Each of such interactions can be described by series of processes, in which photons are exchanged. Photon is one of the bosons and it has no mass or charge, so it propagates freely and photons do not interact between each other. This is why the range of electromagnetic interaction is theoretically infinite. Every particle could have positive, negative or zero charge. Charged particles are influenced by magnetic field, it can be observed as curvature of their trajectories. Photon is an energy quantum, that can be radiated in different processes, where particles lose energy or dramatically change their flight directions (Compton scattering, Bremsstrahlung).

In case of weak interaction, intermediate particles are W^+, W^- and Z^0 bosons. Because of their relatively large masses ($M_{W^\pm} = 80.385 \pm 0.015$ GeV/c^2 [1] and $M_{Z^0} = 91.1876 \pm 0.0021$ GeV/c^2 [1]), the range of this interaction is quite short, approximately 1000 times smaller than the dimension of nucleus ($\sim$1 fm). Actually, in case of low-energy collision, their range is considered negligible. In interactions via charged currents (where $W^\pm$ are propagated), the particle transformations can occur. However, these transformations should conserve number of leptons and also other symmetries. Examples of processes, where one lepton is transformed to another, are β-decays.

Weak and electromagnetic interactions are together described by Glashow-Weinberg-Salam (GWS) standard model of electroweak interactions. In this theory, the bosons, that have already been mentioned, are quanta of physical vector fields, constructed of the four Yang-Mills fields associated with generators of $SU(2) \times U(1)$ symmetry group. In GWS theory, these quanta interact not only together, but also with basic building blocks of matter - leptons (electron e^- , muon μ^-, tau particle τ^- and three corresponding neutrinos ν_e, ν_μ, ν_τ - their properties are in Table 1.2) and quarks (u, d, s, c, b, t - their properties are in Table 1.1). Leptons and quarks are fermions and they are divided in three generations (families). Every lepton family (lepton and corresponding neutrino) have its own lepton number, that should be conserved in all types of interactions.

q	m [MeV/c^2]	Q [e]
u	$2.3^{+0.7}_{-0.5}$	$^2/_3$
d	$4.8^{+0.5}_{-0.3}$	-$^1/_3$
s	95 ± 5	-$^1/_3$
c	1275 ± 25	$^2/_3$
b	4180 ± 30	-$^1/_3$
t	173210 ± 710	$^2/_3$

Table 1.1: Basic properties of quarks q, their mass m and electric charge Q. Data taken from Ref. [1].

l	m [eV/c^2]	Q [e]
e^-	510 998.928 ± 0.011	-1
ν_e	<2	0
μ^-	105 658 371.5 ± 3.5	-1
ν_μ	<2	0
τ^-	1 776 820 000 ± 160 000	-1
ν_τ	<2	0

Table 1.2: Basic properties of leptons l, their mass m and electric charge Q. Data taken from Ref. [1].

General consensus is, that neutrinos have no electric charge and their mass is non-zero for most-likely at least 2 of them, but smaller than 2 eV/c^2. Other leptons have electric charge -1. For every particle of matter, theory describes corresponding antiparticle from antimatter. Antiparticles and particles have opposite charge, but their mass is the same. First experimentally discovered antiparticle was positron - in 1932, Carl D. Anderson observed the track in cloud chamber placed in the magnetic field. Curvature of this track corresponded to the opposite charge, but the same mass as that of an electron.

Last but not least, another basic principle of the GWS standard model is the Higgs mechanism. It generates masses of bosons in the Standard Model. This mechanism is assured by the Higgs boson, the last experimentally approved particle of the Standard Model (in 2012). Higgs boson is a massive scalar particle. Its measured mass is $M_{H^0} = 125.09 \pm 0.24$ GeV/c^2 [2]. Its mass, as well as its measured cross section, could help to construct other theories than the Standard Model theory, such as the Supersymmetry [3].

Figure 1.1 shows the most recent combined results of Higgs mass measurement with the ATLAS and the CMS. In these results, the signal strength μ, used to compare the Standard Model prediction and experimental results, is plotted for Higgs masses resulting from different analysis. μ is defined as fraction of multiplicated cross section σ and branching fraction (BF) from experiment and from Standard Model prediction,

$$\mu = \frac{\sigma_{\text{expt}} \times \text{BF}_{\text{expt}}}{\sigma_{\text{SM}} \times \text{BF}_{\text{SM}}}. \tag{1.1}$$

Decays of Higgs $H \rightarrow \gamma\gamma$ and $H \rightarrow ZZ \rightarrow 4l$ (4 leptons) are considered, with minimal reliance on the Standard Model. Nevertheless, results of the CMS and the ATLAS are consistent, and combined μ is close to the Standard Model prediction.

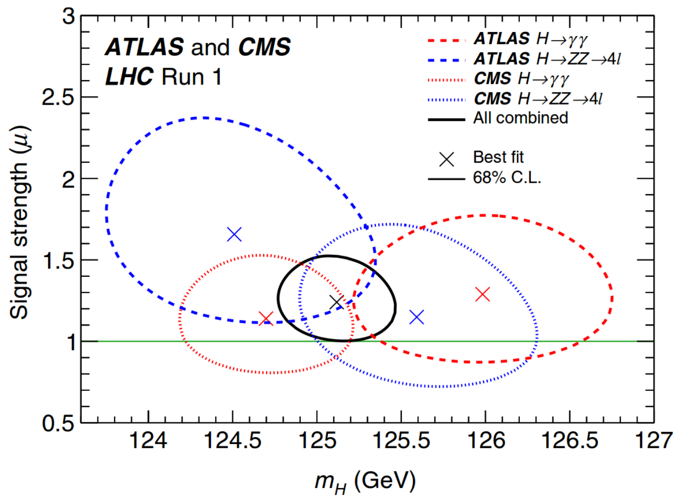

Figure 1.1: Summary of likelihood scans in the 2D plane of signal strength μ versus Higgs boson mass m_H for the ATLAS and CMS experiments. The 68% C.L. confidence regions (1 standard deviation σ) of the individual measurements are shown by the dashed curves and of the overall combination by the solid curve. The markers indicate the respective best-fit values. The SM signal strength is indicated by the horizontal line at $\mu = 1$. Taken from Ref. [2].

Another interaction described by the Standard Model is the strong interaction, described by quantum chromodynamics theory (QCD). This theory is based on $SU(3)$ symmetry group, thus 8 generators (mediators of interactions) are needed. These are 8 gluons of different so-called color charge. Other elementary particles that have color charge are quarks. Three different color charges of quarks are red, green and blue, for antiquarks it is antired, antigreen and antiblue. As gluons connect quarks, they can have different combinations of color and anticolor (for example red-antired, green-antiblue). One of color charge consequence is self-interaction of gluons.

One of the most important properties of strong interaction is asymptotic freedom. When two quarks are binded by gluons, energy of this binding rises with their mutual distance. For small distance, quarks are quasi free. If energy is provided to this binding, quarks are drawn apart from each other. If the provided energy rises, in some moment it is more energetically profitable to create new pair of quark and antiquark from vacuum. Matter, in which this dependency occurs, is called confined nuclear matter. However, the in the case of a very large energy density or temperature ($\approx$ 170 MeV), this binding is "melted" and quarks and gluons are free. This kind of matter is called deconfined nuclear matter, and example of it is the quark-gluon plasma (QGP).

In confined nuclear matter, quarks are binded by gluons to form hadrons. All hadrons are composed in such way, that they have no color charge (so they are "white"). In the case of mesons, hadrons composed from two quarks, this is done by binding of quark with color and antiquark with corresponding anticolor. In the case of baryons, composed from three quarks, these should have red, green and blue color charge. For antibaryons, quarks are replaced by antiquarks and color is replaced by anticolor, so antiquarks should have antired, antigreen and antiblue color charge.

Despite the described fact of confinement of quarks and antiquarks in mesons and baryons, states with more then three quarks and antiquarks have been predicted. These states were firstly theoretically predicted by Gell-Mann [4] and Zweig [5] in 1964. Predicted composition of tetraquark is two quarks and two antiquarks, in the case of pentaquarks it is 4 quarks and 1 antiquark. One of the most recent experimental observations of pentaquarks was in 2015 at the LHCb experiment in CERN [6]. Pentaquarks were observed in decays of baryon $\Lambda_b^0 \to J/\psi K^- p$.

Figure 1.2 (Left) shows Feynman diagram for dominant contribution to this decay, via resonance $\Lambda^* \to K^- p$, in Fig. 1.2 (Right), the exotic contribution is displayed. The exotic one has contribution of pentaquark resonance, composed from d, c, $\bar{c}$ and two u quarks. This resonance decays to J/ψ and p, so it is measured in the spectra of the combination of their invariant masses. Fit of this spectrum, as well as fitted spectrum of invariant mass of pair K^- p are shown in Fig. 1.3. For the most satisfactory description of data, two P_c^+ states are needed: $\mathrm{P}_c(4450)^+$ with mass $4449.8 \pm 1.7(\mathrm{stat.}) \pm 2.5(\mathrm{syst.})$ MeV and $\mathrm{P}_c(4380)^+$ with mass $4380 \pm 8(\mathrm{stat.}) \pm 29(\mathrm{syst.})$ MeV. Quarks in pentaquarks can be tightly bound, or they can form a meson-baryon molecule. More studies are needed to distinguish between these two options.

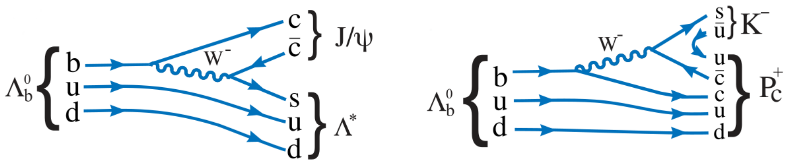

Figure 1.2: Feynman diagrams for $\Lambda_\mathrm{b}^0 \to J/\psi\Lambda^*$ (Left) and $\Lambda_\mathrm{b}^0 \to P_c^+ K^- p$ (Right) decay. Taken from Ref. [6].

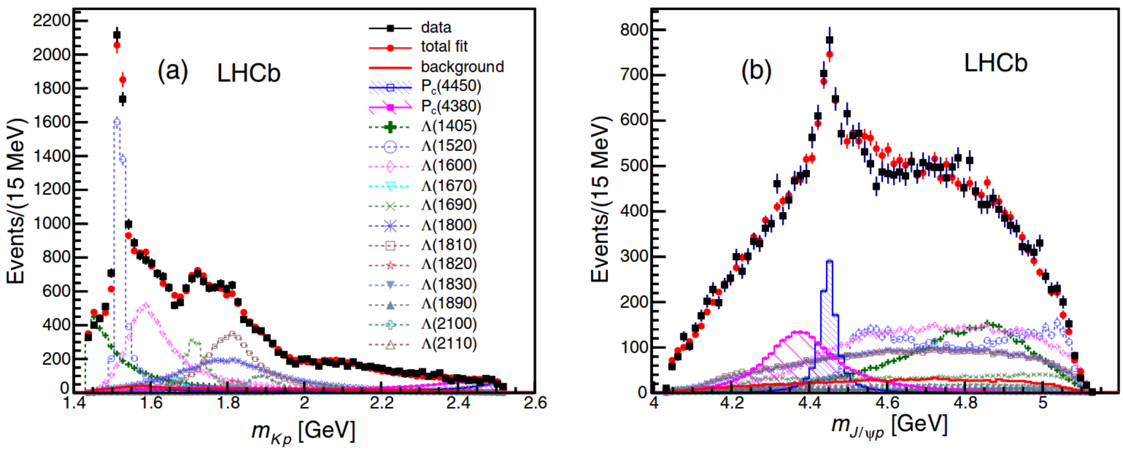

Figure 1.3: Fit projections for invariant mass of K^- p, m_{Kp} (Left) and J/ψ p, $m_{J/\psi p}$ (Right) with two P_c^+ states. The data are shown as solid (black) squares, while the solid (red) points show the results of the fit. The solid (red) histogram shows the background distribution. The (blue) open squares with the shaded histogram represent the $P_c(4450)^+$ state, and the shaded histogram topped with (purple) filled squares represents the $P_c(4380)^+$ state. Each Λ^* model component is also shown. The error bars on the points showing the fit results are due to simulation statistics. Taken from Ref. [6].

One of the problems in Standard Model is, that it does not describe gravitational force. Between two elementary particles, it is too small to be currently measured. It is expected to be intermediated by particle called graviton. Graviton is probably massless particle, propagating by speed of light (same as photon) with spin 2. At CERN, AEGIS (Antihydrogen Experiment: Gravity, Interferometry, Spectroscopy) [7] was built to study

Earth's gravitational acceleration on antihydrogen. Antihydrogen beam is splitted into parallel rays and after travelling given distance, they annihilate on matter. Positions of points of annihilation are measured and form a pattern, that is compared with the pattern of parallel rays created at the beginning. From this comparison, the drop of antihydrogen atoms during their flight is estimated.

New particles and states of matter are studied in high energy particle colliders, few of which were already mentioned. Over the past decades, wide range of innovations in electronics and technologies resulted in large increase in energy and luminosity in accelerators. At the present time, the biggest particle collider is the Large Hadron Collider (LHC) (described in Chapter 2) in CERN, that is planned to be upgraded to the High Luminosity (HL) LHC [8] in 2024. Later, the Future Circular Collider (FCC) [9], post-LHC accelerator in CERN, with circumference of 80 km to 100 km is planned to be built and will be capable to reach energy approximately 8 times higher than the current LHC. It will be able to collide protons with protons, electrons with positrons and also, maybe, hadrons with electrons.

To study the same physics as the LHC, but from a different perspective, the Compact Linear Collider (CLIC) [10] is planned to be built in CERN. It will accelerate and collide electrons with positrons at the energy of few TeV (current plan is 3 TeV). Another electron-positron linear accelerator, the International Linear Collider (ILC) [11], is going to be built in Japan, but with lower collision energy at the level of 200 - 500 GeV (extensible to 1 TeV). Physicist in China proposed to built the Circular Electron Positron Collider (CEPC) [12] as a Higgs Factory, with collision energy at the level of 240 GeV. It could be upgraded to an at least 70 TeV or higher proton-proton collider SppC [12].

In 2015 US Nuclear Physics Long Range Plan, the EIC (Electron-Ion Collider) was selected as number one priority for new facility with aim to study new QCD frontier. Its main goals are measurement of space distribution of spins of sea quarks and gluons, saturation density of gluons or effect of nuclei on the distribution and interaction of quarks and gluons. It construction will start in 2025 in the USA.

All of these experiments will be able to study physics beyond Standard Model and explore new states of matter such as dark matter, dark energy, or different states of nuclear matter, mentioned in Chapter 3.

Chapter 2

The ALICE experiment at the CERN LHC

Nowadays, a major part of activities in particle physics is concentrated at the LHC (Large Hadron Collider) in CERN (Conseil Européen pour la Recherche Nucléaire - the European Organization for Nuclear Research). One of the detectors situated at the LHC is ALICE (A Large Ion Collider Experiment) [13]. Its main goals are studies of QCD matter, that could be created in high-energy collisions of heavy ions. There are six other detectors at the LHC. The general purpose ones are the ATLAS (A Toroidal LHC ApparatuS) [14] and the CMS (Compact Muon Solenoid) [15]. LHCb experiment [16] is especially designed to study beauty and cause of different amount of matter and antimatter in universe. The smallest and the most specialized experiments at the LHC are the TOTEM (Total, elastic and diffractive cross-section measurement) [17], the LHCf [18] and the MoEDAL (Monopole and Exotics Detector at the LHC) [19].

2.1 Large Hadron Collider

LHC has the form of 27 km long circuit and it is a part of the large accelerating complex (Fig. 2.1), that enables cutting-edge studies in particle and nuclear physics. The main purposes of research at the LHC are studies of Higgs boson, Supersymmetry, extra dimension, quark-gluon plasma, dark matter, dark energy and much more. Accelerating complex in CERN is displayed in Fig. 2.1. Currently, it enables acceleration of protons or Pb ions (nuclei). Before injection into the LHC, protons and ions should be accelerated by the chain of accelerators. The source of lead-ion is pure lead that weighs 500 mg, heated to about 500°C to vaporize a small number of atoms. Electrons are removed from vaporized atoms with an electrical current, and then the created ions are injected to Linac 3. Then they are injected in LIER (The Low Energy Ion Ring). The source of protons is situated at the Linac 2, where electrons are stripped from atoms and protons are accelerated to the energy of 50 MeV. Then, they are injected into PSB (Proton Synchrotron Booster). Both protons are ions are subsequently accelerated by PS (Proton Synchrotron), SPS (Super Proton Synchrotron) and finally by the LHC.

LHC operates in different phases. Phase called Run is the working phase, when collisions and measurements occur. During phase called Long Shutdown (LS) there are no collisions, and the LHC is being upgraded or repaired. In Run 1 (2010-2013), there were collisions of protons (pp) at maximum energy of collision $\sqrt{s} = 8$ TeV [1], Pb nuclei (Pb-Pb)

[1] $\sqrt{s}$ is total energy of collision in CMS (center-of-mass frame).

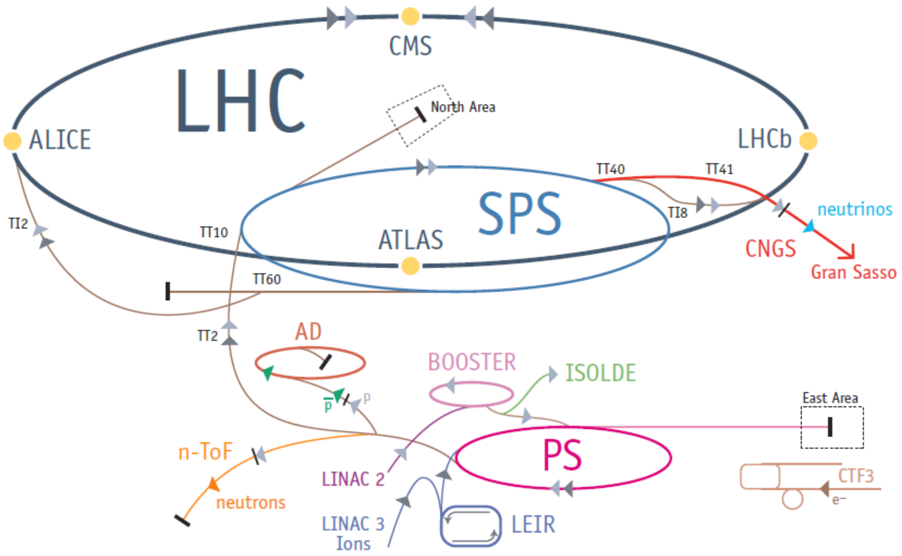

Figure 2.1: Accelerator complex in CERN. Taken from Ref. [20].

at maximum energy per colliding nucleon pair $\sqrt{s_{NN}} = 2.76$ TeV [2] and protons with Pb nuclei (p-Pb) at $\sqrt{s_{NN}} = 5.02$ TeV. More detailed properties of beam and collisions at the LHC are in Table 2.1. Since the first collisions at LHC in 2009, the progressive grow of energy of collisions and luminosity delivered by LHC could be observed. During Run 1, bunch spacing was at 50 ns.

Year	**Mode**	$\sqrt{s_{NN}}$ **[TeV]**	**Delivered** $\mathcal{L}$
2009	pp	0.9	19.6 μb^{-1}
2009	pp	2.36	0.87 μb^{-1}
2010	pp	7	0.5 pb^{-1}
2010	Pb-Pb	2.76	9 μb^{-1}
2011	pp	2.76	46 nb^{-1}
2011	pp	7	4.9 pb^{-1}
2011	Pb-Pb	2.76	146 μb^{-1}
2012	pp	8	9.7 pb^{-1}
2012	p-Pb	5.02	1.5 μb^{-1}
2013	p-Pb	5.02	32 nb^{-1}
2013	pp	2.76	129 nb^{-1}

Table 2.1: Summary of beam parameters (collision system mode, energy of collision $\sqrt{s_{NN}}$ and integrated luminosity delivered by the LHC $\mathcal{L}$) during the first four years (Run 1) of the LHC operation. Taken from Ref. [21]

In Run 2, that has begun in 2015, collision systems are the same and the energies are nearly doubled. Also bunch spacing is planned to fall down to 25 ns. The first collisions of protons in 2015 were at $\sqrt{s} = 13$ TeV. For Pb-Pb collisions in November 2015, energy was $\sqrt{s_{NN}} = 5.02$ TeV. In the end of April 2016, the new period with pp collisions started and it is planned till November 2016, when p-Pb collisions at record energies ($\sqrt{s_{NN}} = 5.02$ TeV to 8.2 TeV, the decision has not yet been taken in time of writing this thesis) are sheduled. The Run 2 phase, that finishes in 2018, is followed by LS 2. Run 3 phase is currently

[2] $\sqrt{s_{\rm NN}}$ is total energy of collision per nucleon pair in nucleus-nucleus collisions in CMS.

planned between years 2021 and 2024.

2.2 ALICE detector

The goal of the ALICE detector (Fig. 2.2) is to study different phases of nuclear matter, such as hot nuclear matter (QGP) or cold nuclear matter, and the phase transition between QGP and hadronic matter. This detector consists of 18 different subdetectors, that are specialized on detection of low energy particles and jets with very high energy, momentum and space resolution. Central barrel of detector is enclosed in solenoid producing magnetic field of 0.5 T. The largest detectors in central barrel, from the closest to the furthest, with regards to the beam pipe are Inner Tracking System (ITS), Time-Projection Chamber (TPC), Time-of-Flight (TOF), Ring Imaging Cherenkov (RICH), High Momentum Particle IDentification (HMPID), Transition Radiation Detector (TRD), ElectroMagnetic Calorimeter (EMCal), Di-Jet Calorimeter (DCal) and PHOton Spectrometer (PHOS). In a forward beam direction there are systems for muon detection, partially enclosed in dipole magnet. Zero Degree Calorimeter (ZDC) measures amount of nucleons, that did not participate in collisions and it is situated 116 m from the interaction point. Some of subdetectors, that are the most important for our studies, will be introduced. Description is focused on performance during Run 1, however, upgrades for Run 2 are shortly discussed. Data concerning performance of the ALICE detector in Run 1 are taken from Ref. [13].

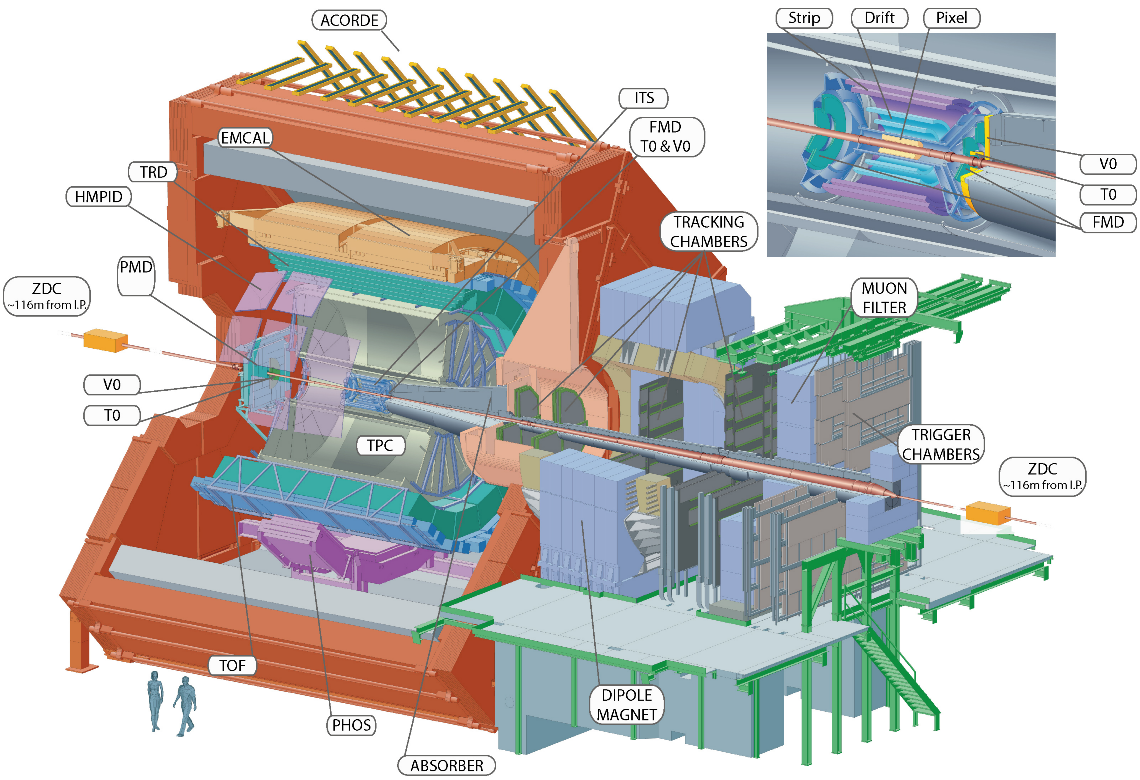

Figure 2.2: Schematic view of the ALICE detector. Taken from Ref. [13].

2.2.1 Inner Tracking System (ITS)

ITS is used to detect position of primary vertex (places, where collision occured), secondary vertices (places, where heavy hadrons decayed) and to track particles with low transverse momentum $p_T < 200$ MeV/c [3]. It is situated as close to the beam pipe as possible and it covers pseudorapidity interval $|\eta| < 0.9$ and full azimuthal angle. It consists of 6 layers of detectors, as it can be seen in Fig. 2.3. The two innermost layers are SPD (Silicon Pixel Detector), the next two are SDD (Silicon Drift Detector) and two outermost are SSD (Silicon Strip Detector).

In Table 2.2 are shown different properties of all layers of ITS in Run 1. SPD is used for reconstruction of position of primary vertex and for measurements of impact parameters of tracks coming from heavy flavour decays. SDD measures mainly energy loss of particles, that aids in further particle identification in ITS. Finally, SSD is used for matching track with signals from other detectors, mainly TPC. It also provides information about energy loss of particles.

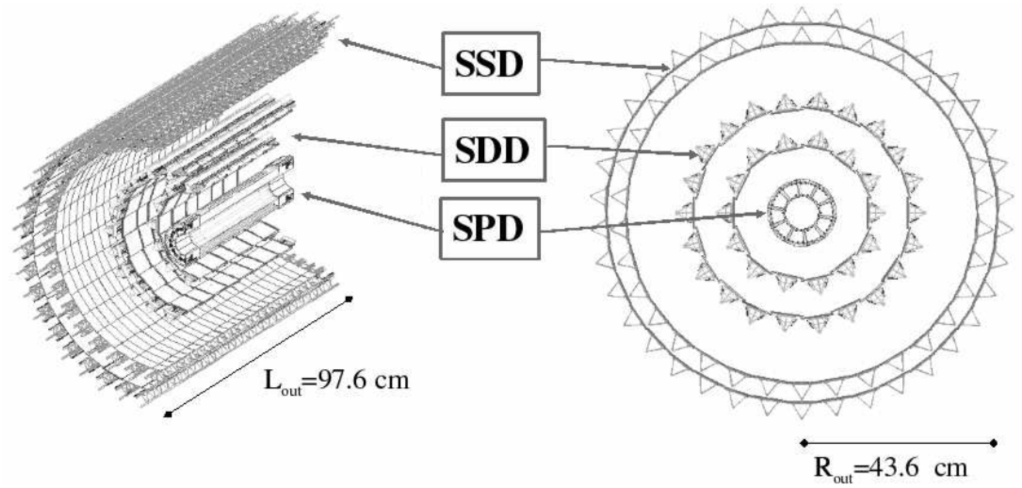

Figure 2.3: Layers of the ITS detector at the ALICE. Taken from Ref. [13].

Layer	Type	Position		Resolution	
		r [cm]	$\pm z$ [cm]	$r\phi$ [μm]	z [μm]
1	pixel	3,9	14,1	12	100
2		7,6	14,1		
3	drift	15,0	22,2	35	25
4		23,9	29,7		
5	strip	38,0	43,1	20	820
6		43,0	48,9		

Table 2.2: Properties of layers of the ALICE ITS detector: type of detection system, its distance from beam pipe r, length along beam pipe from center of ITS to both sides $\pm z$, its resolution in $r\phi$ space (perpendicular to beam pipe) and in beam direction z. Data taken from Ref. [13].

For ITS, major upgrades are planned during LS 2. The pointing resolution will be

[3]Transverse momentum p_T is value of momentum in 2D space perpendicular to the direction of colliding particles (or to the beam direction).

improved by a factor of 3. Number of silicon layers will be increased from 6 to 7, and the innermost layer will be installed closer to the interaction point. Pixel size will drop from 50×425 µm^2 to 50×50 µm^2. There are 2 different options for detector layout: 7 silicon pixel layers or a combination of 4 double sided silicon strip layers and 3 silicon pixel layers.

2.2.2 Time-Projection Chamber (TPC)

Detector situated around ITS is TPC. During Run 1, it was filled by 90 m^3 of Ne/CO_2 (90/10), in Run 2 it is filled by Ar/CO_2 (90/10). New mixture was chosen in order to have more stable response to the high particle fluxes in Run 2. In this drift gas, signals from charged particles are transported on either side of central electrode to the end plates. At each end plate, there are multi-wire proportional chambers.

TPC is the main tracking detector that offers measurements of momentum of charged particles, particle identification and helps with determination of vertex position. For fully reconstructed tracks (with signals also in ITS, TRD, TOF) it has coverage $|\eta| < 0.9$ and for reduced tracks (reconstructed with lower resolution) $|\eta| < 1.5$. It covers the full azimuth angle. Momentum range, that could be detected, is from 0.1 GeV/c to 100 GeV/c.

Resulting position resolution is from 800 μm in outer radius to 1100 μm in inner radius of TPC. In beam direction it is from 1100 μm to 1250 μm. Energy loss resolution for isolated tracks is around 5%, depending on multiplicity of tracks in collision. Energy loss in detector and associated momentum of passing particle can be used for particle identification. Performance of particle identification in TPC is shown in plot in Fig. 2.4.

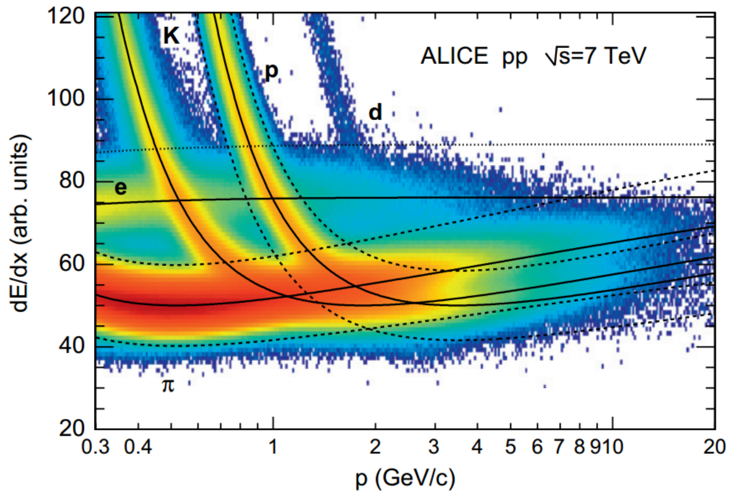

Figure 2.4: Energy loss $\mathrm{d}E/\mathrm{d}x$ spectrum versus momentum in the ALICE TPC from pp collisions at $\sqrt{s} = 7$ TeV in Run 1. Taken from Ref. [22].

Achievable track impact parameter resolution for tracks reconstructed by the ALICE ITS and TPC detectors could be observed in Fig. 2.5. For this study, main track cuts are on pseudorapidity in the TPS $|\eta| < 0.9$ and at least 70 (out of 159) points in the TPC and 6 hits in ITS. Achieved resolution is better for track with higher p_{T}, and for tracks with $p_{\mathrm{T}} > 1$ GeV/c it is better than 70 µm. Reconstruction performance is nearly the same for all collision system at Run 1 energies, weak improvement from pp to p-Pb and Pb-Pb (with charged multiplicity) is observed.

Charged track in jets are then used for reconstruction of places of heavy hadron decays, secondary vertices. Position resolution of secondary vertices in jets of different

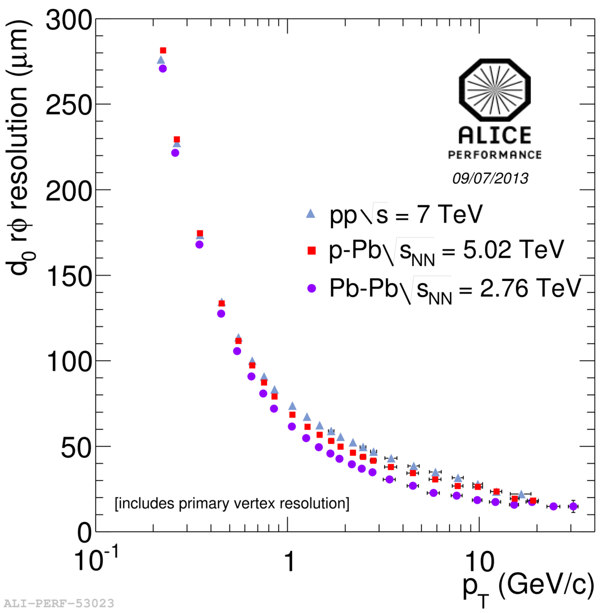

Figure 2.5: Track impact parameter d_0 resolution in the transverse plane $r\phi$ vs p_T for charged particles in pp (triangles), Pb-Pb (squares) and p-Pb (circles) data at the ALICE. The resolution includes the contribution from the primary vertex resolution, which improves from pp to p-Pb and Pb-Pb (with charged multiplicity). Taken from Ref. [23].

flavours, achievable by tracks detected by the ALICE, is shown in Fig. 2.6. Secondary vertices are reconstructed using 3 tracks with transverse momentum $p_\mathrm{T} > 1$ GeV/c. Resolution in both x and y coordinates are nearly the same for secondary vertices in jets of all flavours and it is generally $< |0.02|$ cm.

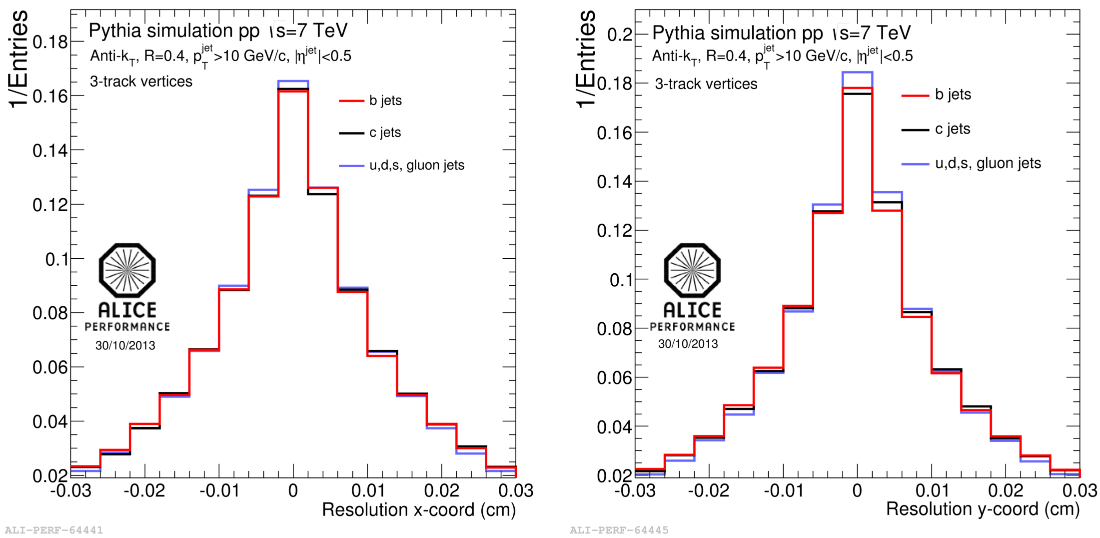

Figure 2.6: Resolution in x coordinate (left) and y coordinate (right) of the secondary vertex reconstructed using three charged tracks with $p_\mathrm{T} > 1$ GeV/c in jets of different flavours (beauty, charm, light), for simulated pp collisions at $\sqrt{s} = 7$ TeV at ALICE. Taken from Ref. [24]

2.2.3 Calorimetry at ALICE

The biggest calorimeter at ALICE is ElectroMagnetic Calorimeter (EMCal). Its main purpose is to study jets and to trigger high-energy events. Thanks to its capability of detecting neutral energy of jets, full jets could be reconstructed at ALICE. It is situated right under ALICE magnet, so around 4.5 m from the interaction point. It covers $|\eta| < 0.7$ and azimuthal angle interval with size $\Delta\phi = 107°$. In azimuth, it is situated opposite to PHOS (PHoton Spectrometer). Position of EMCal in central barrel is shown in Fig. 2.7.

EMCal is Pb-scintillator, that is segmented into 12 288 towers of $6.0 \times 6.0 \times 24.6$ cm^3, all directed to the interaction point. Each tower contains alternating layers of Pb (thickness 1.44 mm) and polystyrene base scintillators (BASF143E + 1.5%pTP + 0.04%POPOP, thickness 1.76 mm). Moreover, each tower is optically isolated.

Resulting energy resolution of the EMCal is $15\%/\sqrt{E} \oplus 2\%$ [25] for jet measurements and $12\%/\sqrt{E} \oplus 1,7\%$ [25] for measurements of electrons and photons. Position of electromagnetic showers is measured with precision of 1.5 mm + 5.3 mm/$\sqrt{E_{deposit}}$ [25], that is nearly the same in all directions.

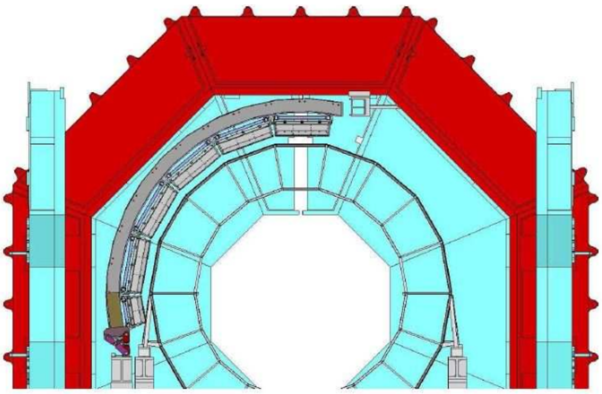

Figure 2.7: Position of the EMCal (grey) in central barrel of the ALICE detector. Taken from Ref. [13].

PHOS is also an electromagnetic calorimeter, that aims to study thermal and dynamic properties of the initial phase of collisions. It is constructed to measure high-p_{T} π^0 and low-p_{T} photons. As scintillator, $PbWO_4$ of 20 X_0 thickness is used. In front of PHOS, there is a set of multiwire chambers, that serve as charged particle veto (CPV). During Run 1, there were 3 modules of PHOS and before Run 2, another 1 module was installed (Fig. 2.8.

During LS1, the Di-Jet Calorimeter (DCal) was installed at ALICE. It is placed back-to-back to EMCal and enlarges azimuthal coverage of calorimeters up to 174° with the same coverage in η as EMCal. It is placed next to PHOS, as can be seen in Fig. 2.8. All of the 6 DCal supermodules are built exactly same as they are in EMCal. All of the calorimetry upgrades during LS 1 are expected to raise performance of the ALICE detector mainly in jet correlations studies.

In summary, the ALICE detector offers a great opportunity to study QCD matter. Its physical program is being broadened by upgrades during LS 1 and future ones. These will expand its capability to detect particles, for example the track impact parameter will be improved by factor 3 (6) in the transverse (longitudinal) direction. By expanding calorimeters, acceptance and precision of neutral energy particles measurement will be multiplied. These upgrades would enable very detailed study of particle and jet production

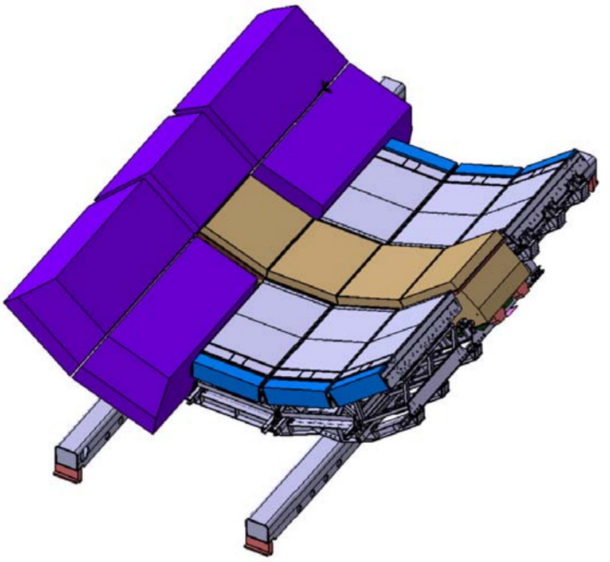

Figure 2.8: Position of 6 supermodules of the DCal (light blue) next to 4 modules of the PHOS (yellow). Also hypothetical 5 modules of future Very High Momentum Particle Detector (VHMPID) are shown. Taken from Ref. [26].

in heavy-ion collisions.

Chapter 3

Quark-gluon plasma

By colliding nuclei of heavy ions at accelerator experiments, matter at large temperature and energy density could be created. If these are large enough, the confinement of quarks disappears and quark-gluon plasma (QGP) could be observed. QGP is the new state of hot and dense nuclear matter.

The first prediction of critical temperature, when hadrons are melted and phase transition occurs, was made by Hagedron in 1960s [27]. He built the new statistical model, involving thermodynamics of strong interactions at large temperatures. In 1970s and 1980s experiments studying hot nuclear matter were built and first observables of the QGP were measured.

At the beginning, the idea was that heavy-ion collisions are just superposition of proton collisions. In 1992, no enhancement of strangeness was measured in p-A collisions [28] by the NA35 Collaboration in CERN and in 1994, strangeness enhancement in central sulfur-sulfur collision was measured [29]. This was the first hint, suggesting that enhancement in A-A collisions is caused by the hot medium. Then, many studies of pion production in central heavy-ion collisions in both Super Proton Synchrotron (SPS) in CERN and Alternating Gradient Synchrotron (AGS) in Brookhaven National Laboratory (BNL) were completed. In 1997, quantitative agreement of the results on pion and strangeness production with calculations concerning presence of the QGP in heavy ion collisions was found. Other observables have also shown possible medium creation, such as charmonium suppression or dilepton studies. Based on these results, in 2000, the announcement on the QGP discovery was made by CERN [30], but it was not published and many physicist were skeptical about it. In any case, SPS showed several observations compatible with the QGP. More detailed studies in different kinematic range were needed.

In 2000, Relativistic Heavy Ion Collider (RHIC) was built to study hot and dense nuclear matter and proton spin structure. Several new phenomena were discovered to give an evidence of the QGP in heavy-ion collisions [31]: bulk collective elliptic flow, modification of jet spectra (jet quenching) and their azimuthal distribution. Since then, there have been no doubts on existence of the QGP. There are still open questions related to heavy-flavour production, jets and QCD phase diagram remaining.

In the evolution of the heavy-ion collisions, different phases could be distinguished. Schematic picture of this evolution is shown in Fig. 3.1. In the first phase, there are many inelastic collisions between nuclei. After this phase, system becomes nearly stable, and in this state quark-gluon plasma could exist. Because of expansion of the system, temperature is decreasing. When it drops to critical temperature T_C, confined nuclear matter starts to be formed in process called hadronisation. For baryochemical potential (energy needed to add one baryon to system) $\mu_B = 0$ MeV, this temperature is expected to be around 170 MeV. When temperature drops below temperature of hadrochemical freeze-out T_{ch}, hadron gas is present. In this medium, inelastic collisions still occur. System continues expanding and below some T_{fo}, there are no inelastic collisions betweeen hadrons. This is point of thermal freeze-out, and for $\mu_B = 0$ MeV it occurs at temperature close to critical temperature. For higher μ_B, it occurs at a temperature of around 10-20 MeV smaller than the critical temperature.

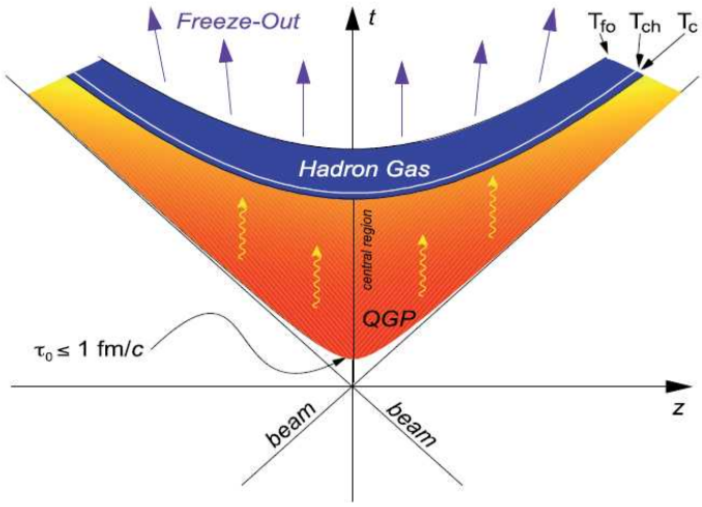

Figure 3.1: Description of heavy-ion collisions in one space (z) and one time (t) dimension (in a light cone). Shown evolution of these collisions: critical temperature of phase transition T_C, temperature of hadrochemical freeze-out T_{ch} and temperature of thermal freeze-out T_{fo}. Taken from Ref. [32].

Nuclear matter has its phase diagram, that can be seen in the left panel of Fig. 3.2. It shows state of matter for different temperatures and baryochemical potential. As we can see, confined nuclear matter (hadrons) exists at temperatures below ≈ 170 MeV for $\mu_B = 0$ MeV. For baryochemical potential bigger then 1200 MeV and temperatures down to approximately 100 MeV, there exists state called color superconductor.

There are two different phase transitions from quark-gluon plasma to hadrons. For low $\mu_B < 350$ MeV (dashed line in Fig. 3.2 left) it is cross over transition, for higher μ_B, there is first order transition. Between cross over transition and first order transition, for 200 MeV$< \mu_B < 500$ MeV, there is critical point. Search of this point is one of the goals for heavy-ions physics, since its precise position in phase diagram is still unknown. In Fig. 3.2 left, regions studied by experiments are also shown.

One of the most important experimental programs, that study QCD phase diagram, is the Beam Energy Scan (BES) at the STAR experiment [33]. Its main goal is to study properties and the position of critical point in the QCD phase diagram. Collecting data in Au-Au collisions with different energies ($\sqrt{s_{\mathrm{NN}}} = 7.7, 11.5, 19.6, 27, 39$ GeV) allows to cover μ_B from 100 to 400 MeV. Figure 3.2 right shows measured parameters of chemical freeze-out, extracted from different collision centralities and energies. The conditions of chemical freeze-out were calculated from measured particle ratios using the statistical thermal model Thermus [34]. Also other theoretical predictions are consistent with measured parameters. Measured temperature of chemical freeze-out for low μ_B is approximately 165 MeV.

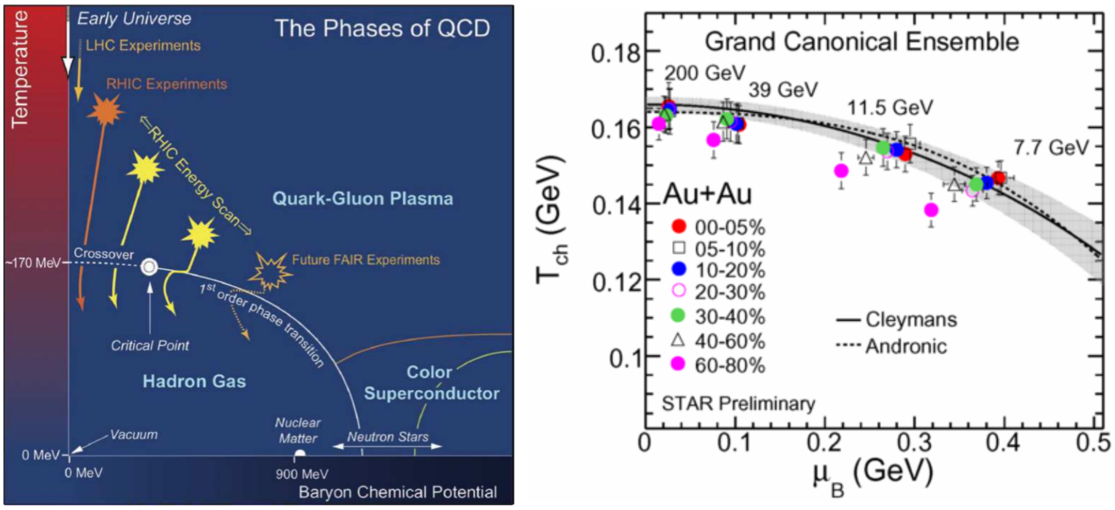

Figure 3.2: Phase diagrams of nuclear matter, in space of baryochemical potential μ_B and temperature T. Left: Description of nuclear matter phases and transition, as well as regions tested by experiments are displayed. Taken from Ref. [32]. Right: Results of measurement at the STAR experiment for different beam energies and centralities, compared to theoretical prediction. The curves represent the theoretical calculations. Taken from Ref. [33]

3.1 Experimental observations of the QGP

Quark-gluon plasma is being studied at experiments in the CERN and the BNL. There are many different analysis, that show existence of hot and dense nuclear matter by studying different effects of medium on the observables. In this section, several observations based on LHC measurements will be mentioned. One of the most important observables is particle production suppression induced by medium. It is observed via nuclear modification factor R_{AA}, usually defined as

$$R_{AA} = \frac{1}{N_{coll}} \frac{Y(AA)}{Y(pp)}, \tag{3.1}$$

where $Y(AA)$ and $Y(pp)$ are particle yields in heavy ions and pp collisions (usually in some specific momentum or pseudorapidity intervals) and N_{coll} is average number of binary collisions of nucleons in heavy-ion collision, that depends on centrality of collision. If $R_{AA} < 1$, production is suppressed, in case $R_{AA} > 1$, production is enhanced.

R_{AA} of inclusive charge hadrons production in the most central (0-5%) Pb-Pb collisions at $\sqrt{s_{\mathrm{NN}}} = 2.76$ TeV is shown in Fig. 3.3. The results from three LHC experiments (ALICE, ATLAS, CMS) are presented. As it can be observed, these agree and show suppression of hadrons. This suppression is evident but non-constant, there is some structure. For $p_{\mathrm{T}} > 30$ GeV$/c$, the three experiments start to differentiate. This needs further studies to establish final shape of R_{AA}.

Jets are collimated sprays of hadrons, Chapter 5 describes them in more detail. If the pair of jets (di-jet) is created in collision, where no hot medium is expected, both of the jets could be observed. They would have nearly the same energy, but the opposite direction. In the case of heavy-ion collision, if di-jet is created in periphery of the hot and dense medium, one of the jets is expected to be more suppressed (have less energy) than the other one. This di-jet symmetry was measured at the ATLAS experiment [37]. In this analysis, jets are labeled as opposite, if their azimuthal angle separation is bigger than

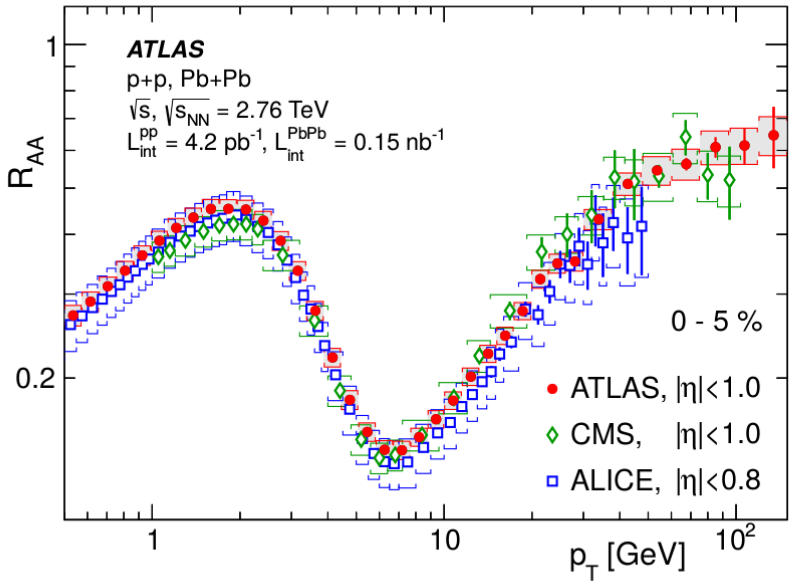

Figure 3.3: The nuclear modification factor R_{AA} dependence on transverse momentum p_{T} measured in centrality interval 0-5% at ATLAS, ALICE and CMS experiments. Statistical uncertainties are shown with vertical bars and systematic uncertainties with brackets. Taken from Ref. [36].

$\pi/2$. The imbalance between opposite jets could be expressed by asymmetry factor A_J,

$$A_J = \frac{E_{\mathrm{T1}} - E_{\mathrm{T2}}}{E_{\mathrm{T1}} + E_{\mathrm{T2}}}, \tag{3.2}$$

where the first jet should have energy $E_{\mathrm{T1}} > 100$ GeV, the second (opposite) one should have energy $E_{\mathrm{T1}} > 25$ GeV.

Results of the jet asymmetry study in pp collision at $\sqrt{s} = 7$ TeV and Pb-Pb collisions at $\sqrt{s_{\mathrm{NN}}} = 2.76$ TeV are shown and compared in Fig. 3.4. The results from Hijing Pythia simulations are shown to illustrate the effect of the heavy ion background on jet reconstruction. In upper plots in Fig. 3.4, the distribution of A_J for 4 centrality bins is displayed. In pp collisions, A_J is distributed exponentially. As it can be observed in Pb-Pb collisions, A_J depends on centrality, it is shifted to higher values and for the most central collisions, peak near $A_J = 0$ disappears and the new for $A_J \approx 0.4$ starts to form. This means that the more central the collision is, the more evident the dijet asymmetry is, thus the hot and dense medium - QGP could be present in such collisions.

Bottom line of plots in Fig. 3.4 displays distribution of the difference of the azimuthal angle between two jets $\Delta\phi$. It shows, that the leading and the second jet are created back-to-back. However, for more central collisions, some increase for low $\Delta\phi$ is measured, but it can be caused by high number of jets in Pb-Pb collisions.

Another observable, that serves as a test of the medium created in heavy-ion collisions, is the momentum anisotropy of the final state particles (anisotropic flow). It is caused by initial spatial anisotropy in overlap region of colliding hadrons. It was observed, that particles in this region have collective behavior. Components of the anisotropic flow are usually described by Fourier expansion of the third derivation of the particles distribution,

$$E\frac{\mathrm{d}^3N}{\mathrm{d}^3p} = \frac{1}{2\pi}\frac{\mathrm{d}^2N}{p_T\mathrm{d}p_T\mathrm{d}y}\left(1 + 2\sum_{n=1}^{\infty} v_n \cos\left[n(\Phi - \psi_n)\right]\right), \tag{3.3}$$

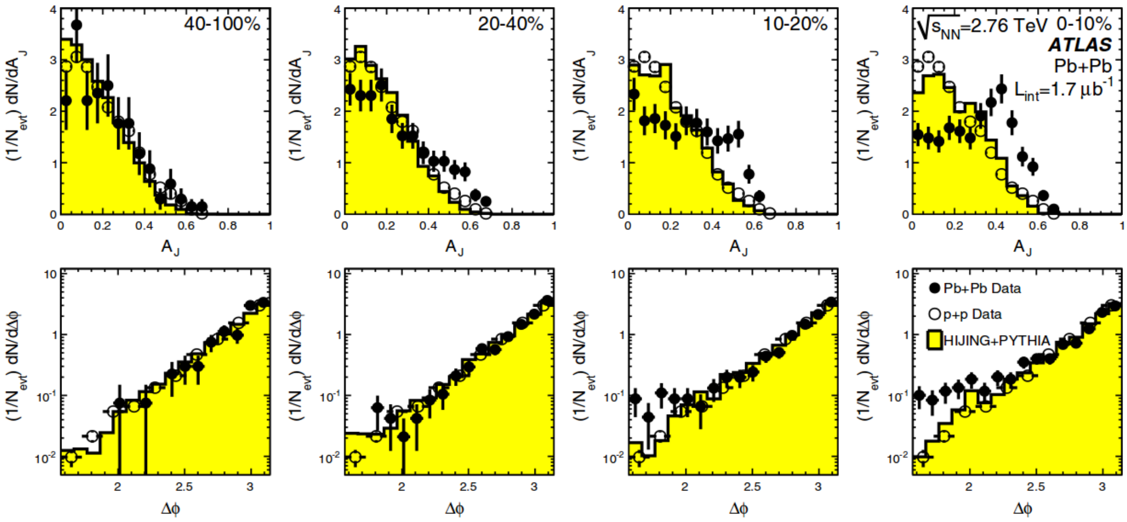

Figure 3.4: Top: Jet asymmetry distributions for data (points) and unquenched Hijing with superimposed Pythia dijets (solid yellow histograms), as a function of collision centrality (left to right from peripheral to central events). Proton-proton data from $\sqrt{s} = 7$ TeV at the ATLAS, analyzed with the same jet selection, are shown as open circles. Bottom: Distribution of $\Delta\phi$, the azimuthal angle between the two jets, for data and Hijing Pythia, also as a function of centrality. Taken from Ref. [37].

where E is energy, p is momentum, p_{T} is transverse momentum, Φ is azimuthal angle, y rapidity of produced particle and ψ_n is angle of the spatial plane of harmonics n. ψ_n is defined relatively to reaction plane, that is defined by beam axis and impact parameter of colliding nuclei. The anisotropy is usually characterized by coefficients

$$v_n(p_T, y) = \langle \cos\left[n(\Phi - \psi_n)\right] \rangle. \tag{3.4}$$

These coefficients could be measured in heavy-ion collisions. Since shape of the overlapping region of colliding nuclei depends on centrality of the collision (Fig. 3.5), coefficients of anisotropic flow are also expected to depend on it.

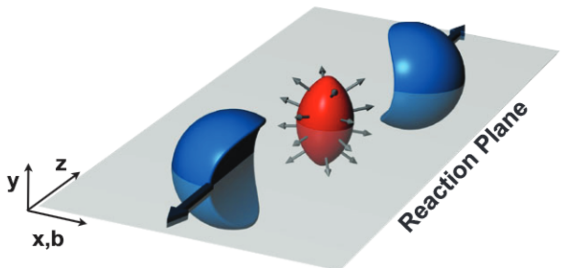

Figure 3.5: Shape of overlapping (interaction) volume of colliding nuclei in non-central heavy-ion collision. Taken from Ref. [38].

Elliptic flow of particles is described by the v_2 coefficient. It describes ellipticity of the overlapping region of nuclei and further elliptic expansion of interacting volume, as it is sketched in Fig. 3.5. Dependence of v_2 on centrality and p_{T} for different particles is measured at the ALICE experiment in Pb-Pb collisions at $\sqrt{s_{\mathrm{NN}}} = 2.76$ TeV ant it is shown in Fig. 3.6. As it can be observed for all particles, v_2 is bigger for peripheral than for central collisions. These observations are consistent with the expected initial state eccentricity, that is more significant for peripheral collisions. Measurements are consistent with theoretical predictions of hydrodynamical model.

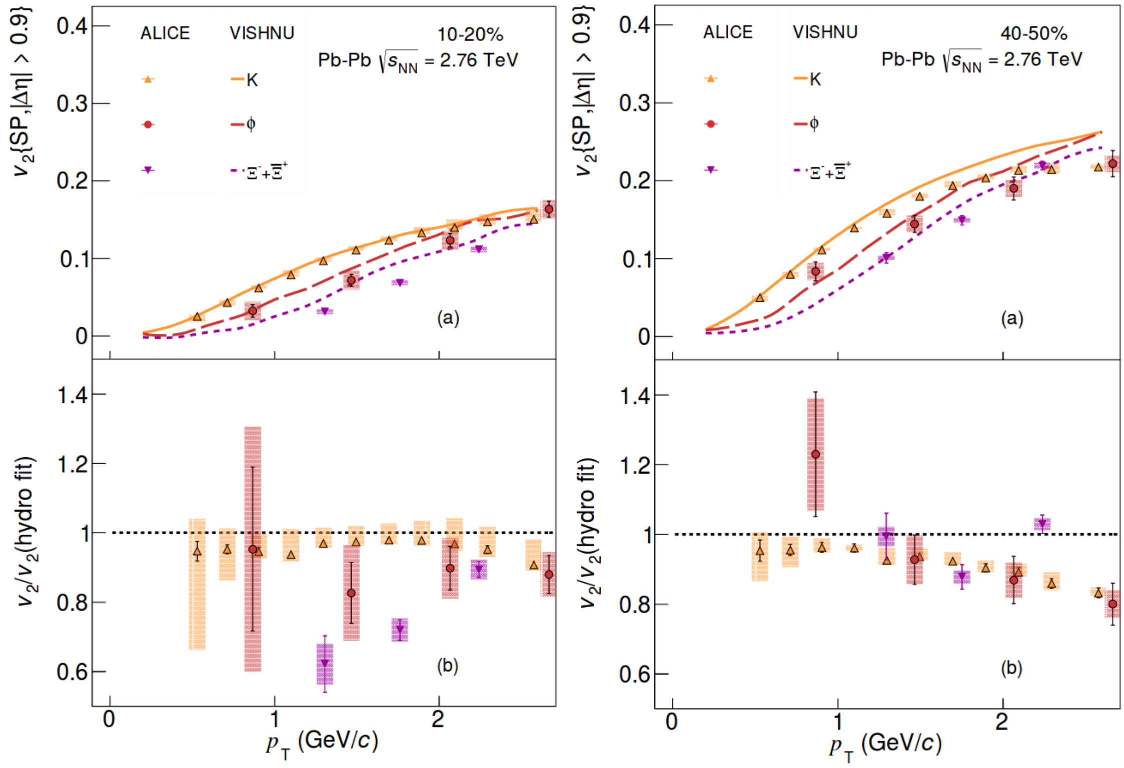

Figure 3.6: Measured eliptic flow v_2 vs. transverse momentum p_T for semi-central and peripheral Pb–Pb collisions at $\sqrt{s_{NN}} = 2.76$ TeV for different particles compared to theoretical, hydrodynamic calculations coupled to a hadronic cascade model. The error bars correspond to statistical uncertainties, while the hollow boxes around each point indicate the systematic uncertainties. Taken from Ref. [39].

Another striking evidence of the QGP presence in collisions is the suppression of quarkonia states[1]. The confinement inside quarkonia is expected to be screened by the free color charges (quarks and gluons) in the hot medium - this phenomenon is color Debye screening [40]. If the screening is strong enough, quarkonia are melted and their production is suppressed. The Debye screening depends on the medium temperature and on the binding energy of quarkonia. If the binding energy, as well as suppression of quarkonia are know, the temperature reached in the medium could be estimated.

J/ψ is one of the lightest quarkonium, its suppression for different centralities measured by heavy-ion experiments is displayed in Fig. 3.7. ALICE, STAR, PHENIX and CMS experiments consistently show, that J/ψ R_{AA} is smaller with higher centrality of the collision. The more central the collision is, the higher is the expected temperature of the medium and thus the suppression is more evident. However, roles of charmonium regeneration and Cold Nuclear Matter effects are not well understood and influence measurements of J/ψ suppression. These processes are important in order to set quantitative description of the QGP properties. Charmonium regeneration during hadronisation phase is important for large transverse momentum of charmonium and for large centralities of collisions.

At the CMS experiment, different quarkonia suppression is measured. Plot summarizing these measurements is in Fig. 3.8. Dependency of R_{AA} on the binding energy of

[1]Quarkonium is meson with valence quark and antiquark having the same flavour.

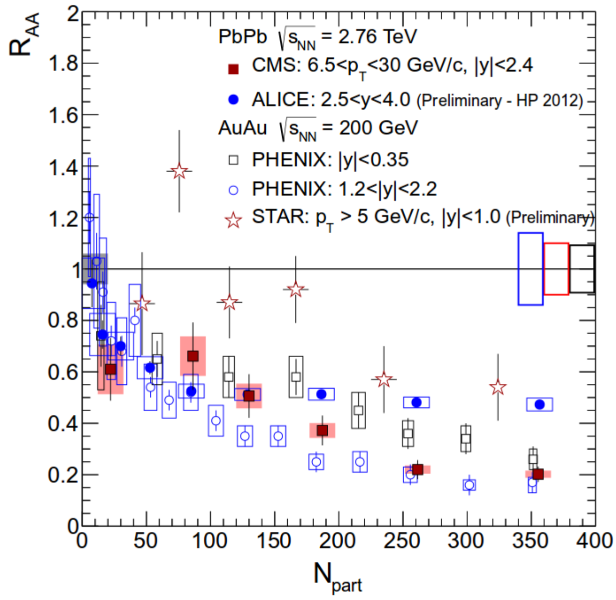

Figure 3.7: J/ψ nuclear modification factor R_{AA} as a function of centrality. The prompt J/ψ measurement of CMS is compared to inclusive J/ψ measurements by ALICE, STAR, and PHENIX at midrapidity and forward rapidity. Statistical (systematic) uncertainties are shown as bars (boxes). In the case of the STAR results, statistical and systematic uncertainties are shown combined as bars. Global uncertainties from the pp luminosity are shown as boxes at unity. Taken from Ref. [41].

quarkonia is consistent with theoretical predictions - the least tightly bound states melt the most.

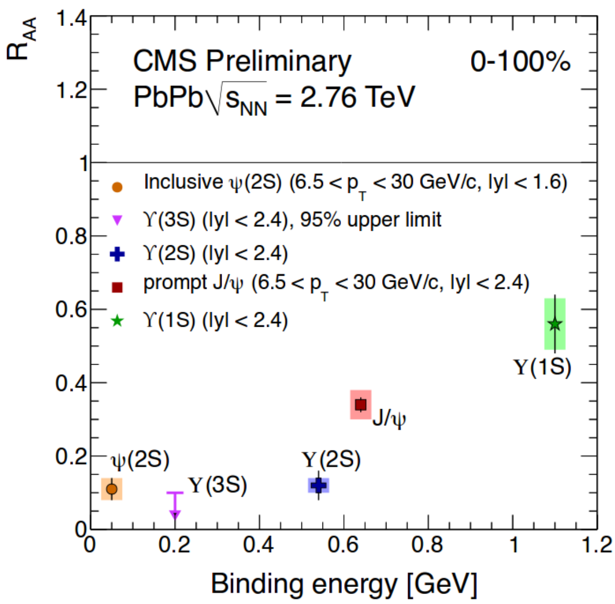

Figure 3.8: Nuclear modification factor R_{AA} for the quarkonia measured by CMS in heavy ion collisions shown as a function of the binding energy of the state. Taken from Ref. [42].

Although the new hot and dense state of nuclear matter, the quark-gluon plasma, was discovered, its properties need further studies. Anisotropic flow of particles in heavy-ion collision , as well as suppression of particle production in the quark-gluon plasma are proven. Mass ordering of the energetic loss of heavy partons in the medium is not as evident as predicted by the theory, thus it needs to be further investigated.

Chapter 4

Experimental results from heavy-flavour studies

Heavy quarks (c and b) are important probe of not only the hot medium (QGP) created in heavy-ion collisions, but also various aspects of QCD in hadronic collisions. The large mass of quarks is a long distance cut-off in studies of hard-scattering QCD processes. Hadronic collisions serve as a reference in studies of medium effect on quark production. Thanks to their large mass, b and c quarks are expected to be created in collision, not as an effect of medium. Thus they are present during the whole evolution of the system and they are important probes of the medium properties. Not only the medium temperature could be tested via melting of quarkonium states (described in Section 3.1), but also its density is tested. This density of partons in the medium influences the energy loss of heavy quark in the medium.

There are two main sources of energy loss of quark in the medium. One of them is collisional energy loss, that is important for low transverse momentum of traversing parton. The other one is inelastic energy loss via gluon radiation. This is expected to depend on the quark colour and mass [43]. The mass ordering is expected in this energy loss, so for gluons and light quarks it is higher than for charm quarks, and for them it is higher than for b quarks.

Measurements in proton-nucleus collisions are important to differentiate between effects of the QGP and multi-particle environment in nucleus-nucleus collisions. In proton-nucleus collisions, cold nuclear matter (CNM) could be created. CNM effects, investigated in such collisions, are for example partonic density in the colliding nuclei, scattering of partons in the nucleus, interactions of produced particle with partons in the nuclei (or in hadrons not scattered in the collision). Studying production of heavy-flavour production in nucleus-nucleus collisions needs clear understanding of reference proton-proton and proton-nucleus collisions.

Branching ratio of (semi-)leptonic decays of beauty hadrons is relatively large, at the level of 20% ([1]). Therefore natural way to study beauty is via lepton spectra. These have large contribution from heavy flavour decays for large momentum. Nuclear modification factor for heavy flavour electrons in different collisional system is shown in Fig. 4.1 (Left). In the case of Au-Au and Cu-Cu collisions, suppression rises with the transverse momentum. In high transverse momentum regions $p_{\mathrm{T}} > 4$ GeV/c, for Au-Au collisions, the suppression is the biggest and for d-Au collisions, R_{AA} is consistent with unity. For smaller transverse momentum, enhancement due to Cronin effect [44] is observed. These results support the idea of presence of the hot medium in Au-Au collisions and no medium in d-Au collisions.

Heavy-flavour electrons suppression dependency on centrality of Au-Au collision is presented in Fig. 4.1 (Right). The dependence on centrality is evident for high-p_T electrons, and its shape is consistent with the π^0 suppression. Heavy-flavour electrons with high-p_T are less suppressed than pions only for larger number of participants in collision. The production of heavy-flavour electrons with $p_T < 0.3$ GeV/c, measuring the production of charm down to $p_T = 0$ GeV/c, is unity for all collision centralities.

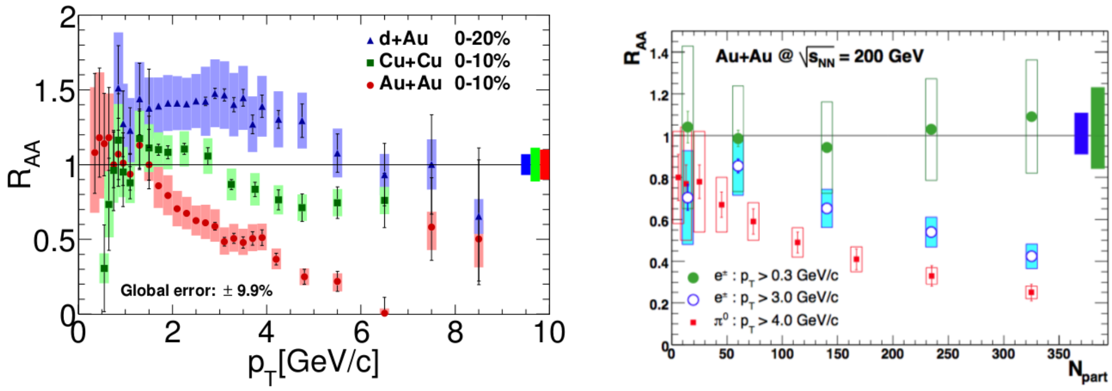

Figure 4.1: Left: The transverse momentum dependence of the nuclear modification factors of heavy-flavour decay electrons at mid-rapidity in central d–Au, Cu–Cu and Au–Au collisions at $\sqrt{s_{NN}} = 200$ GeV at STAR. Right: R_{AA} of heavy-flavour decay electrons at mid-rapidity with p_T above 0.3 and 3 GeV/c and of π^0 with $p_T > 4$ GeV/c as function of number of participants N_{part}. Taken from Ref. [45].

At the LHC, ALICE experiment measures leptons from heavy-flavour decays in Pb-Pb collisions at $\sqrt{s_{NN}} = 2.76$ TeV. Figure 4.2 shows nuclear modification factor of muons from such decay in forward rapidity in central collisions. For transverse momentum of muons larger than 4 GeV/c, R_{AA} is at the level of 0.4, thus the suppression of heavy flavour is evident, see Fig. 4.2 (Left). The shape of centrality dependence of such suppression for muons with $6 < p_T < 10$ GeV/c is shown in Fig. 4.2 (Right), and it is comparable with the shape of electrons with $p_T > 3$ GeV/c shown in Fig. 4.1 (Right). For the most central collisions, nuclear modification factor for muons is at the level of 0.3.

The well measured heavy-flavour probe of the medium are D mesons. In data, D mesons are reconstructed via decays to kaons and pions. Both ALICE and STAR experiments measured their nuclear modification factor, shown in Fig. 4.3. The left panel of Fig. 4.3 shows the results for D^0 in the most central Au-Au collisions at $\sqrt{s_{NN}} = 200$ GeV, measured by STAR. Suppression is evident for $p_T > 2$ GeV/c, on the other hand, for low p_T the ridge is observed. At $p_T \approx 1.5$ GeV/c, the enhancement of production is observed. Figure 4.3 (Right) shows average suppression of D meson for p-Pb and two centrality classes of Pb-Pb collisions, measured by ALICE. The p_T range of measurements is larger than for STAR experiment, it is $2 < p_T < 16$ GeV/c. For the most central collisions, observed suppression is at the same level as at the STAR, where for $p_T > 2$ GeV/c the nuclear modification factor is smaller than 0.5. For the more peripheral Pb-Pb collisions, suppression is still observed at the level of ≈ 0.6. In case of p-Pb collisions, no evident enhancement or suppression of D meson production is measured, however, nuclear modification factor is not constant in p_T and specific shape could be observed. Although D mesons are currently well measured and we would like to have such measurements of heavier B mesons, the shape of nuclear modification factor needs to be investigated in more

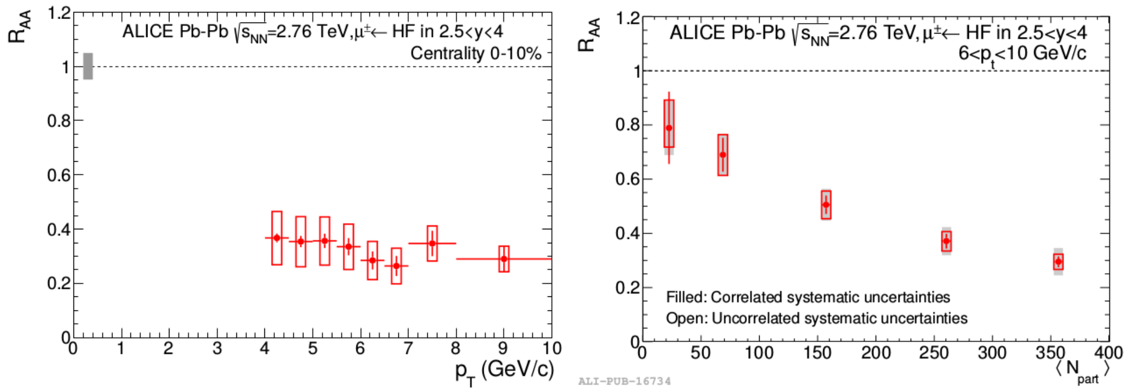

Figure 4.2: Nuclear modification factor R_{AA} of heavy-flavour decay muons with $2.5 < y < 4$ measured by ALICE in Pb–Pb collisions at $\sqrt{s_{\mathrm{NN}}} = 2.76$ TeV as a function of p_{T} in the 10% most central collisions (Left) and as a function of the mean number of participating nucleons $\langle N_{\mathrm{part}} \rangle$ (Right). Taken from Ref. [46].

details. Also, uncertainties are needed to be smaller, so that the comparison with the energy loss of lighter particles is possible.

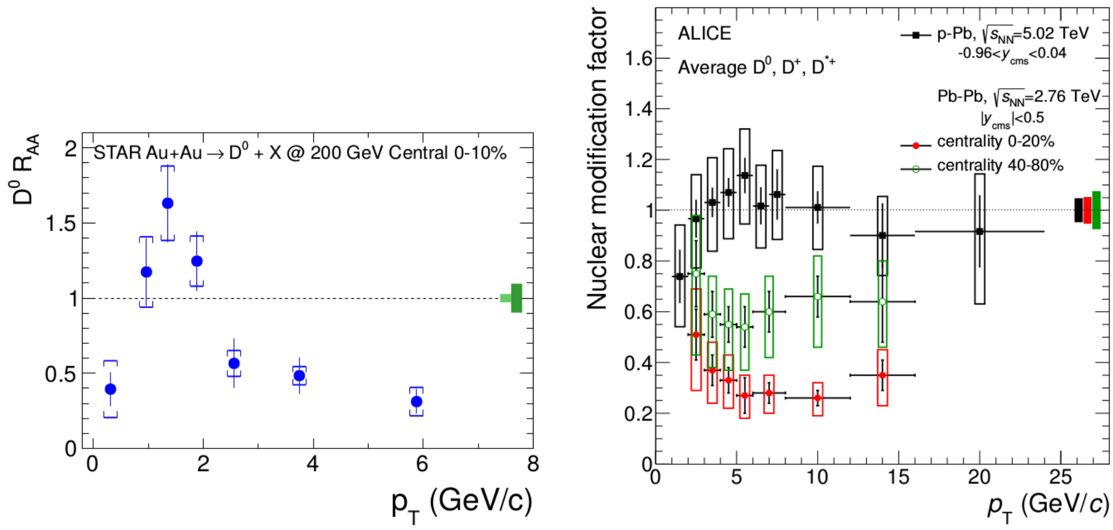

Figure 4.3: Left: Transverse momentum (p_{T}) dependence of the nuclear modification factor R_{AA} of D^0 mesons in the 10% most central Au–Au collisions at $\sqrt{s_{\mathrm{NN}}} = 200$ GeV at STAR. Right: R_{AA} of prompt D mesons (averaged) versus p_{T} for the 0–20% (red discs) and 40–80% (green circles) centrality classes measured by ALICE in Pb–Pb collisions at $\sqrt{s_{\mathrm{NN}}} = 2.76$ TeV and minimum-bias p–Pb collisions at $\sqrt{s_{\mathrm{NN}}} = 5.02$ TeV (black squares). Taken from Ref. [45].

Beauty hadron usually decays to hadrons containing charm quark, e.g. $B \to J/\psi + X$. Charm hadrons are also not detected in the detector, thus beauty is hard to reconstruct. Cross section of beauty production via non-prompt J/ψ (coming from beauty decays) in p-Pb collisions at $\sqrt{s_{\mathrm{NN}}} = 5.02$ TeV was firstly measured at the LHCb experiment. Because of geometry of the detector, J/ψ is measured in forward rapidities and for low p_{T}. Nuclear modification factor resulting from this analysis is shown in Fig. 4.4. Non-prompt component of measured J/ψ is extracted by template fitting. As a reference, extrapolated data from pp collisions at $\sqrt{s} = 2.76, 7, 8$ TeV are used. Figure 4.4 (Left) shows the dependency of the nuclear modification factor on the rapidity of J/ψ. No large suppression for $p_{\mathrm{T}} < 14$ GeV/c is observed in backward rapidity, a small one is observed in the forward region, which is consistent with theoretical predictions. The dependency of the ratio of backward and forward suppression vs the transverse momentum of particle is displayed in Fig. 4.4 (Right). The mean value of this ratio is slightly smaller than unity, indicating weak rapidity asymmetry.

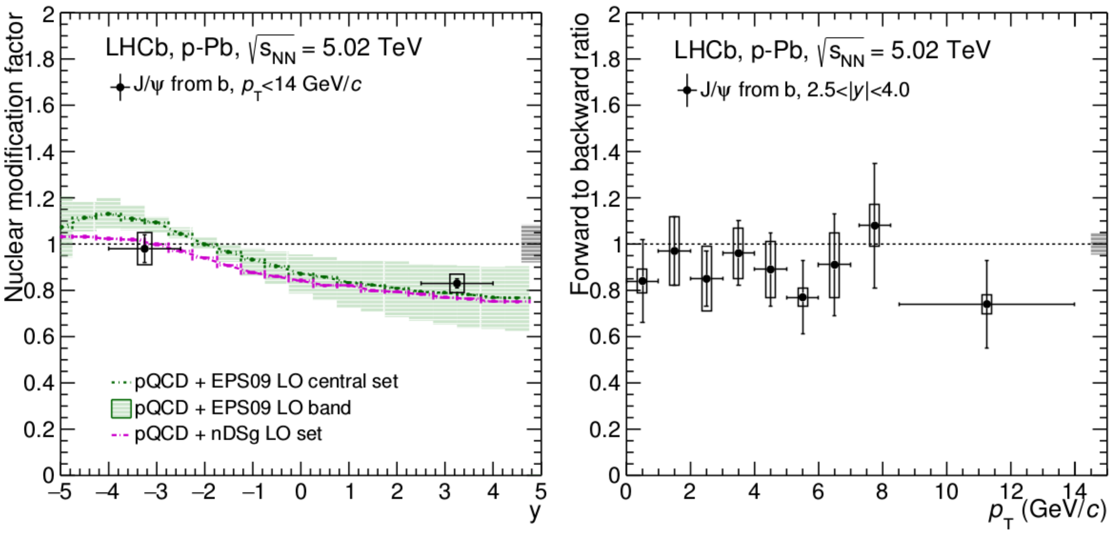

Figure 4.4: LHCb measurements of non-prompt J/ψ mesons in p–Pb collisions at $\sqrt{s_{\mathrm{NN}}} = 5.02$ TeV. Left: Nuclear modification factor as a function of rapidity, compared to nPDF-based calculations. Right: Forward to backward rapidity ratio as a function of transverse momentum. Taken from Ref. [45].

The production of non-prompt J/ψ in mid-rapidity region is studied by the ALICE and the CMS experiments. The overall measured suppression dependency on Pb-Pb collision centrality is displayed in Fig. 4.5. Results from the two experiments are consistent, and show nuclear modifiation factor $R_{\mathrm{AA}} \approx 0.35$ for high-p_{T} J/ψ. In case of J/ψ with lower p_{T}, the suppression is smaller, at the level of 0.7. We should be conscious about the large uncertainty in the ALICE results.

As the main goal of heavy-flavour studies is the measurement of energy loss dependency on parton mass, the comparison of R_{AA} for different flavour hadrons is natural. Figure 4.6 shows the comparison of charm mesons (D and non-prompt J/ψ) with the inclusive charged hadrons, both in central Pb-Pb collisions. Although R_{AA} of D mesons and charged hadrons are compatible within uncertainties, mean value for charged hadrons is smaller than for D mesons. The same case is for non-prompt J/ψ, expected to come from beauty decays, and D mesons. On the other hand, the difference between non-prompt J/ψ suppression and the one for charged hadrons is evident. Although the mean values of R_{AA} for different particle species show some mass ordering, the uncertainties of measurements are too large. Also, the differences in R_{AA} are not as large as expected in theory. No conclusions have been made as further measurements are needed. In addition, non-prompt J/ψ do not give the right access to kinematics of mother B meson, since the p_{T} of J/ψ could be shifted by 2-3 GeV/c with respect to B meson. Also, the kinematical properties (transverse momentum and energy) of mesons does not correspond to properties of the quarks.

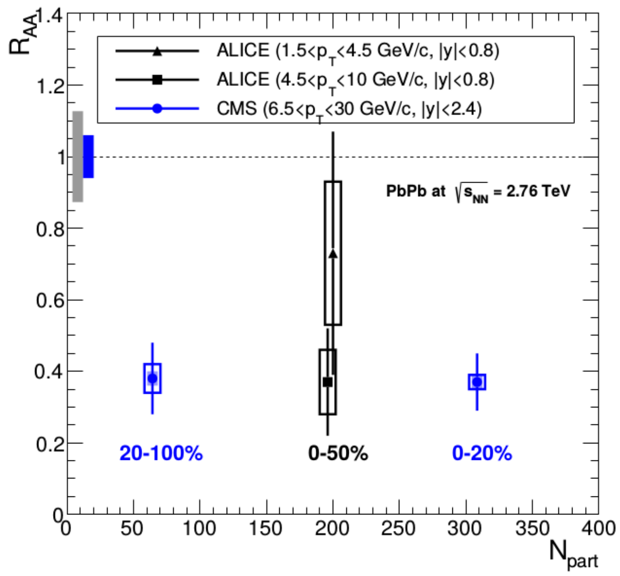

Figure 4.5: Non-prompt J/ψ nuclear modification factor R_{AA} in Pb-Pb collisions at $\sqrt{s_{\mathrm{NN}}} = 2.76$ TeV, measured in two centrality bins from CMS and in one centrality bin for two p_{T} ranges from ALICE. The ALICE points are slightly shifted horizontally for better visibility. The correlated uncertainties are shown as filled box at $R_{\mathrm{AA}} = 1$. Taken from Ref. [45].

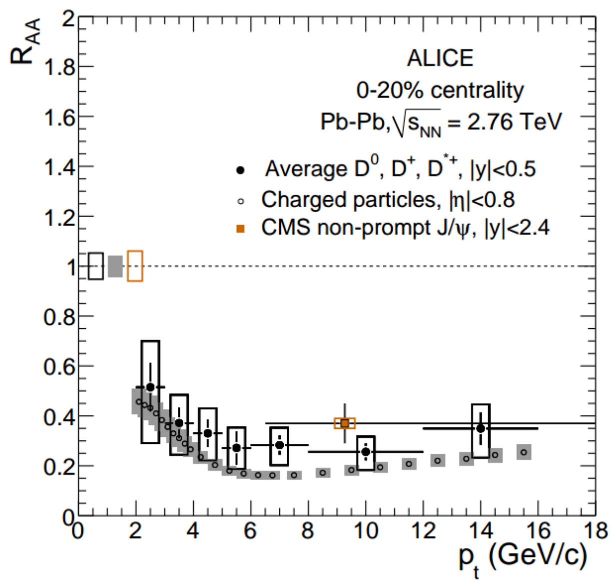

Figure 4.6: Nuclear modification factor R_{AA} of D mesons, charged hadrons and non-prompt J/ψ in Pb–Pb collisions at $\sqrt{s_{\mathrm{NN}}} = 2.76$ TeV in the 0–20% centrality class. Taken from Ref. [45].

At the CMS experiment, suppression of b-jets in Pb-Pb collisions was measured. The results can be observed in Fig. 4.7 for two p_T-bins of b-jets and for different centralities. The larger suppression in central collisions is observed. Smaller b-jet R_AA in central collisions could be caused by redistribution of the energy out of jet cone in Pb-Pb comparing to pp collisions. This could be caused by the medium in central Pb-Pb collisions. Further studies of b-jets are needed, to achieve more clear comparison of energy losses for quarks of different flavours and to compare redistribution of their lost energy. It should not be forgotten, that for more detailed quantitative studies of heavy-ions collisions, the reference proton-nucleus collision studies are needed.

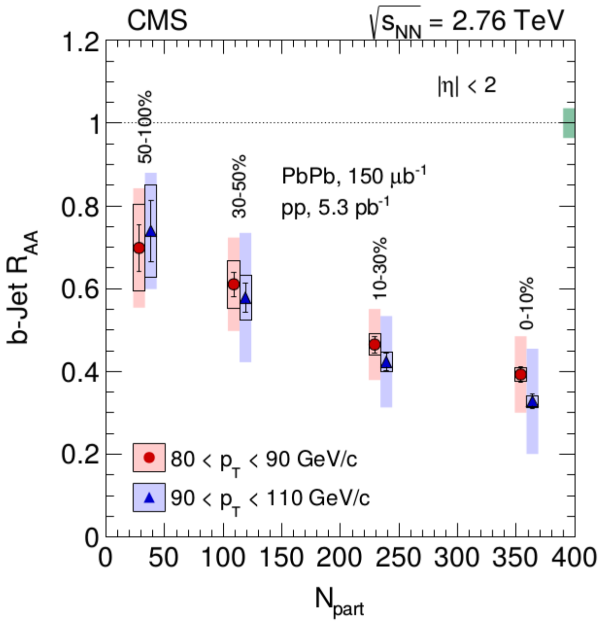

Figure 4.7: Nuclear modification factor R_AA of b jets, as a function of number of participating particles N_part from CMS Pb-Pb collisions at $\sqrt{s_\mathrm{NN}} = 2.76$ TeV, for two jet p_T selections as indicated in the legend. Systematic uncertainties are shown as filled boxes, except the T_AA uncertainties, depicted as open boxes. The luminosity uncertainty is represented by the green box. Taken from Ref. [45].

In summary, heavy-flavour is important probe in high-energy physics. Nowadays, the wide range of measurements is studied, but higher precision is needed to confirm or decline theoretical predictions. Understanding of all collision system at different energies is needed.

Chapter 5

Jets in collisions

Jets are defined as collimated sprays of hadrons, produced via fragmentation of high-energy quarks or gluons. If heavy quark fragmented to form a jet, heavy hadrons are contained in jet after hadronisation. These heavy hadrons decay to light hadrons, which can be also contained in jet cones.

Different types of jets are considered, depending on parton (quark or gluon) from which fragmentation they were formed: usdg-jets (mother particle could be one of light quarks u, s, d or gluon), c-jets (mother particle is c quark) and b-jets (mother particle is b quark). After hadronisation, this particle is contained in relevant hadron, so for example, if mother b quark fragments, after hadronisation, there are some light hadrons and B hadron. The last one decays to lighter hadrons, which are detected.

5.1 Motivation for jet studies

Jets are considered to be one of the most important probes of the partonic medium, that can be created in collisions of heavy ions. In case of pp collisions, jet production can be quite satisfyingly predicted by perturbative QCD (pQCD) calculations and vice versa, so pQCD calculations can be improved by jet measurements. Jets can be also used to study hadronisation and hard scattering. Collisions of protons are also used as reference of measurements in p-Pb or Pb-Pb collisions. In these cases, measured jet productions could be suppressed, mainly for central collisions. This suppression could be expressed by already described nuclear modification factor R_{AA}. Measured R_{AA} for jets in Pb-Pb collision at $\sqrt{s_{NN}} = 2.76$ TeV is shown in Fig. 5.1. Strong suppression for jets can be observed at the level $R_{AA} \approx 0.4$. R_{AA} slowly rises with higher transverse momentum of jet.

By comparing the jet production in pp and Pb-Pb collisions, the properties of produced medium can be studied. These are mainly temperature of the medium, its initial shape or energy loss of particles in it. The last one is expected to be different for gluons, light quarks and heavy quarks due to the dead-cone effect [43]. For b quarks, it is expected to be smaller than for c-quarks, which is smaller than for light quarks or gluons. This energy loss dependence on particle mass is one of our motivations to study heavy-flavour jets. Because of the large mass of b quark, it is expected to be created right after the collision, in hard scattering. So b quarks experience the full evolution of the system, that makes them an excellent probe of medium properties. They enable us to study redistribution of lost energy of quarks in medium or possible modification of b quark fragmentation in medium.

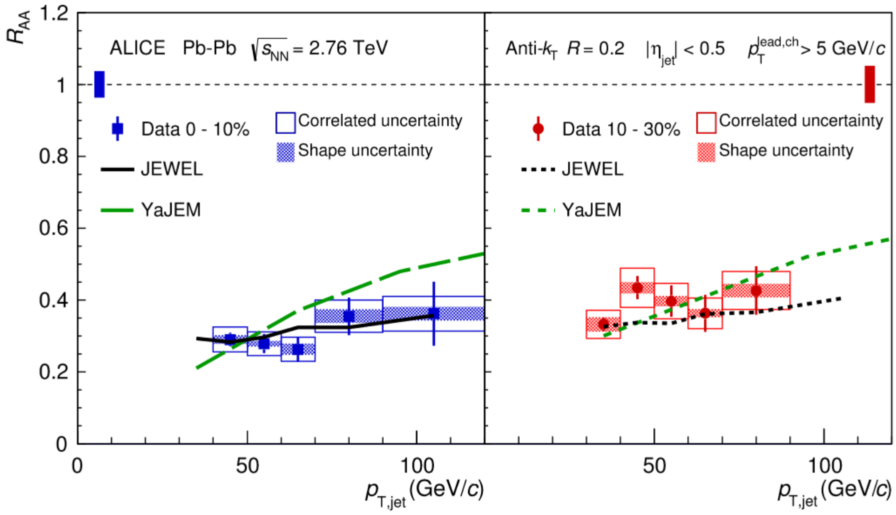

Figure 5.1: Nuclear modification factor R_{AA} of jets reconstructed using anti-k$_T R < 0.2$ and requiring a high p_T leading track, $p_T > 5$ GeV/c in 0–10% (Left) and 10–30% (Right) most central Pb–Pb collisions compared to theoretical calculations from YaJEM [47] and JEWEL [48]. The boxes at $R_{\mathrm{AA}} = 1$ represent the systematic uncertainty on number of binary collisions scaling. Taken from Ref. [35].

5.2 Jet-finding algorithms

Jet reconstruction occurs in space defined by pseudorapidity η and azimuthal angle ϕ. Coordinates of the jet axis in this space are

$$\eta = \sum_i \frac{E_T^i \eta^i}{E_T^J}, \phi = \sum_i \frac{E_T^i \phi^i}{E_T^J}, \tag{5.1}$$

where E_T^J is total transverse energy of jet, η^i and ϕ^i are coordinates of particles in jet and E_T^i are energies of these particles. Transverse energies in definitions could be replaced by transverse momentum p_T.

After tracks and energies of particles in event are reconstructed, different algorithms can be used to find and reconstruct jets. There are different requirements on these algortihms, the most important ones are:

- **Infrared safety:** soft particle should not change number and properties of reconstructed jet.
- **Collinear safety:** in sense of reconstructed clusters, two particles with low energy or mass, propagating close to each other, should not be mismatched as one more energetic particle and vice verse. Analysis of energetic clusters have serious influence on efficiency of jet reconstruction.
- **Order independence:** after reconstructions, resulting jets should be same in parton, hadron and detecter level. This could be tested in MC simulations of collisions.
- **Independence on detector geometry and granularity.**
- **Maximum jet-finding efficiency vs. CPU time.**

5.2.1 Cone algorithms

Cone algorithms firstly look for the most energetic particles (clusters) in η-ϕ space of event. These clusters should have larger energy than set up threshold value, if they do, they are tagged as "seeds". After that, all particles, which distance from the seed is smaller as the threshold value of R ($R = \sqrt{\Delta\eta^2 + \Delta\phi^2}$) are inherited in a jet cone. Then, all particles in the found jet cone are considered to find new seed. It is done via weighted center of actual jet cone. This new seed is used to construct new jet cone, in a same way as before. Process repeats, till some stability of shape of jet or jet axis cone is achieved.

The problem is, that these algorithms are not usually collinear and infrared safe.

5.2.2 Clustering algorithms

Another group of algorithms for jet reconstruction is clustering algorithms. They are based on finding some kind of a weighted distance betweeen particles (i, j) defined as

$$d_{ij} = \min(k_{Ti}^p, k_{Tj}^p)\frac{\Delta_{ij}^2}{D^2}, \tag{5.2}$$

where parameter p defines influence of transverse momentum of particle vs. its geometrical properties, parameter D assures minimal distance between reconstructed jets,

$$\Delta_{ij}^2 = (y_i - y_j)^2 + (\phi_i - \phi_j)^2, \tag{5.3}$$

and k_{Ti} is defined for every particle i as

$$k_{Ti} = \frac{E_i}{c}\sin\theta_i, \tag{5.4}$$

where θ_i is azimuthal angle of particle and E_i is its energy. Then distance between beam and particle i is defined as

$$d_{iB} = k_{Ti}^p. \tag{5.5}$$

In an event, all d_{iB} and d_{ij} are calculated. From these numbers, the smallest one is chosen. If it is one of d_{ij}, particles i and j are merged and later considered as one particle, for which energies, momentum and distances are recalculated. If it is one of d_{iB}, particle i is tagged as jet (in later steps, more particles are "hidden" in this one). This steps are repeated, untill all the particles are part of jets.

Algorithm, that used $p = 2$ is called k$_T$ algorithm, for $p = 0$ it is called C/A (Cambridge/Aachen) algorithm and for $p = -2$ it is anti-k$_T$.

5.3 Heavy flavour jets

Heavy hadrons are decaying in the secondary vertices to multiple daughter particles. Secondary vertices thus share some properties of appropriate hadrons. These properties could be used for tagging different jet flavour containing secondary vertex.

Multiple tracks are therefore coming out from secondary vertices. These tracks are specific for their large displacement from primary vertex (interaction point), thanks to this secondary vertices are found in data. The invariant mass of secondary vertex is

$$m_{inv}^2 = \left(\sum_i E_i\right)^2 - \left\|\sum_i \overrightarrow{p_i}\right\|^2, \tag{5.6}$$

where E_i are energies of particles coming out from secondary vertex and p_i are their momentum. Distance of secondary vertex from primary vertex, L_{xy}, depends on decay length of meson decaying in this vertex.

As already mentioned, b-jets contain B hadrons, mainly B mesons. They are heavy, therefore also the secondary vertices created after they decay have large invariant mass ($\approx$ 5 GeV/c^2). Lifetime of B meson is large, their flight distance is $\approx$ 500 μm. Fig. 5.2 shows the geometrical schema of b-jet. Impact parameter of tracks coming from secondary vertex, as well as decay length of B hadron are important in further studies.

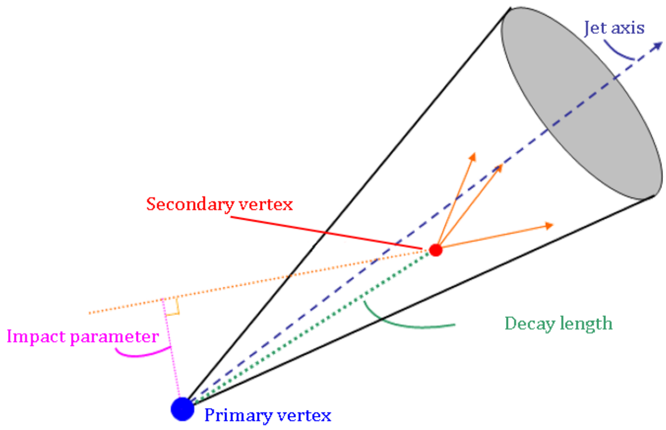

Figure 5.2: Geometry of the jet, showing jet axis, decay length of secondary vertex (L_{xy}) and impact parameter of track (vertex).

5.4 Tagging of b-jets

Studies of b-jet tagging in heavy-ion collisions were already successfully done at the CMS experiment, see Ref. [49]. Algorithms used for b-tagging exploit B meson or b-jet properties described above. For example, simple Secondary Vertex (SSV) algorithm uses properties of secondary vertices in jet, whereas Track Counting (TC) algorithms use properties of tracks in a jet (e.g. large displacement).

In simulated data, "true" number of jets of given flavour could be accessed. These flavours could be identified by different labeling methods, that vary for different simulations implementations. The most used methods look for beauty hadron or quark in given distance from jet axis.

Extracted "true" number of b jets is used for estimation of algorithm performance, expressed by b-tagging efficiency and udsg-jet and c-jets mistagging efficiencies. The efficiency of b-tagging is defined as the fraction of b jets in the sample after applying cuts (tagged sample), divided by the "true" number of b jets in data sample without any cuts. In addition, b tagging purity is fraction of b jets in the tagged sample and total number of jets in the sample.

Efficiency and purity of algorithm thus depend on selected values of discriminating variables. Example of binding of b-tagging and mistagging efficiencies for different values of discriminators and for different b-tagging algorithms is shown in Fig. 5.3. For example, for SSVHP (Simply Secondary Vertex High Purity) algorithm, described in Section 5.4.2, if the working point with b-jet efficiency 40% is chosen, misidentification probability is at the level of 0.05% for light jets and 4% for charm jets. This means, that in the sample selected by such cut, there 40% of all b-jets, 0.05% of all light jets and 4% of all charm jets that are reconstructed. It can be observed, that for all algorithms, higher b-tagging efficiency also means higher mistag efficiencies, that is the natural property of tagging algorithms. On the other hand, higher efficiency of b-tagging results in smaller b-jet purity in tagged sample.

The goal is to set up discriminators in such a way, that c-jets and usdg-jets are rejected, but b-tagging efficiency is high enough.

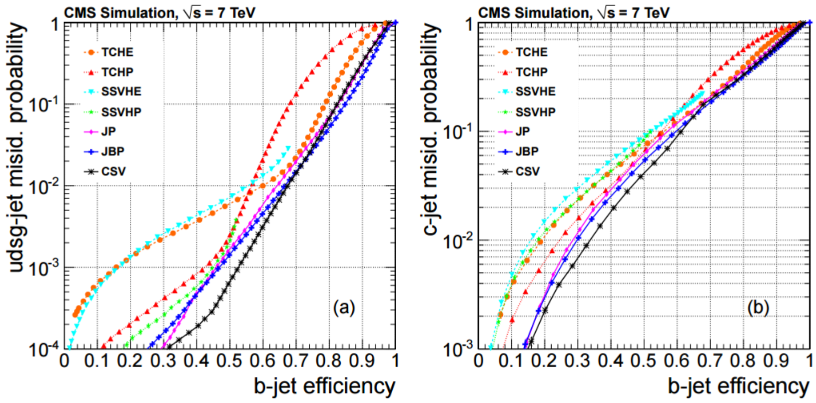

Figure 5.3: On the left usdg-jet and on the right c-jet misidentification probabilities as functions of the b-jet efficiency for b-tagging algorithms at the CMS and for several values of their discriminators, for simulation of pp collisions at $\sqrt{s} = 7$ TeV. Taken from Ref. [49].

5.4.1 Track Counting algorithm

As a first step, impact parameter d_0 of every track in the jet is calculated, then it is projected along the jet axis. Then, these are ordered in decreasing order. The n-th track is chosen and its value of discriminating variable is compared to the threshold value of discriminating variable. If it is bigger than the threshold, jet is tagged as b-jet. As discriminating variable, impact paramater of the track, energy of the track or their combination are usually chosen. At ALICE, usually $n = 3$ and impact parameter as discriminator are used. Typical threshold value is $\approx$ 100 μm. With this value, achieved b-tagging efficiency is ≈ 0.1.

Current results from this algorithm for ALICE MC data are shown in Fig. 5.4. In right column, comparison of b-tagging efficiency and mistagging eficiencies for c-jets and usdg-jets is displayed. In tagging algorithms, our goal is to suppress mistagging efficiency in comparison with b-tagging efficiency. As we can see in Fig. 5.4, usdg-jet mistagging efficiency is suppressed by a factor 10 to 100, c-jet mistagging is by a factor of around 10. Even for small values of transverse momentum of jet, ratio of c-jet mistagging to b-tagging eficiency is around 0.2. We should also be conscious of b-tagging efficiency of 0.1, so with this setup, we are actually able to tag only 10% of real b-jets.

Natural extension of the Track Counting algorithm is the Jet Probability (JP) algorithm, that combines properties of all tracks in jet. For every jet, it calculates estimate that its associated tracks come from primary vertex. This estimate is defined as

$$P_{\text{jet}} = \Pi \cdot \sum_{i=0}^{N-1} \frac{(-\ln \Pi)^i}{i!}, \; \Pi = \prod_{i=1}^{N} \max(P_i, 0.005), \tag{5.7}$$

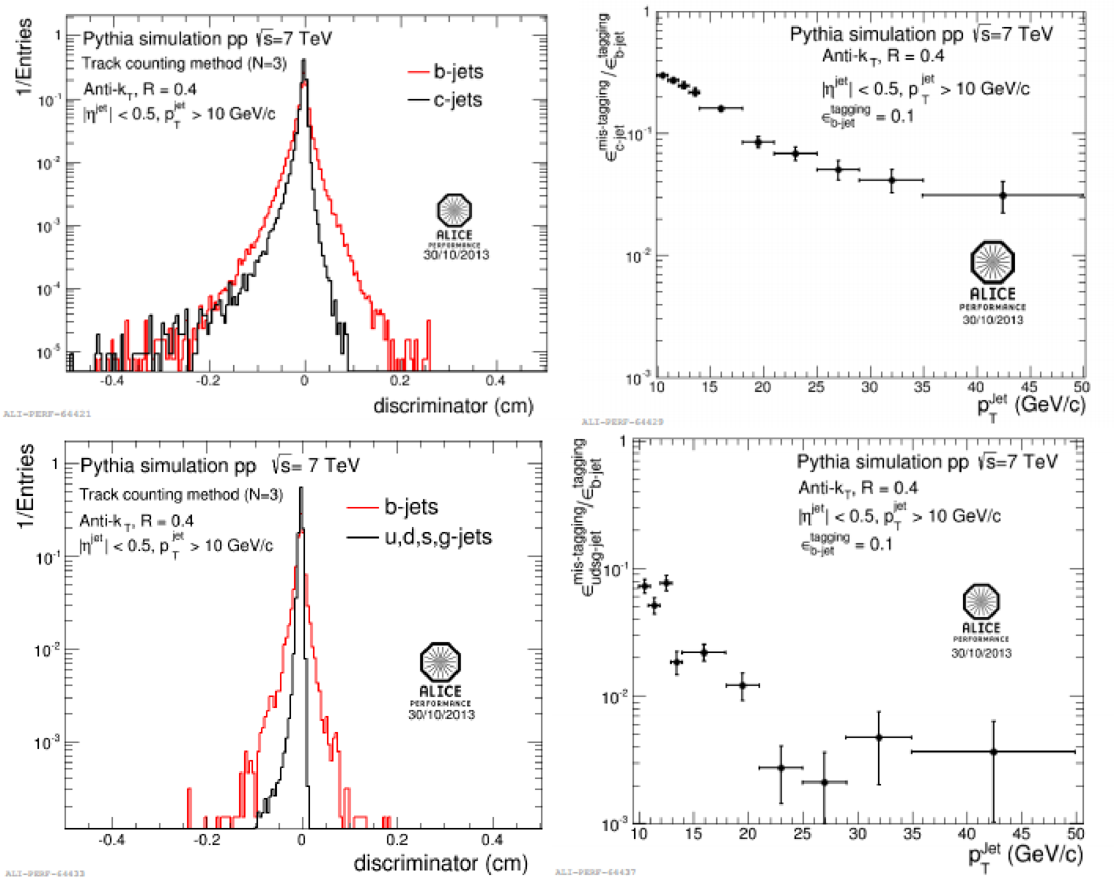

Figure 5.4: Performance of the Track Counting algorithm at ALICE for PYTHIA simulation of pp collisions at $\sqrt{s} = 7$ TeV. First line compares b-jets and c-jets, second line b-jets and usdg-jets. In left column, distributions of impact parameter with respect to jet axis of the third most displaced track in jet (discriminator), in right ratio of other flavour mistagging efficiencies and b-tagging efficiency. Threshold value for the third most displaces track in Track Counting was 100µm. Taken from Ref. [24].

where N is the number of considered tracks and P_i is the probability for the track i to come from the primary vertex. Probability distributions of the significance of track impact parameter are used for calculations of P_i, more details in [50].

5.4.2 Simply Secondary Vertex algorithm

Firstly, all secondary vertices in events are reconstructed. Secondary vertex is calculated as the point, for which the sum of the distances to the three (high purity - SSVHP) or two ((high efficiency - SSVHE)) tracks is minimum. The choice of number of tracks depends on analysis strategy and data statistics.

Then, from all secondary vertices in jet, only secondary vertex with the furthest distance from primary vertex is chosen. For b-tagging, different properties of these secondary vertices could be used. Discriminating variables exploit properties of beauty-hadron decays, i.e. their long lifetime and large mass. Thus natural discriminating variables are the secondary vertex invariant mass, distance from primary vertex (flight distance) or a combination of the two.

Another variable used as a discriminator is the significance of flight distance of secondary vertex in a transverse plane. The sign of the secondary vertex flight distance is defined w.r.t. the jet direction, so the signed length is

$$L = |\vec{L'}|\mathrm{sign}(\vec{L'} \cdot p_{jet}), \tag{5.8}$$

where $\vec{L'}$ is the secondary vertex position. The significance of flight distance in a transverse plane xy is then defined as

$$SL_{xy} \equiv \frac{L_{xy}}{\sigma_{L_{xy}}}, \tag{5.9}$$

where $\sigma_{L_{xy}}$ is uncertainty of L_{xy} reconstruction.

Last but not least, variable describing quality of vertex reconstruction is the secondary vertex dispersion, defined as

$$\sigma_v tx \equiv \sqrt{\sum_i d_i^2}, \tag{5.10}$$

where d_i are the distances of the tracks, used for reconstruction of studied secondary vertex, from secondary vertex in 3D .

Then, selection criteria are applied on the chosen secondary vertices to construct (b-)tagged sample, that is expected to have reduced number of light jets. Purity (fraction of b-jets in tagged sample) of this cut has a significant influence on further b-tagging efficiency. High purity of b-jets in this sample simplifies extraction of the number of b-jets in it. For this, different techniques are used - usually, it is fitting of the secondary vertex mass or distance from primary vertex distributions in tagged sample by three components. These components represent three flavours of jets - light, charm and beauty. They are extracted from simulations. In this fitting, shapes of three distributions are fixed, but their relative contribution is allowed to float. In case of b-jets, these contribution correspond to b purity p_b in sample.

5.5 Results of b-jet tagging by secondary vertices from the CMS experiment

The CMS detector has unique capabilities to reconstruct b jets, as it can be seen in Ref. [49]. I would like to show analysis combining tagging by secondary vertices and template fitting methods in the same collision systems as studied at the ALICE experiment. Analysis steps in this procedure are in principal also the same as the one used at the ALICE experiment, described in Chapter 6.

In analysis of b jets in p-Pb collisions at $\sqrt{s_{\mathrm{NN}}} = 5.02$ TeV at the CMS [50], jets are clustered by anti-k$_T$ algorithm with a parameter $R < 0.3$. Particles are identified using wide range of detection system, where tracking detectors cover the pseudorapidity interval $|\eta_{\mathrm{lab}}| < 2.4$ and calorimeters $|\eta_{\mathrm{lab}}| < 3$. Background and jet energy corrections are also applied to measured jet transverse momentum. Pythia, tune Z2 is used to simulate dijet events, that are then embedded into p-Pb background event, simulated by Hijing. Secondary vertices are reconstructed using charged tracks in jets. Those secondary vertices, that are compatible with decays of $\mathrm{K}^0_{\mathrm{S}}$ and with flight distance larger than 2.5 cm are rejected.

Secondary vertex significance of distance of flight is chosen as discriminating variable in this algorithm. To construct tagged sample of jets, value 2 of this discriminator is used. In this analysis, both data-driven and MC based b tagging efficiencies are studied. MC based efficiency is based on dividing the number of b-jets in tagged sample and the overall number of b-jets. In the case of data-driven method, information from Jet Probability algorithm are used and the procedure is as follows: Tagged sample is constructed using JP discriminator, resulting secondary vertex mass distribution is in Fig. 5.5 (Left), number of b-jets is extracted via template fitting. Then additional SSV cut is applied on the JP tagged sample, resulting secondary vertex mass distribution is in Fig. 5.5 (Right) and again number of b-jets is extracted via template fitting. The two obtained b-jet numbers are compared and used to study the performance of algorithm, shown in Fig. 5.6 (Left). As can be observed in Fig. 5.5, additional cut on discriminator in SSV tagger rejects jets with low value of the jet probability discriminator, thus it enhances b-jet purity in the sample.

After this performance study, tagged sample is constructed only with the cut on the discriminator of SSV tagger. The working point with 65% b tagging efficiency is chosen. Tagged samples are constructed in different p_{T} bins and template fitting is applied on all of them. From calculated purities and efficiencies, distribution of number of b jets, as well as the production cross section are gained. This could be used to calculate nuclear modification factor $R_{\mathrm{pA}}^{\mathrm{PYTHIA}}$ (displayed in Fig. 5.7), where as reference, simulated pp collisions were taken. This study results in small enhancement in b jet production, mainly for low p_{T}. For higher p_{T}, nuclear modification factor is consistent with 1 and with pQDC theoretical predictions.

Last but not least, b jet fraction in p-Pb data is extracted in this analysis and it is presented in Fig. 5.8. The result is 3-4%, nearly same as in the case of pp collisions [51]. This also supports an idea, that b production is not largely affected by the Cold Nuclear Matter, created in p-Pb collisions. These measurements are baseline for further studies of b-jets in other collisional systems and energies.

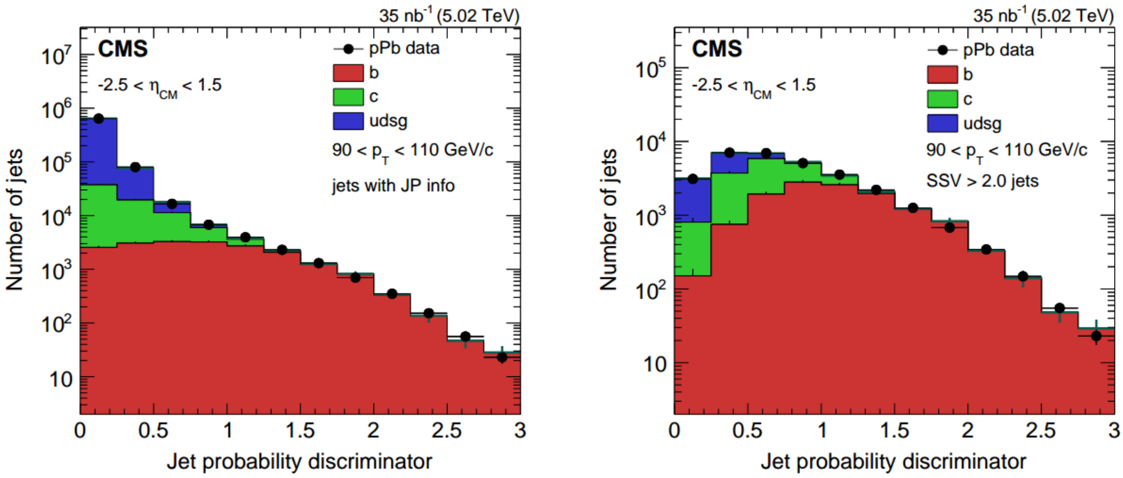

Figure 5.5: Distributions of the Jet Probability tagger discriminator before (Left) and after (Right) applying the SSV tagger selection. Filled black points are data, while the colored histograms denote contributions from simulated b, c, and light-flavor jets in red, green and blue, respectively, obtained from a fit to data. Statistical uncertainties from data are in black, while statistical uncertainty from the templates are shown in dark green. Taken from Ref. [50].

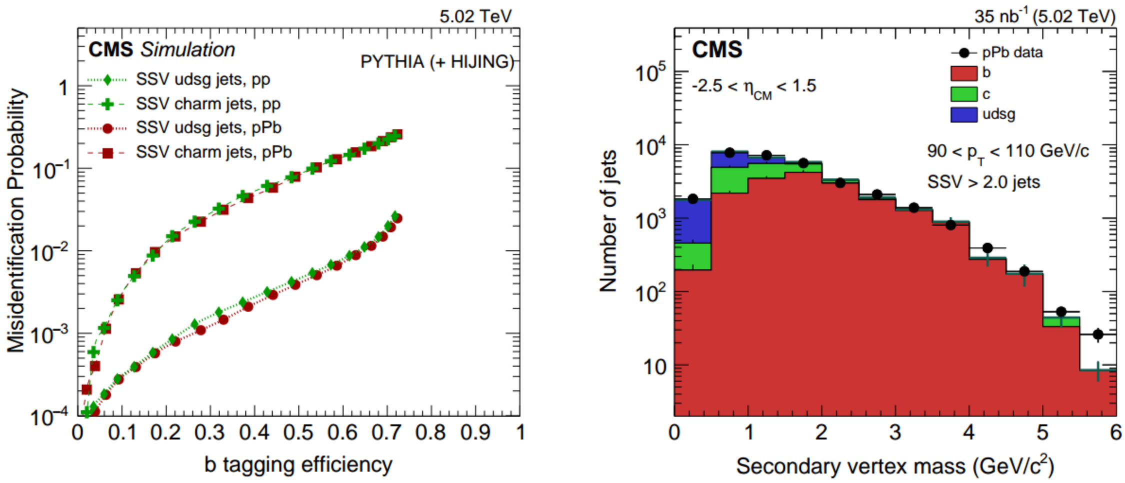

Figure 5.6: The left panel shows the likelihood of misidentifying a light-flavor (circles and dotted lines) or charm (squares and dashed lines) jet as a b jet, as a function of the b tagging efficiency. Shown is the SSV tagger for p-Pb (purple) and pp (green) collisions. The right panel shows a template fit to the secondary vertex invariant mass distribution in p-Pb collisions for jets with $90 < p_\mathrm{T} < 110$ GeV/c. Filled black points are data, while the colored histograms denote distributions of b, c, and light-quark jets in red, green and blue, respectively, extracted from the fit to data. Statistical uncertainties from data are shown as black vertical bars, while statistical uncertainties from the templates are shown as dark green vertical bars around the sum of the templates. Taken from Ref. [50].

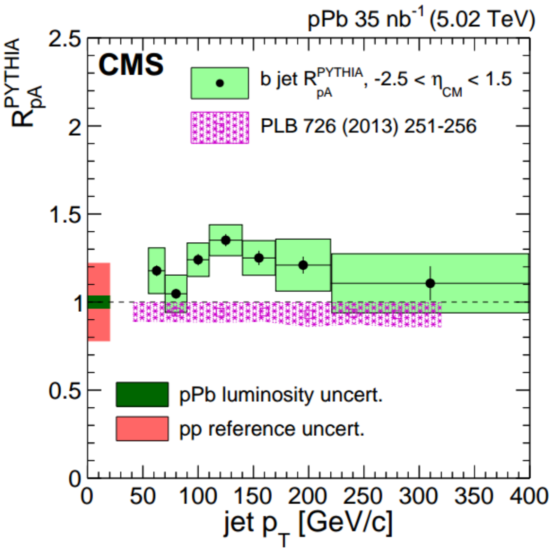

Figure 5.7: The b-jet suppression factor $R_{\mathrm{pA}}^{\mathrm{PYTHIA}}$ as a function of jet transverse momentum p_{T} is shown as points with filled boxes for systematic uncertainties. The pp reference and integrated luminosity uncertainties are shown as red and green bands around unity, respectively. A pQCD prediction is also shown. Taken from Ref. [50].

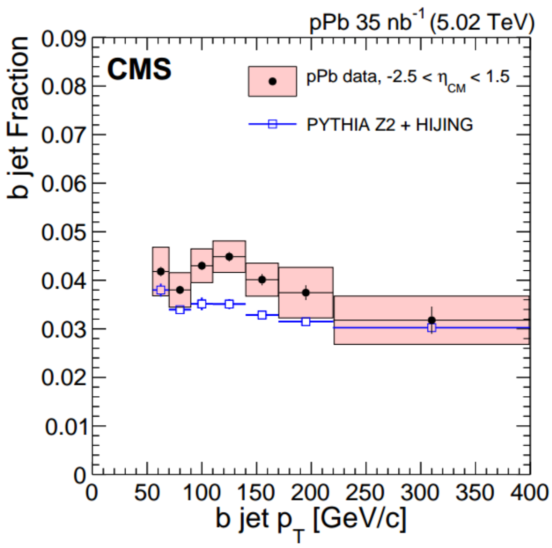

Figure 5.8: The b-jet fraction is shown for p-Pb data as filled black circles surrounded by filled boxes for systematic uncertainties. A simulation from the Z2 tune of Pythia+Hijing at $\sqrt{s_{\mathrm{NN}}} = 5.02$ TeV is also shown as open blue boxes. Taken from Ref. [50].

Chapter 6

Performance of the ALICE secondary vertex b-tagging algorithm

In this chapter, reconstruction of b-jets in p-Pb collisions at $\sqrt{s_{\mathrm{NN}}} = 5.02$ TeV recorded in the year 2013 by ALICE experiment is discussed. Our goal is to develop, test and tune b-tagging analysis in order to obtain the best possible precision for ALICE detector. Obtained b-jet spectra and b-jet fraction are compared to the results from other experiments.

At ALICE, there are no results from b-jet studies yet (only first estimation of heavy-flavour lepton suppression), this analysis is in this respect unique. In ALICE collaboration, alternative method of b-tagging based on displaced tracks (Track Counting method) is developed as well .

This analysis exploits properties of beauty-hadron decays, in a way of reconstructing places of such decays - secondary vertices (described in Section 5.3). For this, track selection suitable for b-tagging is needed. Next step in analysis is jet reconstruction from these tracks. The underlying background is then subtracted under the jet area. Once jets and secondary vertices are reconstructed, the tagging with a particular algorithm is done. Finally the resulting spectra of b-jets should be corrected not only on the efficiency and purity of tagging algorithm, but also on the further detector effects. Systematic errors have not yet been estimated.

This work was performed within the ALICE Physics Analysis Group - Heavy-flavour Correlations and Jets.

6.1 Data and event selection

At ALICE, data recorded by detectors are prepared for physical analysis centrally in reconstruction passes. Reconstruction pass normally comes after the calibration and validation passes. If some problem or possible improvement is found in a given reconstruction pass (e.g. improvement of the detector tracking), then it is decided to reconstruct the full data set again. At this point, also the MC production has to be redone with the same reconstruction pass in order to anchor to the corresponding data. In other words, if calibration files changed for data, they have to be the same for the MC simulations.

After this phase, analysis code, prepared by Physics Working Groups, is processed on reconstructed data or MC simulations. This is usually done centrally at the CERN's Worldwide LHC Computing GRID. In our analysis, results of this phase are C++ object holders, so called containers. They contain information about reconstructed jets and their properties. This is an input to my analysis, technically a preparation of complex analysis macro was needed. Histograms and plots presented in this thesis are results of this analysis macro, built for AliRoot. AliRoot is the ALICE off-line framework for simulation, reconstruction and data analysis, based on the ROOT[1], on which the framework and applications are built.

For b-tagging in data from collisions, detailed understanding of algorithm performance is needed. This is tested in MC simulations of collisions. In this analysis, simulation of p-Pb collisions at $\sqrt{s_{\mathrm{NN}}} = 5.02$ TeV are used. These are represented by the mix of PYTHIA6 (Perugia 2011) [52] and HIJING [53] event generators. PYTHIA simulates hard physics in collisions, whereas HIJING corresponds to p-Pb background. Since jets are analyzed, to enhance simulated statistics, jet (LHC14g3b) and heavy-flavour (LHC14g3a) enhanced production are used. Jet enhanced production assures, that in every event, at least one pair of jets is generated. In the case of heavy-flavour enhanced production, at least one pair of heavy quark and corresponding antiquark is generated in every collision. Two heavy-flavour enhanced productions are analyzed: charm-enhanced, where charm-anticharm pair is generated, and beauty-enhanced, where beauty-antibeauty pair is generated. In total, 20 millions of heavy-flavour enhanced simulated events and 60 millions jet enhanced simulated events are analyzed. Both MC simulations, LHC14g3a and LHC14g3b are anchored to recorded p-Pb data.

Since spectrum of jets has a steeply falling shape, simulated events were generated in four hard-p_{T} bins, to provide sufficient statistics even for large transverse momentum jets. Without generating in hard bins, very large number of events would have been generated. Every hard-p_{T} bin represents given interval of transferred momenta in hard scattering. In this study, these intervals were aplied:

- for beauty enhanced sample: 10-18 GeV/c, 18-30 GeV/c, 30-50 GeV/c and more than 50 GeV/c,
- for charm enhanced sample: 10-20 GeV/c, 20-50 GeV/c and more than 50 GeV/c,
- for jet enhanced sample: 11-21 GeV/c, 21-36 GeV/c, 36-57 GeV/c and more than 57 GeV/c.

Events in hard bins were appropriately scaled, to obtain cross sections of variables that can be summed to create continuous spectra of jets.

Detector simulations are important in our study in order to understand detector effects on jet reconstruction and for right comparison of simulation results with those from data. GEANT3 [54] is used to implement response of the ALICE detector. Collisions of protons at $\sqrt{s} = 5.02$ TeV, simulated by PYTHIA6, with tune Perugia 2011 with a Lorentz boost (to get the same rapidity shift as in p-Pb collisions), are used to study detector response for jets without underlying event.

For data analysis, p-Pb collisions at $\sqrt{s_{\mathrm{NN}}} = 5.02$ TeV recorded during Run 1 are studied. Analysed productions are LHC13b and LHC13c after pass 4, which is the newest reconstruction pass available. Analysed data were recorded using minimum-bias trigger, that required the arrival of colliding bunches from both directions and signal in both scintillators of V0 detector (in pseudorapidity covarage $2.8 < \eta < 5.1$ and $-3.7 < \eta < -1.7$). Timing information from V0 and Zero Degree Calorimeters was used for off-line event selection, to remove background from beam-gas interactions. Events with primary vertex

[1] ROOT is modular scientific software developed for big data processing, statistical analysis, visualization and storage of data.

reconstructed less than 10 cm from the center of the detector along beam line were considered. This selection criteria resulted in approximately 100 milions of events analysed.

6.2 Analysis procedure

6.2.1 Track selection

Study of b-jet tagging requires optimized track selection. The track selection is the same in data and in MC simulations. Charged tracks with transverse momentum $0.15 < p_{\mathrm{T}} < 100$ GeV/c, reconstructed in rapidity region $|\eta| < 0.9$ by ITS and TPC detectors are used. Some regions in SPD are inefficient, thus azimuthal distribution of tracks reconstructed using SPD information is not completely uniform. Therefore, also tracks without SPD requirements are used. Tracks reconstructed in TPC are required to have more than 70 (out of 159) points in TPC. These tracks are used for jet reconstruction. Tracks, that are used for secondary vertex reconstruction, are in addition required to have at least one point in SPD and $p_{\mathrm{T}} > 1$ GeV/c.

6.2.2 Jet reconstruction

Firstly, described reconstructed charged tracks are used for charged jet reconstruction. This is done using the anti-k_{T} algorithm from the FastJet package [55] with resolution parameter of $R = 0.4$. For that jets are fully located in the TPC acceptance, only those having axis in pseudorapidity interval $|\eta_{\mathrm{jet}}| < 0.5$ are considered. Then, for the estimation of the background density and fluctuations in jet reconstruction, a similar approach to the one applied by ALICE jet group for charged jet measurements in p-Pb collisions [56] is used. The background fluctuations under the jet area are found to be slightly smaller in the HIJING simulation than in the p-Pb data [56].

The background density ρ is calculated also in the same way in Ref. [56]. This method is well-suited for sparse environment in p-Pb collisions. This approach reconstructs cones using k_{T} algorithm from FastJet package and uses their transverse momentum $p_{\mathrm{T},i}$ and area A_i to calculate constant background density

$$\rho = \text{median}\left(\frac{p_{\mathrm{T},i}}{A_i}\right) C, \tag{6.1}$$

where C is the correction factor for the empty clusters.

The constant background density is subtracted event by event from each jet in the event. However, in reality, this background is not constant and differs for different jets in a given event. A random cone approach is applied to estimate background fluctuations. Resulting background fluctuations are thus

$$\delta p_{\mathrm{T}} = \sum_i p_{\mathrm{T},i} - A_{cone} \cdot \rho, \tag{6.2}$$

where the sum is over the track p_{T} in a cone and A_{cone} is the cone area. These fluctuations are used for construction of background fluctuation matrix, used in unfolding of the jet momentum distribution (see Section 6.2.6). For more details see Ref. [56].

Labeling of b-jets in MC simulations is done via search of beauty hadron in a cone $\Delta R < 0.7$ around the jet axis. If no beauty hadron, but the charm one is found in such cone, jet is tagged as charm jet. If no heavy hadron is found in the jet cone, jet is tagged as light-flavour (udsg) jet.

In simulated events, the jet finder algorithm is being run at both particle and detector level, thereafter these jets are matched. Therefore, both information on jets before and after passing detector are accessible. Efficiencies, purities and spectra are reconstructed at both levels, mainly for consistency checks and further corrections. In what follows, jets at the reconstructed level (after detections) are considered. In our studies, jet p_{T} with background rejection is always used.

6.2.3 Secondary vertex reconstruction and properties

This analysis calculates secondary vertex as the point of the closest approach of three tracks. These tracks should belong to jet and should have at least one point in SPD and $p_{\mathrm{T}} > 1$ GeV/c. Once secondary vertices are reconstructed, their properties are used to tag b-jets. For every jet, only the secondary vertex with the largest distance from interaction point is considered. Jets with no reconstructed secondary vertex inside are not considered in this analysis.

In Fig. 6.1, basic properties of secondary vertices, reconstructed in MC simulations for $20 < p_{\mathrm{T,jet}} < 50$ GeV/c are showed, their invariant mass and signed flight distance. Distributions for beauty, charm and light jets have clearly different shapes. It could be observed, that the properties of B hadron decays cause, that distribution of secondary vertex mass and flight distance for b-jets are more broaden than distributions for charm and light jets.

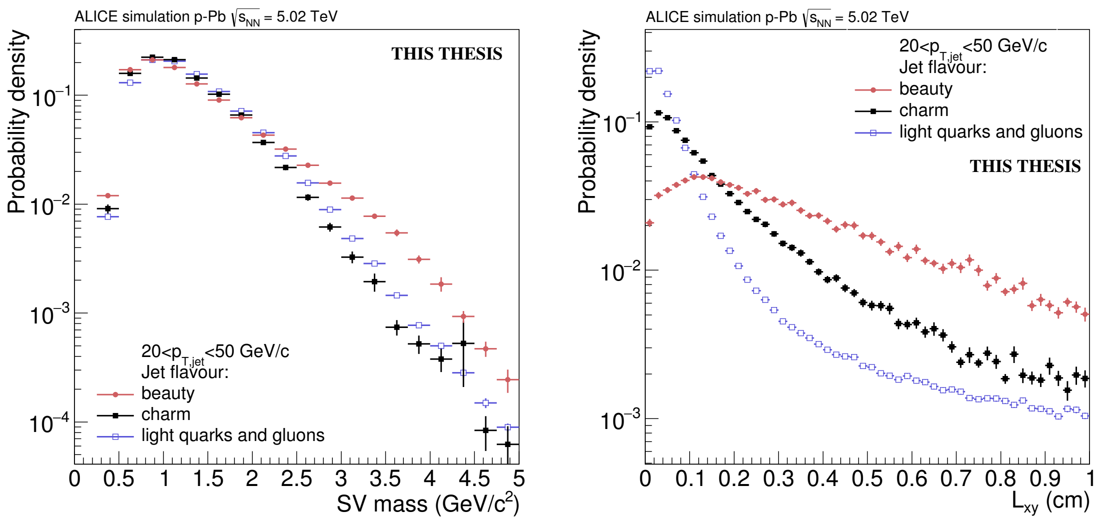

Figure 6.1: Probability distribution of mass (Left) and the signed flight distance L_{xy} of the most displaced secondary vertex (Right) found in charged jets with transverse momentum $20 < p_{\mathrm{T,jet}} < 50$ GeV/c in p-Pb simulations at $\sqrt{s_{\mathrm{NN}}} = 5.02$ TeV from Pythia+Hijing. Distributions are plotted for beauty (red circles), charm (full black rectangles) and light (open blue rectangles) jets. Beauty and charm jet distributions are reconstructed from b-enhanced and c-enhanced productions respectively, light and gluon jet are reconstructed in jet-enhanced production.

Properties of secondary vertices, used for b tagging in this analysis are significance of signed flight distance SL_{xy} and secondary vertex dispersion σ_{vtx} of secondary vertex, both described in Section 5.4.2, page 55, Equations 5.9 and 5.10. Distributions of these properties in our MC simulation data are shown in Fig. 6.2. For both discriminators, different shapes for different jet flavours could be observed. Vertex dispersion distribution, shown in the left panel of Fig. 6.2 shows, that in general for heavy jets it has larger values. Most likely explanation of such uncertainty is, that secondary vertices in the light jets have tracks, which come from the primary vertex, therefore the secondary vertex dispersion is good, because all tracks come from the same point. For charm and beauty jets, we are firstly tagging them as charm or beauty in MC simulations, and then we take the most displaced secondary vertex in them. For beauty jets, there are tracks also coming from the decays of D mesons from B decays. Both for charm and beauty jets, it is possible, that the three tracks do not necessarily come from the B or D decay but rather from the beauty or charm quark fragmentation, being therefore less close by reconstructed secondary vertex. For secondary vertex dispersion smaller than 0.02 cm, shapes of the distributions are nearly the same for all jet flavours. The aim is to keep well-reconstructed secondary vertices, in order to keep measurements precise, however by applying the strict cut on secondary vertex dispersion, we loose large number of b-jets.

Significance of signed secondary vertex flight distance SL_{xy} is a discriminating variable exploiting beauty-hadron decay properties. Requirement on minimal value of SL_{xy} in selection cuts rejects secondary vertices with small distance from primary vertex or poorly reconstructed ones (with large relative uncertainty). As it can be observed in Fig. 6.2 (Right), probability density of SL_{xy} for heavy flavour jets is clearly different from the one for light quark and gluon jets. For $SL_{xy} < 30$, probability density of SL_{xy} for b-jet is falling by an order of magnitude, while distribution for light jets is falling by more than two orders. For c-jets, probability density is falling by nearly two orders, but the shape is more broaden as in the case of light jets. In addition, small ridge for SL_{xy} < 5 is observed for light and charm jets, but it is not present in distribution for b-jets. Distribution for b-jets is more broaden than for other flavours. For example, $\approx 2\%$ of b-jets a have of value $SL_{xy} = 20$, but only 0.2% of light and 0.5% of charm jets have this value. This shows the power of SL_{xy} to suppress contamination of light jet flavours in tagging. This property makes SL_{xy} a great variable for b-tagging.

Discriminating variables used in this analysis are complementary in such way, that cut on minimal SL_{xy} enhances sample with secondary vertices with large displacement and cut on maximal secondary vertex dispersion rejects those, that are reconstructed with a good relative uncertainty but with a large absolute value of uncertainty.

In all figures in this section, secondary vertex dispersion σ_{vtx} is in centimeters, although it is not written in the plots for better readability.

Tests, showing if MC simulations generate the same shape of secondary vertex properties distributions as the data, are needed and they are partially presented in Fig. 6.3 for secondary vertex mass, in one of the selected p_{T} intervals for different cuts on discriminating variables (dispersion of secondary vertex and significance of signed flight distance of the secondary vertex). Distributions in this figure are rescaled, so that the corresponding shapes are easy to compare. In case of MC, results from jet-enhanced sample are shown. In such comparison, e.g. rescaling and summing of distributions generated in p_{T} hard bins is tested, as well as the description of heavy-flavour production by PYTHIA (since after chosen selection criteria, tagged samples are expected to have large b-jet purity and suppression of light jets). For the distribution with no cuts applied and for the three tagging criteria, only small differences are observed (Fig. 6.3). It seems that simulation described data satisfactorily. Also some of the small "ridges" and structures are the same in data and simulations. Small differences between data and simulated events are still expected, since it is well-known, that PYTHIA does not reproduce heavy-flavour production well. Differences, coming from this inconsistency, should be more evident for tighter cuts on discriminating variables, for which higher purity of heavy-flavour jets is expected.

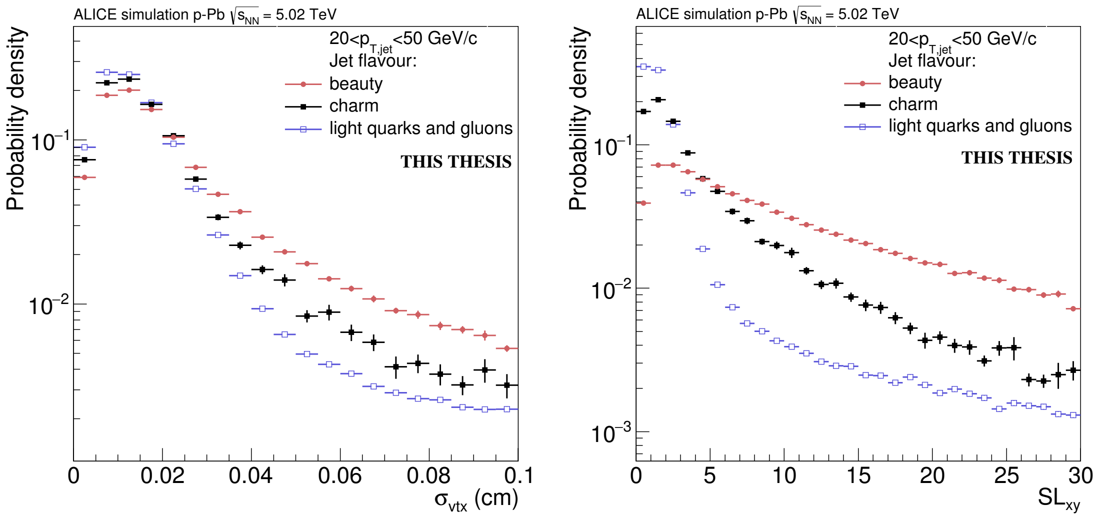

Figure 6.2: Probability distribution of the dispersion σ_{vtx} (Left) and the signed flight distance significance SL_{xy} of the most displaced secondary vertex (Right), found in charged jets with transverse momentum $20 < p_{\mathrm{T,jet}} < 50$ GeV/c in p-Pb simulations at $\sqrt{s_{\mathrm{NN}}} = 5.02$ TeV from PYTHIA+HIJING. Distributions are plotted for beauty (red circles), charm (full black rectangles) and light (open blue rectangles) jets. Beauty and charm jet distributions are reconstructed from b-enhanced and c-enhanced productions respectively, light and gluon jet are reconstructed in jet-enhanced production.

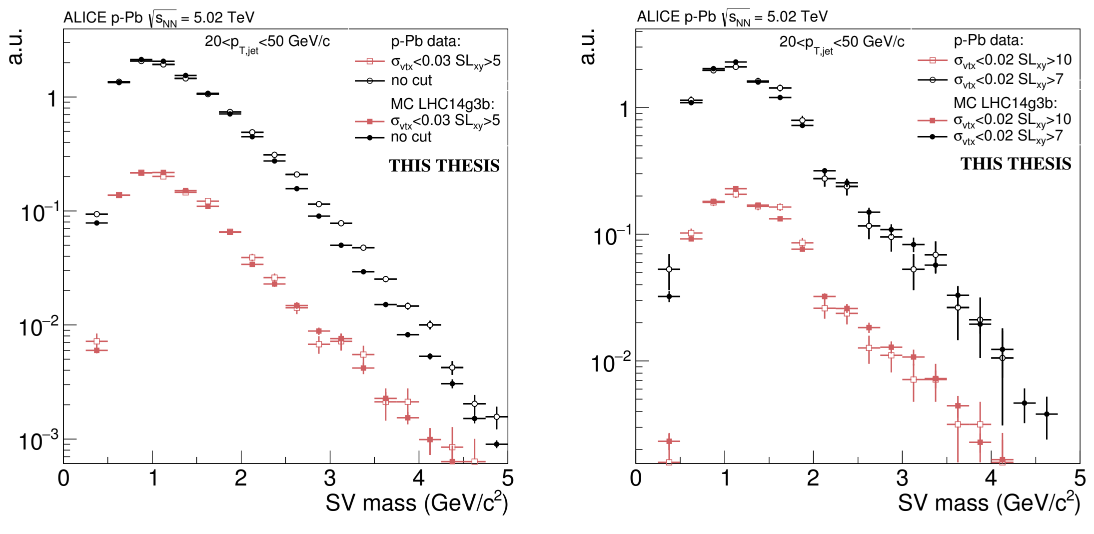

Figure 6.3: Comparison of the invariant mass distribution shape of the most displaced secondary vertex in the charged jet with transverse momentum $20 < p_{\mathrm{T,jet}} < 50$ GeV/c in different samples, tagged by various secondary vertex dispersion σ_{vtx} and signed flight distance significance of the secondary vertex SL_{xy} and in sample with no cuts applied, in simulated jet enhanced p-Pb collisions from PYTHIA+HIJING and in p-Pb data, both at $\sqrt{s_{\mathrm{NN}}} = 5.02$ TeV. Distributions are scaled, in order to clearly compare shapes of tagged sample in data and simulations.

6.2.4 Tagging of b-jets

Different jet p_{T}-bins and selection criteria are studied. The goal of the ALICE is to study b-jets in momentum range $20 \lesssim p_{\mathrm{T}} \lesssim 60$ GeV/c. This is the region that is complementary to other LHC experiments. We will study performance of b-tagging algorithm in order to select the optimal jet p_{T}-bins. As a first step, tagging and mistagging efficiencies for wide range of cuts on discriminating variables are investigated. The goal is to find working point having contamination of light jets suppressed by 2 orders of magnitude and charm jets by at least one order of magnitude suppressed in comparison with b-jet efficiency. These assumptions are based on measurements of the CMS experiment, where b jets to inclusive jets fraction is at the level of 2-4%, both in pp collisions at $\sqrt{s} = 7$ TeV [51] and in p-Pb collisions at $\sqrt{s_{\mathrm{NN}}} = 5.02$ TeV [50] (Fig. 5.8).

In our analysis, efficiencies are based on calculations in simulations, thus for b-jet efficiency, number of b-jets in sample after selection criteria is compared with overall number of b-jets. For estimation of beauty, charm and light (mis)tagging efficiencies, corresponding simulated data are used - beauty efficiency is estimated in beauty enhanced sample, charm in charm enhanced and light in jet enhanced sample. Mis-tagging rate vs b-jet efficiency for jet transverse momentum $20 < p_{\mathrm{T,jet}} < 50$ GeV/c is shown in Fig. 6.4. Sensitivity of cuts is presented in two ways: the lines on the left panel of Fig. 6.4 are for fixed cut on SL_{xy} and for every line, points represent different cuts on secondary vertex dispersion from 0.01 cm to 0.07 cm. In the right panel, it is vice versa - lines are for fixed secondary vertex dispersion, while points represent cuts on SL_{xy} from 3 to 12.

The natural behavior of algorithm performance is observed - cuts with large b-jet efficiency have also larger contamination from other flavours. For the b-jet efficiency 35%, observed the mistagging rate is $\approx 10\%$ for charm and $\approx 0.6\%$ for light jets for all of the cuts. This selection cut thus satisfies requirement of the suppression of both charm and light contaminations. For samples with b-jet efficiency higher than 35%, the contamination of charm jets starts to be critical, and for samples with very high b-jet efficiencies, light jets are not suppressed enough. To obtain large b-purity in the tagged sample, cuts with lower b-jet efficiency, around the middle of efficiencies plotted in Fig. 6.4, are used.

For further studies, three different selection criteria are chosen to construct and study three tagged samples. From the loosest one to the tightest they are:

- dispersion of the secondary vertex $\sigma_{vtx} < 0.03$ cm, significance of signed flight distance of secondary vertex $SL_{xy} > 5$,
- dispersion of the secondary vertex $\sigma_{vtx} < 0.02$ cm, significance of signed flight distance of secondary vertex $SL_{xy} > 7$,
- dispersion of the secondary vertex $\sigma_{vtx} < 0.02$ cm, significance of signed flight distance of secondary vertex $SL_{xy} > 10$.

Mistagging (charm and light) and b-tagging efficiencies for these cuts vs p_{T} are displayed in Fig. 6.5. The two tightest cuts have satisfying suppression of light-flavour by 2 orders of magnitude and nearly satisfying suppression of charm. The loosest cuts have large contamination of both, but it is chosen because of the small statistics.

The loosest cut, $\sigma_{vtx} < 0.03$ cm and $SL_{xy} > 5$, is chosen in order to obtain as large statistics in the tagged sample as possible. Resulting b-jet efficiency is $\approx 40\%$, charm misidentification is large, around 10-20% and the light misidentification is not larger than 2%. Therefore, this cut does not suppress both light and charm jets in the tagged sample satisfactorily.

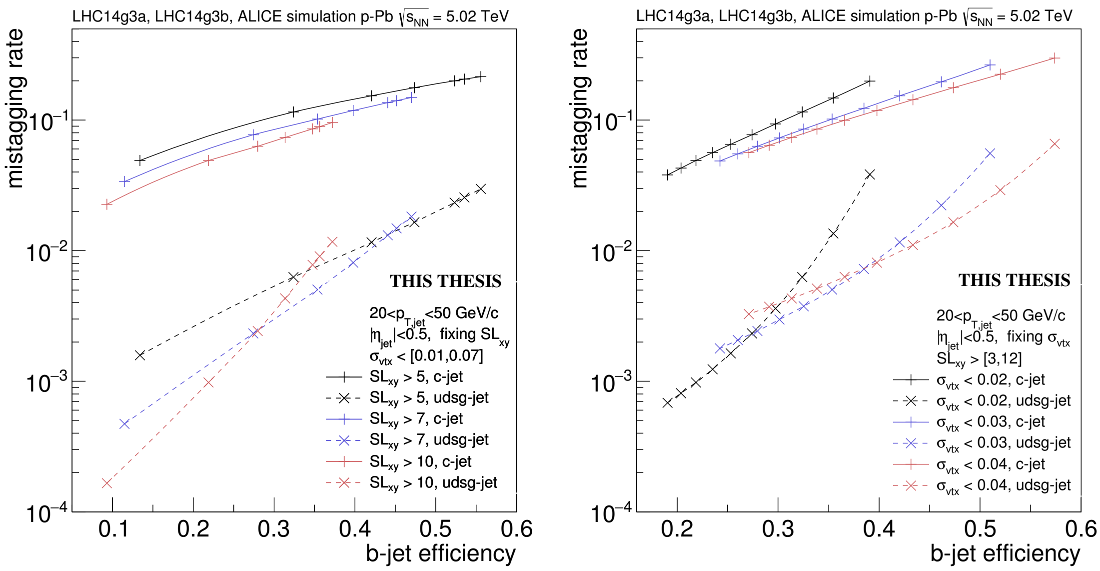

Figure 6.4: Mistagging rate of charm jets (full line) and light jets (dashed line) vs the b-tagging efficiency of the secondary vertex tagging algorithm for different operating points for jet transverse momentum range $20 < p_{\mathrm{T,jet}} < 50$ GeV/c. Left: Curves corresponds to different fixed cuts on the secondary vertex signed flight distance significance SL_{xy} and points represents secondary vertex dispersion σ_{vtx} cuts from 0.01 cm to 0.07 cm. Right: Curves correspond to different fixed cuts on the secondary vertex dispersion σ_{vtx} and points represent the secondary vertex signed flight distance significance SL_{xy} cuts from 3 to 12. Efficiencies are extracted from simulated jet enhanced p-Pb production at $\sqrt{s_{\mathrm{NN}}} = 5.02$ TeV (LHC14g3b) in the case of light jets and from simulated heavy-flavour enhanced p-Pb production at $\sqrt{s_{\mathrm{NN}}} = 5.02$ TeV (LHC14g3a) in case of charm and beauty jets. Simulated events are generated by Pythia+Hijing.

However, the tightest cut, $\sigma_{vtx} < 0.02$ cm and $SL_{xy} > 10$, suppresses light efficiency to 0.09% for jet transverse momentum $p_{\mathrm{T}} = 20$ GeV/c. This is slowly growing with p_{T} up to 0.15% for $p_{\mathrm{T}} = 60$ GeV/c. For this cut, b-jet efficiency is $\approx 20\%$, that is 2 orders of magnitude higher than the light efficiency. Thus this cut fulfills the requirement coming from measured b-jet fraction. For completeness, charm misidentification efficiency is 4-6% in this tagged sample.

Efficiencies in sample tagged by $\sigma_{vtx} < 0.02$ cm and $SL_{xy} > 7$ are in the middle of efficiencies obtained in the two described samples. This sample is as well chosen because of small statistics in the tightest cut.

As it can be observed in Fig. 6.6, that shows distributions of secondary vertex mass without any scaling after applying cuts compared to the distribution with no cuts applied, the number of events in tagged sample is rapidly falling with the tightness of the cut. If there are no selection criteria applied on secondary vertices, so just jets with at least one reconstructed secondary vertex are considered, the overall number of jets with $20 < p_{\mathrm{T}} < 50$ GeV/c is 127 595. After applying described selection criteria in this transverse momentum region statistics are, from the loosest to the tightest cut, 4 728, 1 891 and 1 264. So only 3.7% of jets with secondary vertex pass the selection criteria for the loosest cut, for the tightest cut it is 1% of jets. Therefore, when cuts are applied, we should consider not only achievable efficiencies, but also statistics in tagged samples.

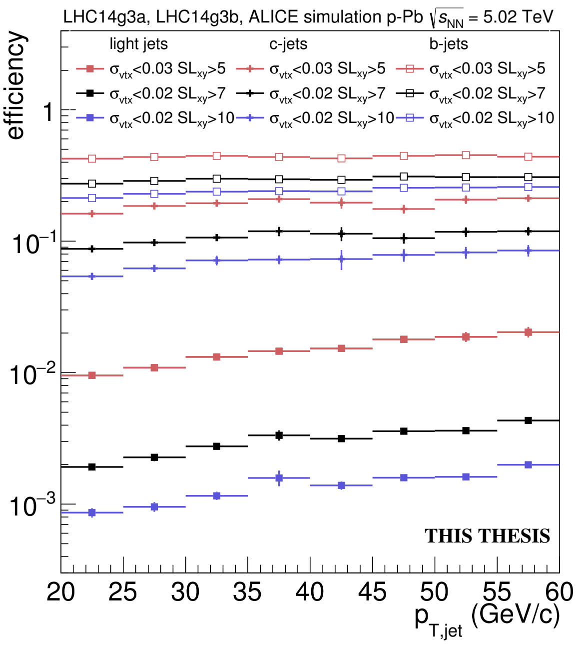

Figure 6.5: The jet transverse momentum $p_{\mathrm{T,jet}}$ dependence of the b-tagging efficiency and mistagging rate of the secondary vertex algorithm for the various samples tagged by the signed flight distance significance SL_{xy} and the secondary vertex dispersion σ_{vtx} in p-Pb collisions at $\sqrt{s_{\mathrm{NN}}} = 5.02$ TeV. Efficiencies are extracted from simulated jet enhanced p-Pb production at $\sqrt{s_{\mathrm{NN}}} = 5.02$ TeV (LHC14g3b) in case of light jets and from simulated heavy-flavour enhanced p-Pb production at $\sqrt{s_{\mathrm{NN}}} = 5.02$ TeV (LHC14g3a) in case of charm and beauty jets. Simulated events are generated by PYTHIA+HIJING.

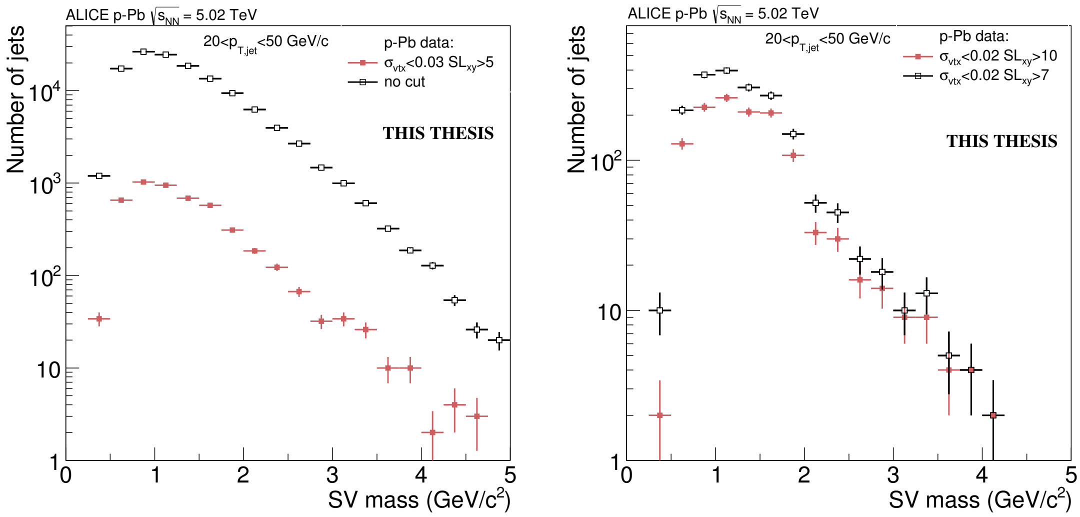

Figure 6.6: Distributions of the invariant mass of the furthest secondary vertex in the charged jet with transverse momentum $20 < p_{\mathrm{T,jet}} < 50$ GeV/c, in different samples tagged by the signed flight distance significance SL_{xy} and the secondary vertex dispersion σ_{vtx} in p-Pb collisions at $\sqrt{s_{\mathrm{NN}}} = 5.02$ TeV.

6.2.5 Template fitting

Once the efficiencies of tagged sample construction are known, tagged sample is fitted by templates from simulations to obtain b-jet purity in the sample. Templates are extracted from the MC simulations, in such a way that light-flavour templates are extracted from jet-enhanced simulation (LHC14g3b), charm template from charm-enhanced simulation (LHC14g3a) and beauty template from beauty-enhanced simulation (LHC14g3a). Templates are constructed by applying the same cuts as for the data and jets are labeled as described above. For fitting, RooFit[2] [57] is used. The results from fitting the sample tagged by $\sigma_{vtx} < 0.02$ cm and $SL_{xy} > 7$ for three considered p_{T}-bins are displayed in Fig. 6.7. The resulting purities for three flavours, as well as ξ^2/n.d.f are shown. The fact, that template fit converged with such precision gives a hint, that templates from MC have significantly different shapes and that this step is possible to be made. Results from template fits in all tagged samples and transverse momentum intervals, showed in this chapter, are in Appendix B.

In distributions of secondary vertex mass in charm jets, the ridge (or the large step) is observed around 1.5-2 GeV/c^2. This needs further study, but it is expected to come from D mesons decays (mass of D mesons is $\approx$ 1.8-2.1 GeV/c^2). This ridge is also observed in distributions from data, thus it is not caused by a mistake in MC simulations. On the other hand, the position and shape of this ridge could be helpful in fitting method for estimation of c-jet purity. In nearly all of the cases, ξ^2/n.d.f of the fit is smaller than 1 or around 1. Overall, the result of the fit describes the data quite well, mainly for secondary vertex mass smaller than 3 GeV/c^2. For large masses, mostly statistics are missing, resulting in large uncertainty.

In addition, tests of template fitting in simulation are done to study if the resulting purities are reasonable. First test is that tagged sample of inclusive jets from jet enhanced production (LHC14g3b) is fitted by the same templates as data. Resulting purity is com-

[2] The Toolkit for Data Modeling with ROOT (RooFit) is a package that facilitate in compact modeling of probability distributions. It is distributed with ROOT.

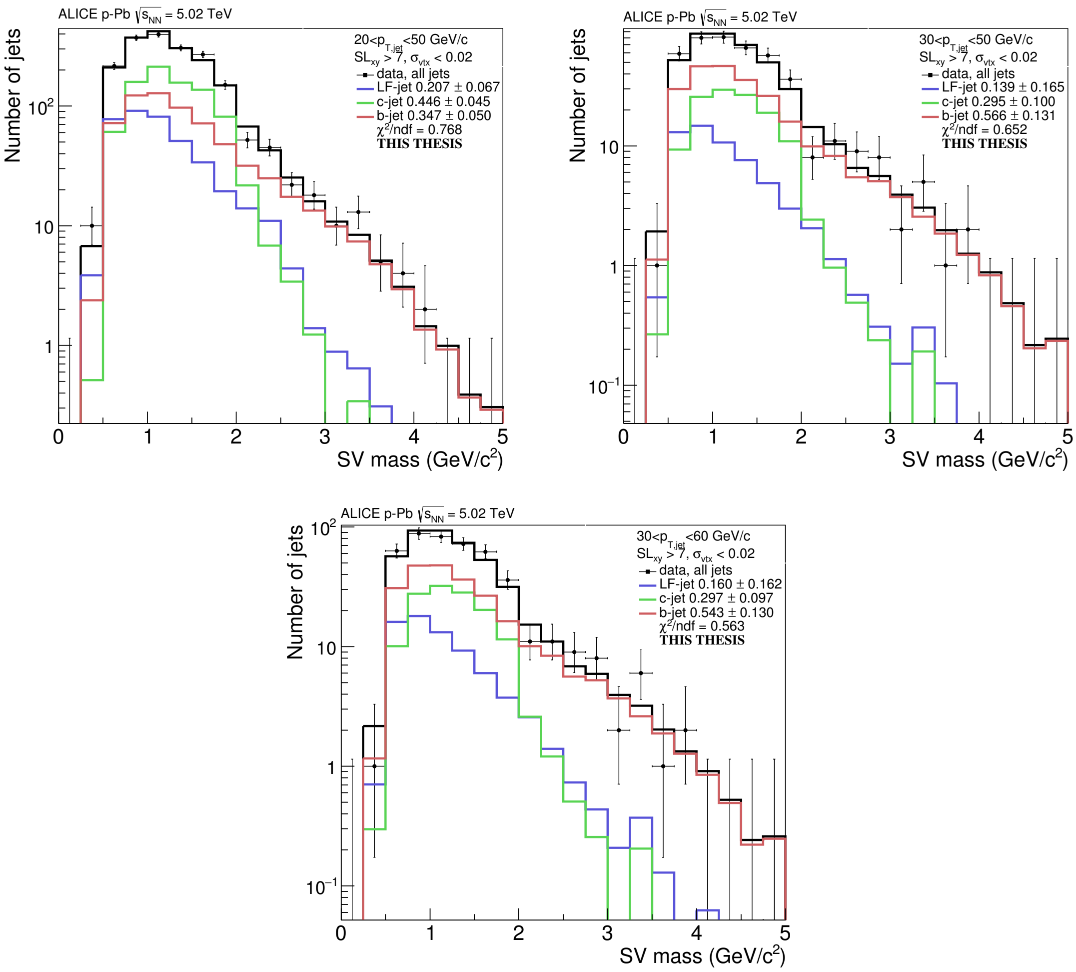

Figure 6.7: Template fit to the secondary vertex invariant mass distribution in p-Pb collisions at $\sqrt{s_{\mathrm{NN}}} = 5.02$ TeV, tagged by dispersion of secondary vertex $\sigma_{vtx} < 0.02$ cm and significance of signed flight distance of secondary vertex $SL_{xy} > 7$ for jets with transverse momentum $20 < p_{\mathrm{T}} < 50$ GeV/c, $30 < p_{\mathrm{T}} < 50$ GeV/c and $30 < p_{\mathrm{T}} < 60$ GeV/c. Filled black points are data, while the colored lines denote distributions of beauty, charm, and light jets in red, green and blue, respectively, extracted from the template fit to data (black line). Statistical uncertainties from data are shown as black vertical bars. Simulated events, used to extract MC templates, are generated by Pythia+Hijing.

pared to the true one, extracted from MC as the fraction of b-jets in the tagged sample. Results and the comparison is in Fig. 6.8. The uncertainty showed for the true one is statistical. For $20 < p_{\mathrm{T}} < 50$ GeV/c the fitted b-purity is within uncertainty the same as the true one. In other p_{T} bins, purity from fit is slightly higher than the true one. For sample tagged by $\sigma_{vtx} < 0.02$ cm and $SL_{xy} > 10$, in p_{T} bins $30 < p_{\mathrm{T}} < 50$ GeV/c and $30 < p_{\mathrm{T}} < 60$ GeV/c, b-jet purity is larger than the true one by ≈ 0.06, for other two samples in the same p_{T} bins it is overestimated by 0.02-0.04. In all cases, results are satisfying, thus template fitting method could be used in data and the results are certain.

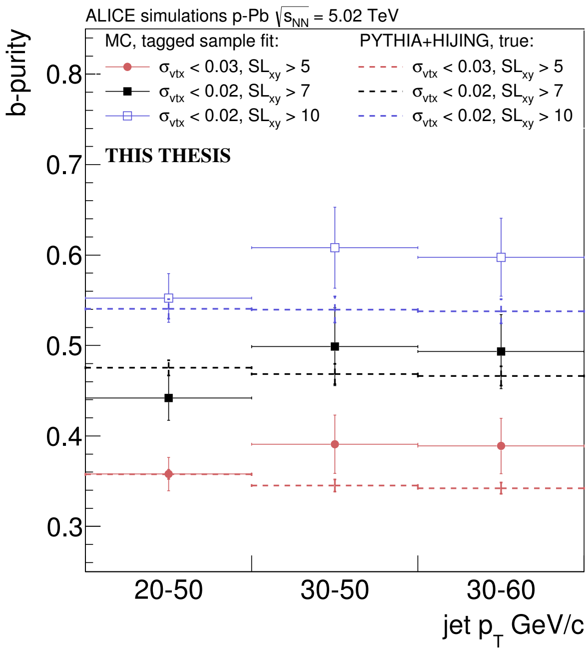

Figure 6.8: The b-jet purity extracted from template fits to the secondary vertex mass distributions (full line) in simulated p-Pb production at $\sqrt{s_{\mathrm{NN}}} = 5.02$ TeV (LHC14g3b) compared to the true purity in this simulation (dashed lines) for three samples tagged by different cuts on secondary vertex dispersion σ_{vtx} and significance of signed flight distance SL_{xy}. Templates are extracted from simulated jet enhanced p-Pb production at $\sqrt{s_{\mathrm{NN}}} = 5.02$ TeV (LHC14g3b, the same as the fitted one) in the case of light-jet template and from simulated heavy-flavour enhanced p-Pb production at $\sqrt{s_{\mathrm{NN}}} = 5.02$ TeV (LHC14g3a) in the case of charm and beauty jets. Simulated events are generated by Pythia+Hijing.

Template fitting method thus results in b-jet purity in three p_{T}-bins for three different selection criteria. This purity is shown in Fig. 6.9, also the true purity in the jet enhanced sample is shown. These two are not required be exactly the same, as Pythia does not describe well heavy-flavour production, but they are shown together for better orientation and interpretation of the result from data. For $20 < p_{\mathrm{T}} < 50$ GeV/c, mean values of b-jet purities in three samples are from 34.7% to 40.3%., giving a hint on correct functionality of the algorithm. In bins $30 < p_{\mathrm{T}} < 50$ GeV/c and $30 < p_{\mathrm{T}} < 60$ GeV/c, the intervals of resulting purities are larger, $\approx 14\%$. However, in these two bins, the ordering of the purity mean value is exactly opposite as expected. It can be observed, that the cut with the highest efficiency, expecting to have small b-jet purity, has the largest one.

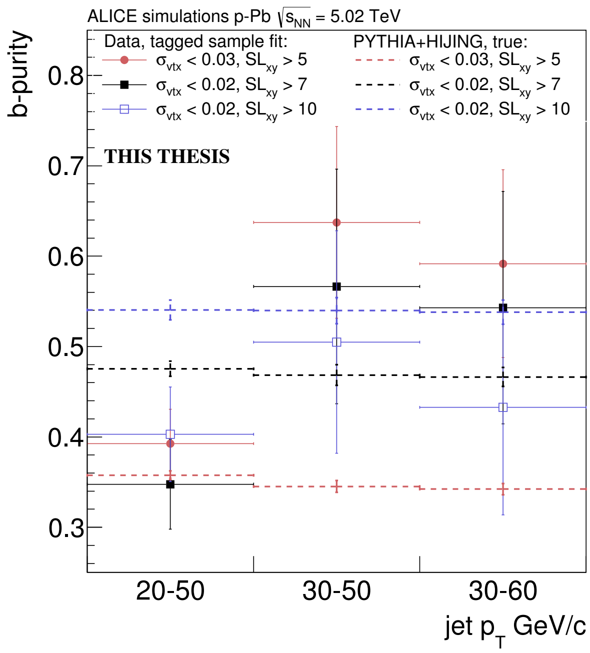

Figure 6.9: The b-jet purity from template fits to secondary vertex mass distribution in p-Pb data at $\sqrt{s_{\mathrm{NN}}} = 5.02$ TeV (full line) compared to the true purity in the jet enhanced p-Pb simulation (dashed lines) for three samples tagged by different cuts on secondary vertex dispersion σ_{vtx} and significance of signed flight distance SL_{xy}. Templates are extracted from simulated jet enhanced p-Pb production at $\sqrt{s_{\mathrm{NN}}} = 5.02$ TeV (LHC14g3b) in the case of light-jet template and from simulated heavy-flavour p-Pb enhanced production at $\sqrt{s_{\mathrm{NN}}} = 5.02$ TeV (LHC14g3a) in the case of charm and beauty jets. Simulated events, to extract templates, are generated by Pythia+Hijing.

6.2.6 Correction for detector effects and background fluctuations

The jet momentum distribution is distorted by the detector mainly due to tracking inefficiency and momentum resolution, thus corrections should be performed. For this, the ALICE detector simulation by GEANT is used. Reconstructed jets at particle level without detector effects and jets at the detector level after particle transport through the ALICE detector are matched and based on this the detector response matrix is built. The true jet momentum distribution is obtained via unfolding of the jet momentum distribution at the detector level with inverse response matrix. The unfolding of the momentum distribution at detector level with inverse response matrix leads to the true jet momentum distribution. In this work, the Singular Value Decomposition (SVD) [58] regularization method is used.

The correction for detector effects is tested with two detector response matrices: the detector response for b-jets and the one for inclusive jets. Figure 6.10 shows the ratio of two unfolded b-jets p_{T}-spectra. In both cases the unfolding procedure yields a similar result. This ensures that beauty and inclusive jets have similar detector response matrices and therefore the detectors response for inclusive jets can be used to unfold the tagged b-jet spectrum.

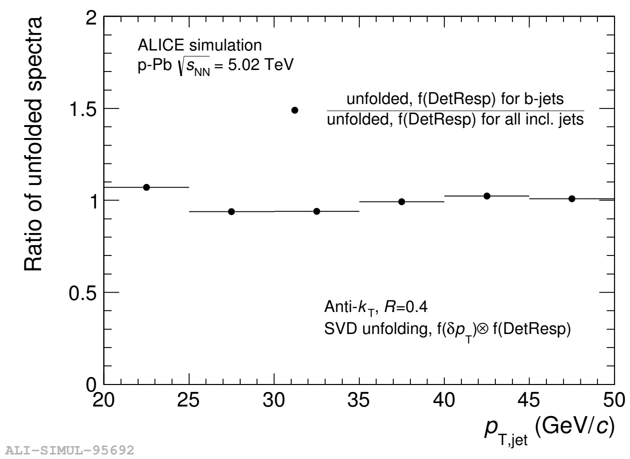

Figure 6.10: Comparison of Singular Value Decomposition (SVD) unfolding of b-jet spectrum with two matrices: detector matrix for inclusive jets and for b jets. Both matrices are combined with background fluctuation matrix from MC. The ratio of the two unfolded results is shown. Spectra constructed from simulated heavy-flavour enhanced p-Pb collisions at $\sqrt{s_{\mathrm{NN}}} = 5.02$ TeV by PYTHIA+HIJING, detector response matrix constructed from pp collisons at $\sqrt{s_{\mathrm{NN}}} = 5.02$ TeV with a Lorentz boost by PYTHIA.

As described in Sec. 6.2.2, non constant jet background is represented by background fluctuation matrix. The unfolding is done with a matrix which is a product of this matrix with detector response matrix. In measurements, the jet momentum correction for tagging performance and the unfolding have to be applied carefully. If the tagged spectrum is unfolded first, one has to be sure that the response matrix does not depend on the jet flavour. The tagging efficiency and purity then have to be estimated at particle level and to be free from background fluctuations. This can be done with the unfolding of efficiency and purity. This additional unfolding, on the other hands, implies large systematic error.

Order of unfolding and corrections on tagging efficiency and purity is not straightforward and it is studied in more details to estimate its systematic influence. The stability is tested in two scenarios:

- the measured tagged b-jet spectrum is first unfolded for detector response and background fluctuations, then corrected for the b-tagging efficiency as a function of $p_{\mathrm{T}}^{\mathrm{gen}}$ (at particle level).

- the measured tagged b-jet spectrum is first corrected for the b-tagging efficiency as a function of $p_{\mathrm{T}}^{\mathrm{det}}$ and then unfolded for detector response and background fluctuations.

Figure 6.11 displays comparison of the spectra obtained by the two scenarios. As it can be observed, they are in agreement with each other, suggesting that both scenarios can be applied in p-Pb collisions.

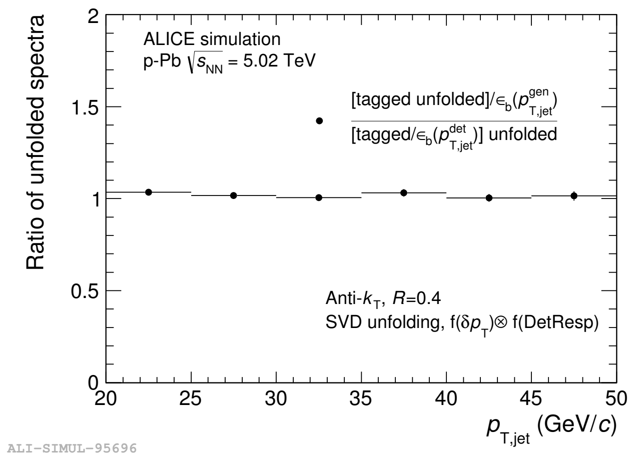

Figure 6.11: Comparison of two sequences of corrections: Singular Value Decomposition (SVD) unfolding and correction for tagging performance and vice versa. The ratio of the two corrected spectra is shown. Spectra constructed from simulated heavy-flavour enhanced p-Pb collisions at $\sqrt{s_{\mathrm{NN}}} = 5.02$ TeV by Pythia+Hijing, detector response matrix constructed from pp collisons at $\sqrt{s_{\mathrm{NN}}} = 5.02$ TeV with a Lorentz boost by Pythia.

6.3 Systematic uncertainties

The dominant group of systematical uncertainties is resulting from tagging of samples and it can be studied by variation of selection criteria (cuts on σ_{vtx} and SL_{xy}) that results in close efficiencies. Efficiencies used in this analysis are MC based. Their comparison with data-driven estimations of efficiencies lead to another correction of efficiency.

Another source of uncertainties is jet reconstruction. This uncertainty arises from jet energy resolution. In addition, another uncertainty comes from unfolding by SVD and is studied by varying SVD regularization and the prior spectrum.

Systematic uncertainty, coming from template fitting, should also be studied. This could be done in MC simulations by smearing templates, as well as fitted distributions. Smeared distributions are then fitted to extract b-jet purities. Differences in these purities result in systematic studies.

Other systematics, that should be considered are different p_{T} cuts on tracks used for secondary vertex reconstruction, and different shapes of b-jet and c-jet distributions in MC simulations and in data. These are not well reproduced by Pythia and could affect extracted mass templates.

Finally, although various systematic studies were shown, absolute value of systematic error was not yet estimated. This will be the subject of further studies. To give a feeling of its value, b-jet fraction systematic uncertainty for $55 < p_{\mathrm{T}} < 70$ GeV/c was determined to be at the level of 12% in Ref. [51].

6.4 Results

Finally, obtained b-jet purities p_b in the tagged sample (Fig. 6.9) are then used to calculate b-jet fraction f_b in data. Using accessible informations, it is defined as

$$f_b = \frac{p_b N_{\text{tagged jets}}}{\epsilon_b N_{\text{all jets}}}, \tag{6.3}$$

where $N_{\text{tagged jets}}$ is the number of all jets in the tagged sample, $N_{\text{all jets}}$ is the number of all jets in the selected p_{T}-bin and ϵ_b is the b-tagging efficiency in the selected p_{T}-bin (from Fig. 6.5). Calculated b-jet fractions in different p_{T}-bins for different tagging criteria are shown in Fig. 6.12. This is compared with the true b-jet fraction in jet-enhanced simulations. Results from simulations and data are not expected the same, since it is known, that Pythia does not reproduce heavy-flavour production well enough.

In the left panel of Fig. 6.12, b-jet fraction in overlaying p_{T}-bins is shown to check consistency of results obtained with different cuts. For $20 < p_{\mathrm{T}} < 50$ GeV/c, where b-jet purities (Fig. 6.9) from template fits are having small uncertainty and are consistent, also b-jet fraction is consistent within the cuts. Even for $\sigma_{vtx} < 0.02$ cm and $SL_{xy} > 10$, and $\sigma_{vtx} < 0.02$ cm and $SL_{xy} > 7$ the result is the same, $\approx (1.8 \pm 0.2)$%. In addition for $30 < p_{\mathrm{T}} < 50$ GeV/c and $30 < p_{\mathrm{T}} < 60$ GeV/c, these cuts resulted in b-jet fractions with mean values separated by 1%. These two tagging criteria results in b-jet fractions being consistent within studied overlapping p_{T} bins. For the loosest cut, $\sigma_{vtx} < 0.03$ cm and $SL_{xy} > 5$, the b-jet fraction is largely overestimated (6%) for $30 < p_{\mathrm{T}} < 50$ GeV/c and $30 < p_{\mathrm{T}} < 60$ GeV/c, although across momentum ranges it differs by only ≈ 0.5%.

To summarize, tighter cuts $\sigma_{vtx} < 0.02$ cm and $SL_{xy} > 10$, and $\sigma_{vtx} < 0.02$ cm and $SL_{xy} > 7$, with good light jets suppression seem to be quite consistent, but the loosest cuts overestimate the fraction and they do not provide such stability as tighter cuts.

Results on b-jet fraction for $20 < p_{\mathrm{T}} < 60$ GeV/c separated in three momentum ranges are displayed in Fig 6.12 (Right). Taking into account the fact, that systematic errors are have not yet been estimated, we interpret these results conservatively. Obtained value of the b-jet fraction is $\approx$ 1-6%. For $20 < p_{\mathrm{T}} < 40$ GeV/c, the same properties as in Fig 6.12 (Left) for fractions obtained by different cuts are observed. In momentum range $40 < p_{\mathrm{T}} < 60$ GeV/c, resulting b-jet fraction has a large uncertainty. For the tightest cut, statistics are limited in this region, thus the result is not reasonable. However, $\sigma_{vtx} < 0.02$ cm and $SL_{xy} > 7$, and $\sigma_{vtx} < 0.03$ cm and $SL_{xy} > 5$ results in mean value of b-jet fraction ≈ 3.5%. Comparing this result with the b-jet fraction at CMS for $50 < p_{\mathrm{T}} < 70$ GeV/c, displayed in Fig. 5.8, that have value of 4.2 ± 0.5% for $55 < p_{\mathrm{T}} < 70$ GeV/c, we can claim, that results are consistent. However, for $40 < p_{\mathrm{T}} < 60$ GeV/c our result in b-jet fraction is interpreted as 1-6%.

In summary, template fitting method shows stability for those cuts, that result in sufficient suppression of light contamination in tagged samples, although the statistics in such samples are very limited. The fact, that the method converged for all selected selection criteria, shows that b-tagging by secondary vertices is possible at ALICE experiment. To make our results more precise, rejection of VO topology tracks, that could help to enhance

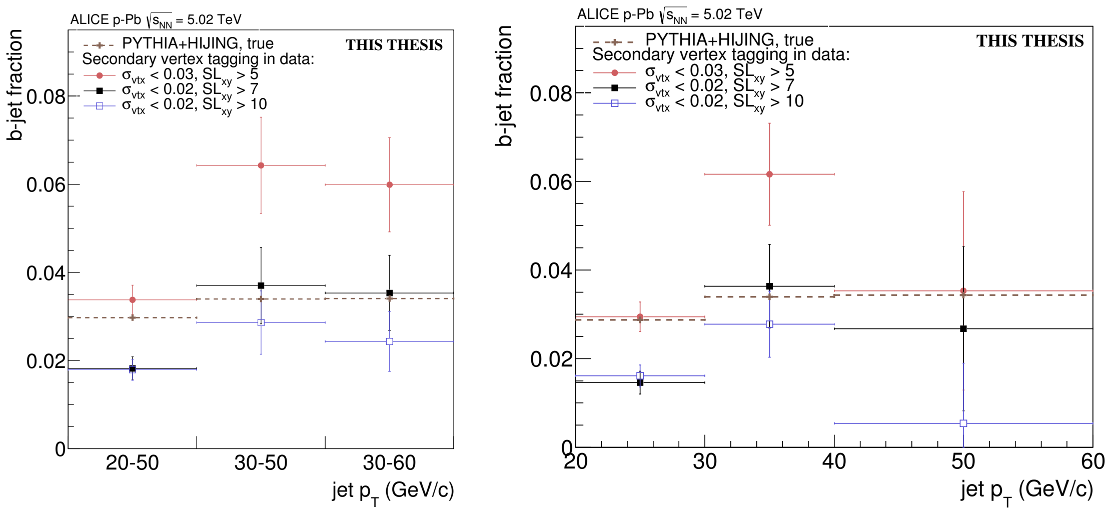

Figure 6.12: The b-jet fraction extracted from template fits in p-Pb data at $\sqrt{s_{\mathrm{NN}}} = 5.02$ TeV (full line) for three p_{T}-bins and three samples tagged by different cuts on secondary vertex dispersion σ_{vtx} and significance of signed flight distance SL_{xy}. True purity in jet enhanced simulation of p-Pb collisions at $\sqrt{s_{\mathrm{NN}}} = 5.02$ TeV from PYTHIA+HIJING is also shown (dashed line).

b purity, is going to be studied. PYTHIA does not describes heavy-flavour production well, thus first tests, using POWHEG simulations are ongoing. In the framework of the ALICE collaboration, cross checks of results with group reconstructing b-jets using only displaced tracks (Track Counting algorithm) are developed.

6.5 Statement about the author contribution

Results presented in this chapter are the original work of the author of this thesis. Firstly, this included quality analysis of secondary vertex reconstruction both in data and in MC simulations. Then, properties of reconstructed secondary vertices were studied, in order to estimate performance of b-tagging by different selection criteria. Different tagged samples of secondary vertices were investigated. Based on this, 3 selection criteria, with different properties, were chosen. According tagged sample were fitted by templates from simulations, compared with MC results and used for b-jet fraction estimation. Every step was cross-checked in simulations for consistency.

Work was regularly discussed in Physics Analysis Group - Heavy-flavour Correlations and Jets, the subgroup of the heavy flavour physical working group of ALICE collaboration. Feedback from the group was used to improve the results of the analysis. During the work on this thesis, approved results on performance of the b-tagging via secondary vertices were presented on Winter School on Heavy Ion Physics in Budapest, Hungary; on 54$^{\mathrm{th}}$ International Winter Meeting on Nuclear Physics in Bormio, Italy (Appendix. C) and on 4$^{\mathrm{th}}$ International Conference on New Frontiers in Physics 2015 in Creta, Greece (Appendix. C). Figures, labeled as "THIS THESIS" were not approved by the ALICE collaboration and were created for the purposes of this thesis by the author. This is consistent with the ALICE publication policy.

Conclusions

Heavy-flavour measurements in nucleus and hadronic collisions provide information on the fragmentation of quark in the hot medium and on the in-medium energetic loss dependency on the quark mass. Heavy beauty quarks are created in the collision and traverse through the hot medium. Reconstruction of jets, coming from these quarks, could give access to their kinematics. Because of the large mass of beauty hadron, it decays in secondary vertex. The ALICE experiment has detection systems able to reconstruct these vertices. Once this is done, selection criteria are applied to their properties to construct tagged sample of jets. Large fraction of b jets is expected to be in such sample. The extract the number of b jets in it, fitting by template is done. These templates are extracted from simulated collisions.

This work presented study of such analysis in p-Pb collisions at $\sqrt{s_{\rm NN}} = 5.02$ TeV. This study have not yet been completed at the ALICE, unlike it was done at the CMS. The goal of the ALICE is to study smaller transverse momentum ranges than those at the CMS. At the ALICE, low momentum ranges are accessible thanks to its great low-momentum particle identification. However, statistics at the ALICE are not satisfying.

For simulation studies, jet and heavy-flavour enhanced simulated data, generated by PYTHIA+HIJING, were used. Jet labeling in simulations is realised by search of B hadron in a cone around the jet axis. Charged jets, reconstructed by anti-$k_{\rm T}$ with parameter $R = 0.4$ are considered in both, the data and the simulations. It has been proven, that jet momentum distributions in these data and simulations are consistent.

In this analysis, properties of secondary vertices used for tagged sample construction are dispersion of secondary vertex and secondary vertex signed flight distance significance. Working point of this analysis was chosen in such a way, that light contamination is suppressed by two orders of magnitude in the tagged sample. Three tagged samples were constructed, having different efficiencies and purities of b-jets. The loosest cut has large statistics and efficiency, but the contamination of charm and light jets is large. On the other hand, the tightest cuts have satisfying suppression of light and charm flavour, but statistics are low especially for high transverse momentum of jets.

The secondary vertex invariant mass in the three tagged samples is then fitted by templates from the simulations. These templates correspond to beauty, charm and light (gluons and u, d, s quarks) contributions. In the fitting, shape of the distribution is fixed, but its relative contribution to secondary vertex mass is allowed to float. Template fitting was tested in simulations and compared to the true purity. In summary, these tests showed that template fitting could be used. After applying template fits in data, resulting purities were consistent with expectations from previously published results by CMS.

Unfolding of b-jets is important to access jet momentum before distortion by detector effect. In our analysis, SVD unfolding method was used. Detector response matrices for b-jets and for inclusive jets were applied to unfold b-jet spectra. Two matrices give compatible resulting jet spectra.

Purities of b-jets in tagged samples, obtained via template fits, were used to calculate b-jet fraction in p-Pb collisions. This was done for three overlaying p_{T}-bins and for continuous transverse momentum range $20 < p_{\mathrm{T}} < 60$ GeV/c. Results for tagging selection criteria and p_{T}-bins with sufficient statistics results in b-jet fraction of 1-6%, that is consistent with results from the CMS experiments. Systematic errors has not been presented and will be further studied.

In the future, larger statistics are expected to be obtained in Run 2 and 3 of the LHC. The track impact parameter resolution at the ALICE is expected to improve by the factor of 3 (6) in longitudinal (transverse) direction due to upgrade of the ALICE tracking detectors. These could result in better light-flavour rejection in b tagging analysis.

Bibliography

[1] Particle Data Group Collaboration, K.A. Olive et al., *2014 Review of Particle Physics,* Chin. Phys. C, 38, 090001 (2014).

[2] ATLAS Collaboration, CMS Collaboration, G. Aad et al., *Combined Measurement of the Higgs Boson Mass in pp Collisions at* $\sqrt{s} = 7$ *and 8 TeV with the ATLAS and CMS Experiments*, Phys. Rev. Lett. 114, 191803 (2015).

[3] O. Buchmueller et al., *Collider Interplay for Supersymmetry, Higgs and Dark Matter*, Eur. Phys. J. C 75, 469, (2015).

[4] M. Gell-Mann, *A schematic model of baryons and mesons,* Phys. Lett. 8, 214 (1964).

[5] G. Zweig, *An* SU_3 *model for strong interaction symmetry and its breaking,* CERN-TH-401 (1964).

[6] LHCb collaboration, R. Aaij et al., *Observation of* $J/\psi p$ *resonances consistent with pentaquark states in* $\Lambda_b^0 \to J/\psi K^- p$ *decays,* Phys. Rev. Lett. 115, 072001 (2015).

[7] AEgIS Collaboration, S.Aghion et al., *Prospects for measuring the gravitational free-fall of antihydrogen with emulsion detectors*, JINST 8 P08013 (2013).

[8] Bejar Alonso et al., *HiLumi LHC Technical Design Report*, CERN-ACC-2015-0140 (2015).

[9] M. Benedikt, F. Zimmermann, *Status and Challenges of the Future Circular Collider Study*, CERN-ACC-2016-0005 (2016).

[10] M. Aicheler et al., *A Multi-TeV Linear Collider based on CLIC Technology: CLIC Conceptual Design Report*, CERN-2012-007 (2012).

[11] T. Behnke et al., *The International Linear Collider Technical Design Report - Volume 1: Executive Summary*, ILC-REPORT-2013-040 (2013).

[12] CEPC-SPPC Study Group, M. Ahmad et al., *CEPC-SPPC, Preliminary Conceptual Design Report, Volume I - Physics & Detector*, IHEP-EP-2015-01 (2015).

[13] ALICE Collaboration, K. Aadmodt. et al., *The ALICE experiment at the CERN LHC,* JINST 3 S08002 (2008).

[14] ATLAS Collaboration, G. Aad et al., *The ATLAS Experiment at the CERN Large Hadron Collider,* JINST 3 S08003 (2008).

[15] CMS Collaboration, S. Chatrchyan et al., *The CMS experiment at the CERN LHC,* JINST 3 S08004 (2008).

[16] LHCb Collaboration, A. A. Alves, Jr. et al., *The LHCb Detector at the LHC,* JINS 3 S08005 (2008).

[17] TOTEM Collaboration, G. Anelli et al., *The TOTEM Experiment at the CERN Large Hadron Collider,* JINST 3 S08007 (2008).

[18] LHCf Collaboration, O. Adriani et al., *The LHCf detector at the CERN Large Hadron Collider,* JINST 3 S08006 (2008).

[19] MoEDAL Collaboration, B. Acharya et al., *The Physics Programme Of The MoEDAL Experiment At The LHC,* Int. J. Mod. Phys. A29 1430050 (2014).

[20] C. Lefevre, *LHC: the guide*, CERN-Brochure-2009-003-Eng (2009).

[21] ALICE Collaboration, B. B. Abelev et al., *Performance of the ALICE Experiment at the CERN LHC,* Int. J. Mod. Phys. A 29 1430044 (2014).

[22] W. Yu, for the ALICE TPC Collaboration, *Particle identification of the ALICE TPC via dE/dx,* Nucl. Instrum. Meth. A706 55–58 (2013).

[23] G. Luparello for the ALICE Collaboration, *Performance of ALICE silicon tracker detector*, PoS (Vertex2013) 004 (2013).

[24] S. LaPointe for the ALICE collaboration, *Prospects for beauty-jet measurements with ALICE*, poster presentation, Quark Matter 2014, Darmstadt.

[25] ALICE EMCal Collaboration, U. Abeysekara et al., *ALICE EMCal Physics Performance Report*, arXiv:1008.0413 (2010).

[26] J. Allen et al., *ALICE DCal: An Addendum to the EMCal Technical Design Report,* CERN-LHCC-2010-011 (2010).

[27] R. Hagedorn, *Statistical thermodynamics of strong interactions at high-energies*, Nuovo Cim. Suppl. 3, 147 (1965).

[28] H. Bialkowska et al., *Strangeness enhancement and strangeness suppression in nuclear collisions at 200-GeV/N*, Z. Phys. C55 491-495 (1992).

[29] NA35 Collaboration, T. Alber et al., *Strange particle production in nuclear collisions at 200-GeV per nucleon*, Z. Phys. C64 195-207 (1994).

[30] U. Heinz, M. Jacob, *Evidence for a New State of Matter: An Assessment of the Results from the CERN Lead Beam Programme*, arXiv:nucl-th/0002042 (2000).

[31] BRAHMS Collaboration, I. Arsene et al., STAR Collaboration, J. Adams et al., PHOBOS Collaboration, B. B. Back et al., PHENIX Collaboration, K. Adcox et al., *First Three Years of Operation of RHIC*, Nucl. Phys. A 757 (2005).

[32] S. Sarkar et al., *Lecture notes in Physics 785,* The Physics of the Quark-Gluon Plasma, Springer (2010).

[33] STAR Collaboration, L. Kumar et al., *STAR Results from the RHIC Beam Energy Scan-I*, Nucl. Phys. A 904–905 256c–263c (2013).

[34] STAR Collaboration, J. Adams et al., *Experimental and Theoretical Challenges in the Search for the Quark Gluon Plasma: The STAR Collaboration's Critical Assessment of the Evidence from RHIC Collisions*, Nucl. Phys. A 757, 102 (2005).

[35] ALICE Collaboration, J. Adam et al., *Measurement of jet suppression in central Pb–Pb collisions at $\sqrt{s_{NN}} = 2.76$ TeV*, Phys. Lett. B 746 1 (2015).

[36] ATLAS collaboration, G. Aad et al., *Measurement of charged-particle spectra in Pb+Pb collisions at $\sqrt{s_{NN}} = 2.76$ TeV with the ATLAS detector at the LHC*, JHEP 09 050 (2015).

[37] ATLAS Collaboration, G. Aad et al., *Observation of a Centrality-Dependent Dijet Asymmetry in Lead-Lead Collisions at $\sqrt{s_{NN}} = 2.76$ TeV with the ATLAS Detector at the LHC*, Phys. Rev. Lett. 105, 252303 (2010).

[38] R. Snellings, *Elliptic Flow: A Brief Review*, New J. Phys. 13 055008 (2011).

[39] ALICE Collaboration, B. Abelev et al., *Elliptic flow of identified hadrons in Pb-Pb collisions at $\sqrt{s_{NN}} = 2.76$ TeV*, JHEP 06 190 (2015).

[40] T. Matsui, H. Satz, *J/psi suppression by quark-gluon plasma formation*, Phys. Lett. B 178, 416 (1986).

[41] T. Dahms, for the CMS collaboration, *Quarkonia and heavy-flavour production in CMS*, Nuclear Physics A 910–911 91 (2013).

[42] M C. de la Barca Sánchez for the CMS Collaboration, *Quarkonium Results in PbPb Collisions at CMS*, J. Phys.: Conf. Ser. 458 012011 (2013).

[43] Y.L. Dokshitzer, D.E. Kharzeev, *Heavy quark colorimetry of QCD matter*, Phys. Lett. 519, 199 (2001).

[44] M. Krelina, J. Nemchik, *Cronin effect at different energies: from RHIC to LHC*, EPJ Web of Conferences 66, 04016 (2014).

[45] A. Andronic et al., *Heavy-flavour and quarkonium production in the LHC era: from proton–proton to heavy-ion collisions*, Eur. Phys. J. C 76 no.3, 107 (2016).

[46] ALICE Collaboration, B. Abelev et al., *Production of Muons from Heavy Flavor Decays at Forward Rapidity in pp and Pb-Pb Collisions at $\sqrt{s_{NN}} = 2.76$ TeV*, Phys. Rev. Lett. 109, 112301 (2012).

[47] T. Renk, *Physics probed by the p_T dependence of the nuclear suppression factor*, Phys. Rev. C 88 014905 (2013).

[48] K. C. Zapp, F. Krauss, U. A. Wiedemann, *A perturbative framework for jet quenching*, JHEP 1303 080 (2013).

[49] CMS Collaboration, *Identification of b-quark jets with the CMS experiment*, JINST 8 P04013 (2013).

[50] CMS Collaboration, V. Khachatryan et al., *Transverse momentum spectra of inclusive b jets in pPb collisions at $\sqrt{s_{NN}} = 5.02$ TeV*, Phys. Lett B 754 59 (2016).

[51] CMS Collaboration, S. Chatrchyan et al., *Inclusive b-jet production in pp collisions at $\sqrt{s} = 7$ TeV*, JHEP 04 084 (2012).

[52] T. Sjostrand, S. Mrenna, P. Skands, *PYTHIA 6.4 Physics and Manual*, JHEP 0605 026 (2006).

[53] X.N. Wang, M. Gyulassy, *HIJING: A Monte Carlo model for multiple jet production in pp, pA, and AA collisions*, (1991).

[54] S. Agostinelli, et al., *Geant4 - a simulation toolkit*, Nucl. Instrum. Meth. A506 250-303 (2003).

[55] M. Cacciari, et al., *FastJet user manual*, Eur. Phys. J. C 72 1896 (2012).

[56] ALICE Collaboration, J. Adam et al., *Measurement of charged jet production cross sections and nuclear modification in p–Pb collisions at* $\sqrt{s_{NN}} = 5.02$ *TeV*, Phys. Lett. B 749 68 (2015).

[57] W. Verkerke, D. Kirkby, *The RooFit toolkit for data modeling*, arXiv:physics/0306116v1 (2003).

[58] A. Hocker, V. Kartvelishvili, *SVD Approach to Data Unfolding*, Nucl. Instrum. Meth. A372, 469, (1996).

[59] L. Hsu, J. P. Hsu, *The physical basis of natural units and truly fundamental constants,* Eur. Phys. J. Plus 127:11 (2012).

Appendix A

Natural units

In the field of elementary nuclear and particle physics, natural units are used. This system is based on universal physical constants, such as speed of light c, elementary charge e, reduced Planck constant $\hbar$ and Boltzmann constant k_B. In this system, these constant are fixed: $\hbar = c = k_B = 1$. All physical quantities are expressed in terms of energy E. Quantities, with appropriate natural units and with conversion to SI units system are in Table A.1. Usually, constants $c, \hbar$ and k_B are not written in units.

Quantity	**Natural units**	**Conversion**	
energy	E	1 eV	$= 1.602\ 177 \cdot 10^{-19}$ J
momentum	E	1 eV/c	$= 5.344\ 286 \cdot 10^{-28}$ kg·m/s
mass	E	1 eV/c^2	$= 1.782\ 662 \cdot 10^{-36}$ kg
temperature	E	1 eV/k_B	$= 11\ 604.522\ 1(67)$ K
time	$1/E$	1 $\hbar$/eV	$= 6.582\ 119 \cdot 10^{-16}$ s
length	$1/E$	1 $\hbar c$/eV	$= 1.973\ 27 \cdot 10^{-7}$ m
velocity	none	1	$= c = 2.997\ 924 \cdot 10^{8}$ m/s

Table A.1: Natural units of different quantities and their conversion to SI units. Data taken from Ref. [59].

Appendix B

Template fits of secondary vertex mass distributions

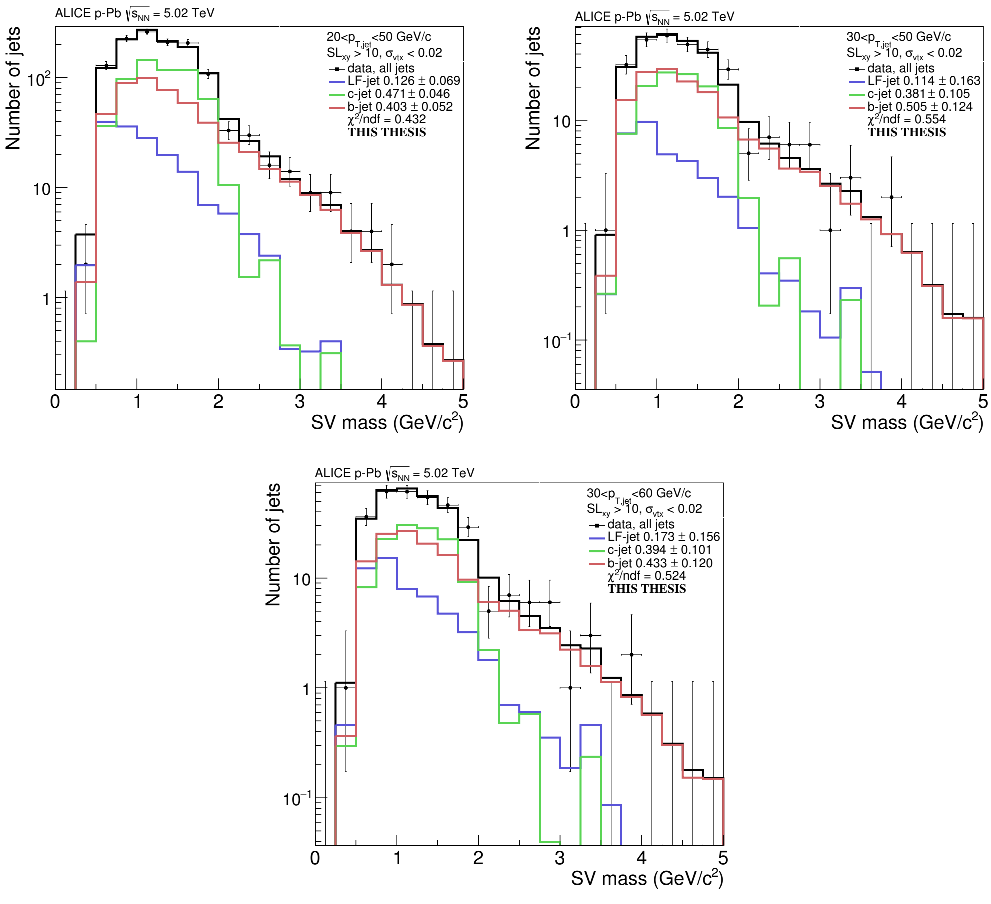

Figure B.1: Template fit to the secondary vertex invariant mass distribution in p-Pb collisions at $\sqrt{s_{\mathrm{NN}}} = 5.02$ TeV, tagged by dispersion of secondary vertex $\sigma_{vtx} < 0.02$ cm and significance of signed flight distance of secondary vertex $SL_{xy} > 10$ for jets with transverse momentum $20 < p_{\mathrm{T}} < 50$ GeV/c, $30 < p_{\mathrm{T}} < 50$ GeV/c and $30 < p_{\mathrm{T}} < 60$ GeV/c. Filled black points are data, while the colored lines denote distributions of beauty, charm, and light jets in red, green and blue, respectively, extracted from the template fit to data (black line). Statistical uncertainties from data are shown as black vertical bars. Simulated events, used to extract MC templates, are generated by Pythia+Hijing.

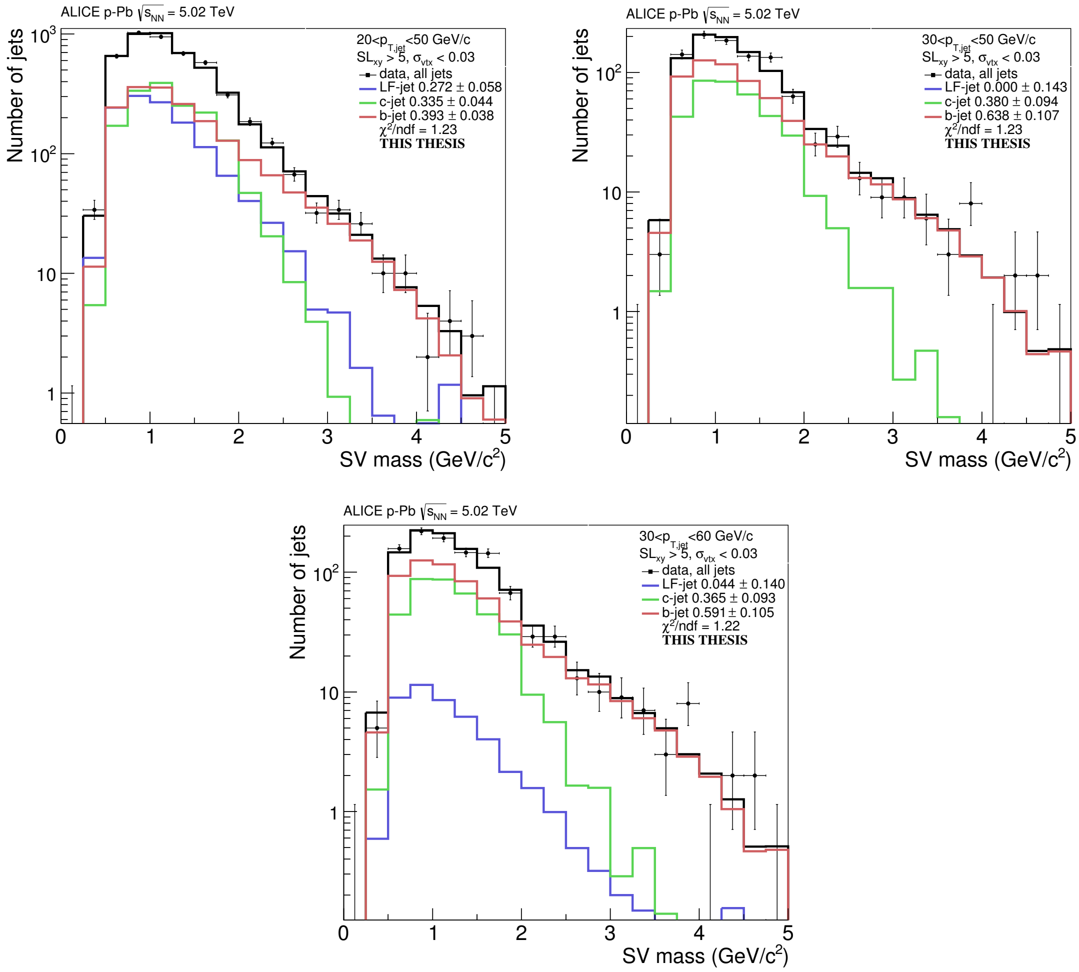

Figure B.2: Template fit to the secondary vertex invariant mass distribution in p-Pb collisions at $\sqrt{s_{\mathrm{NN}}} = 5.02$ TeV, tagged by dispersion of secondary vertex $\sigma_{vtx} < 0.03$ cm and significance of signed flight distance of secondary vertex $SL_{xy} > 5$ for jets with transverse momentum $20 < p_{\mathrm{T}} < 50$ GeV/c, $30 < p_{\mathrm{T}} < 50$ GeV/c and $30 < p_{\mathrm{T}} < 60$ GeV/c. Filled black points are data, while the colored lines denote distributions of beauty, charm, and light jets in red, green and blue, respectively, extracted from the template fit to data (black line). Statistical uncertainties from data are shown as black vertical bars. Simulated events, used to extract MC templates, are generated by Pythia+Hijing.

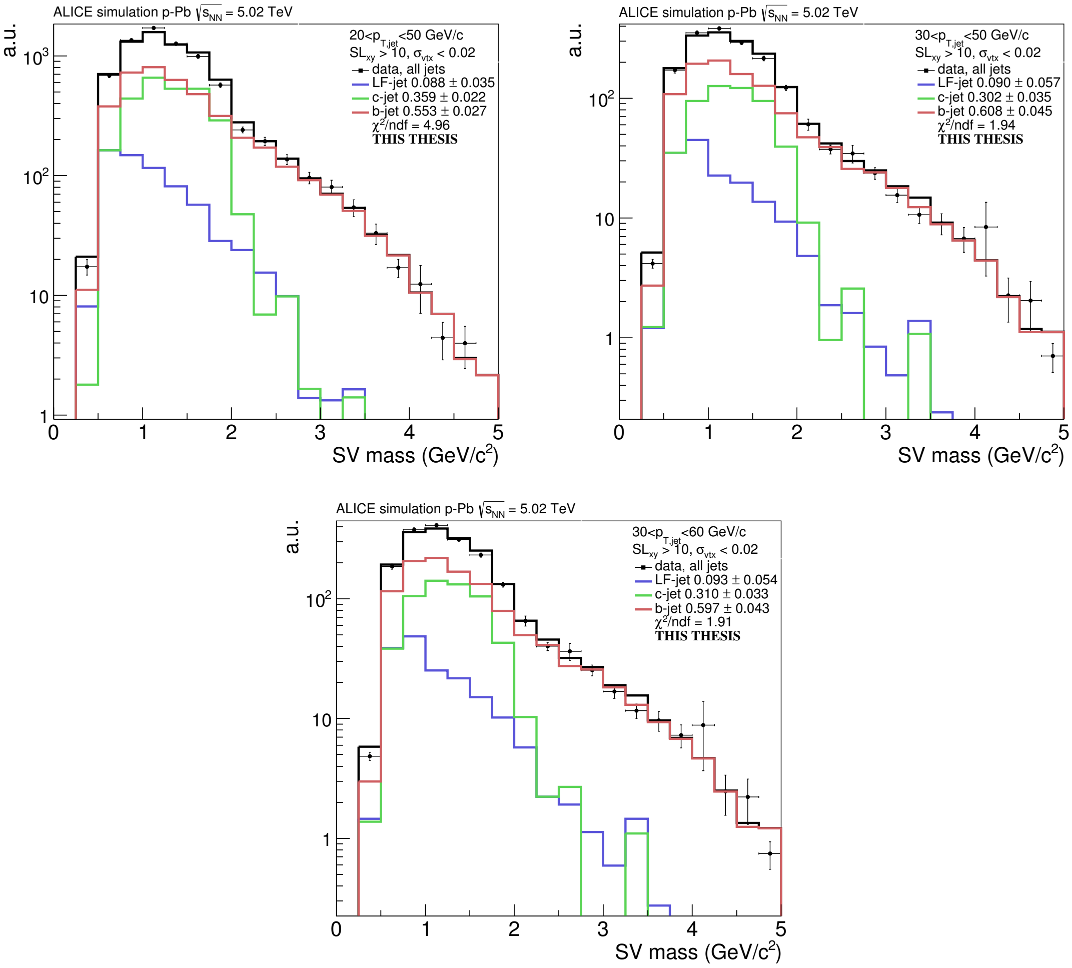

Figure B.3: Template fit to the secondary vertex invariant mass distribution in MC simulated p-Pb collisions at $\sqrt{s_{\mathrm{NN}}} = 5.02$ TeV, tagged by dispersion of secondary vertex $\sigma_{vtx} < 0.02$ cm and significance of signed flight distance of secondary vertex $SL_{xy} > 10$ for jets with transverse momentum $20 < p_{\mathrm{T}} < 50$ GeV/c, $30 < p_{\mathrm{T}} < 50$ GeV/c and $30 < p_{\mathrm{T}} < 60$ GeV/c. Filled black points are data, while the colored lines denote distributions of beauty, charm, and light jets in red, green and blue, respectively, extracted from the template fit to data (black line). Statistical uncertainties from data are shown as black vertical bars. Simulated events are generated by PYTHIA+HIJING.

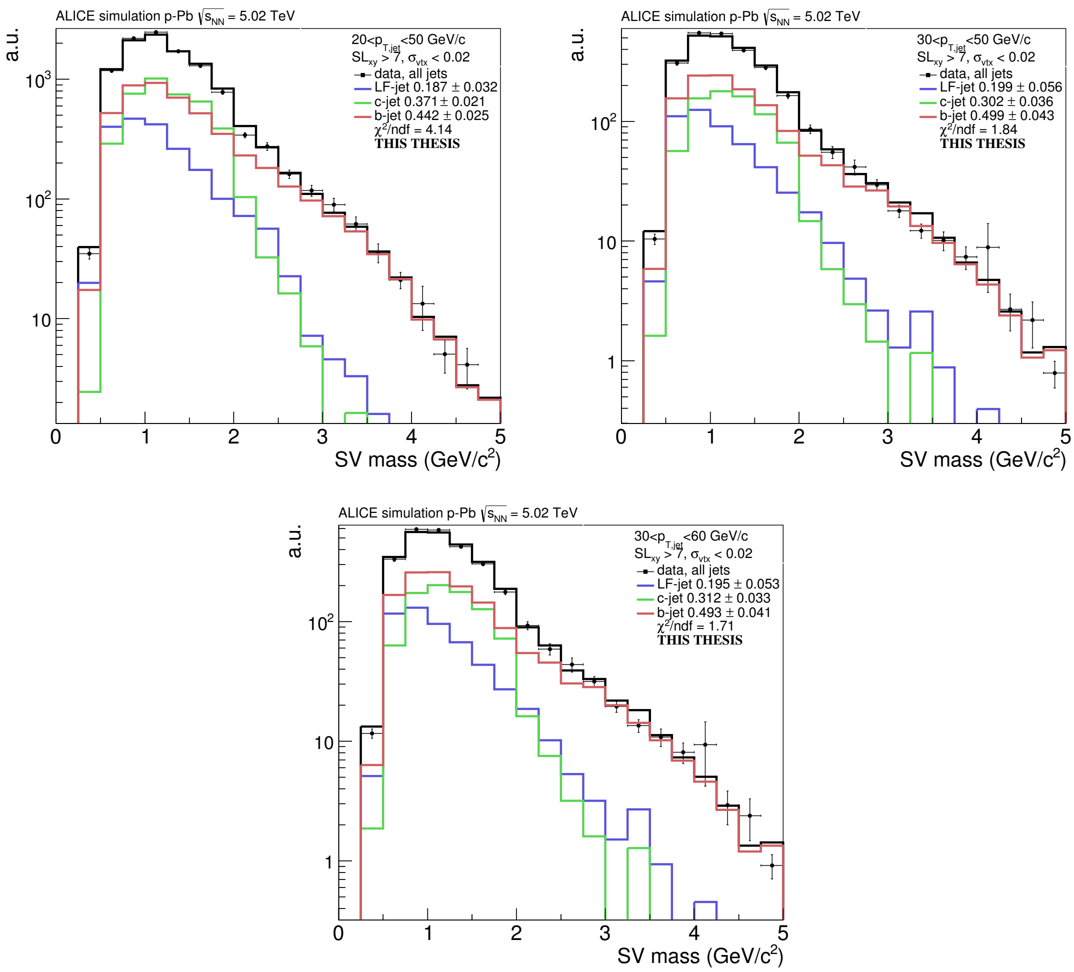

Figure B.4: Template fit to the secondary vertex invariant mass distribution in MC simulated p-Pb collisions at $\sqrt{s_{\rm NN}} = 5.02$ TeV, tagged by dispersion of secondary vertex $\sigma_{vtx} < 0.02$ cm and significance of signed flight distance of secondary vertex $SL_{xy} > 7$ for jets with transverse momentum $20 < p_{\rm T} < 50$ GeV/c, $30 < p_{\rm T} < 50$ GeV/c and $30 < p_{\rm T} < 60$ GeV/c. Filled black points are data, while the colored lines denote distributions of beauty, charm, and light jets in red, green and blue, respectively, extracted from the template fit to data (black line). Statistical uncertainties from data are shown as black vertical bars. Simulated events are generated by Pythia+Hijing.

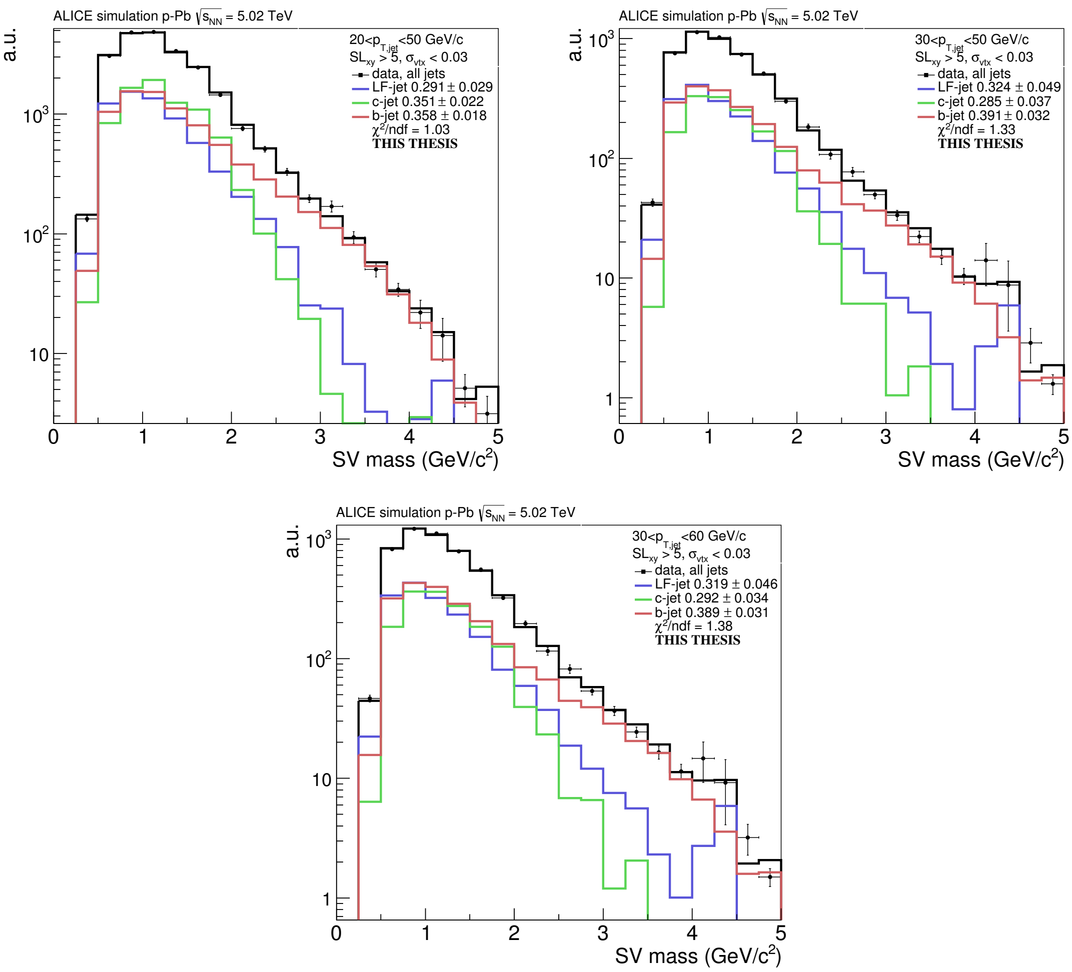

Figure B.5: Template fit to the secondary vertex invariant mass distribution in MC simulated p-Pb collisions at $\sqrt{s_{\mathrm{NN}}} = 5.02$ TeV, tagged by dispersion of secondary vertex $\sigma_{vtx} < 0.03$ cm and significance of signed flight distance of secondary vertex $SL_{xy} > 5$ for jets with transverse momentum $20 < p_{\mathrm{T}} < 50$ GeV/c, $30 < p_{\mathrm{T}} < 50$ GeV/c and $30 < p_{\mathrm{T}} < 60$ GeV/c. Filled black points are data, while the colored lines denote distributions of beauty, charm, and light jets in red, green and blue, respectively, extracted from the template fit to data (black line). Statistical uncertainties from data are shown as black vertical bars. Simulated events are generated by Pythia+Hijing.

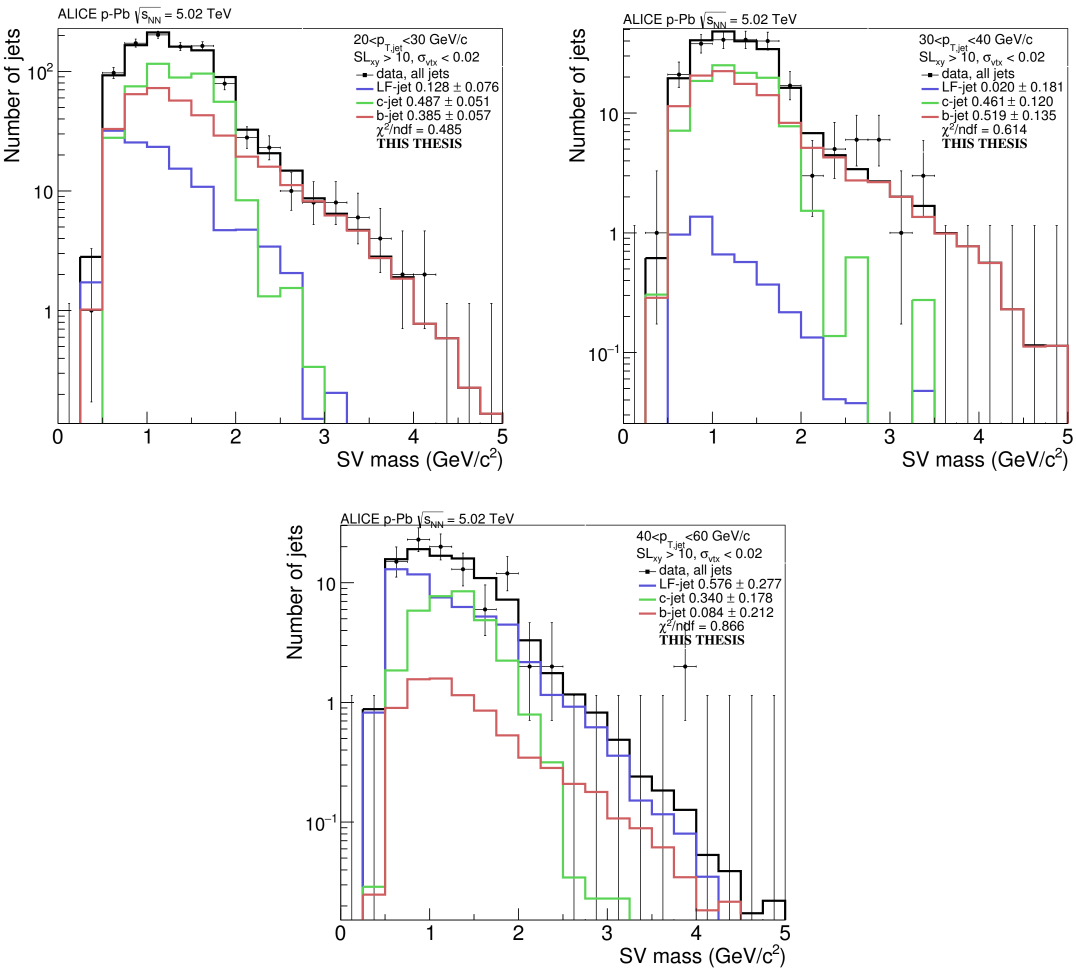

Figure B.6: Template fit to the secondary vertex invariant mass distribution in p-Pb collisions at $\sqrt{s_{\mathrm{NN}}} = 5.02$ TeV, tagged by dispersion of secondary vertex $\sigma_{vtx} < 0.02$ cm and significance of signed flight distance of secondary vertex $SL_{xy} > 10$ for jets with transverse momentum $20 < p_{\mathrm{T}} < 30$ GeV/c, $30 < p_{\mathrm{T}} < 40$ GeV/c and $40 < p_{\mathrm{T}} < 60$ GeV/c. Filled black points are data, while the colored lines denote distributions of beauty, charm, and light jets in red, green and blue, respectively, extracted from the template fit to data (black line). Statistical uncertainties from data are shown as black vertical bars. Simulated events, used to extract MC templates, are generated by Pythia+Hijing.

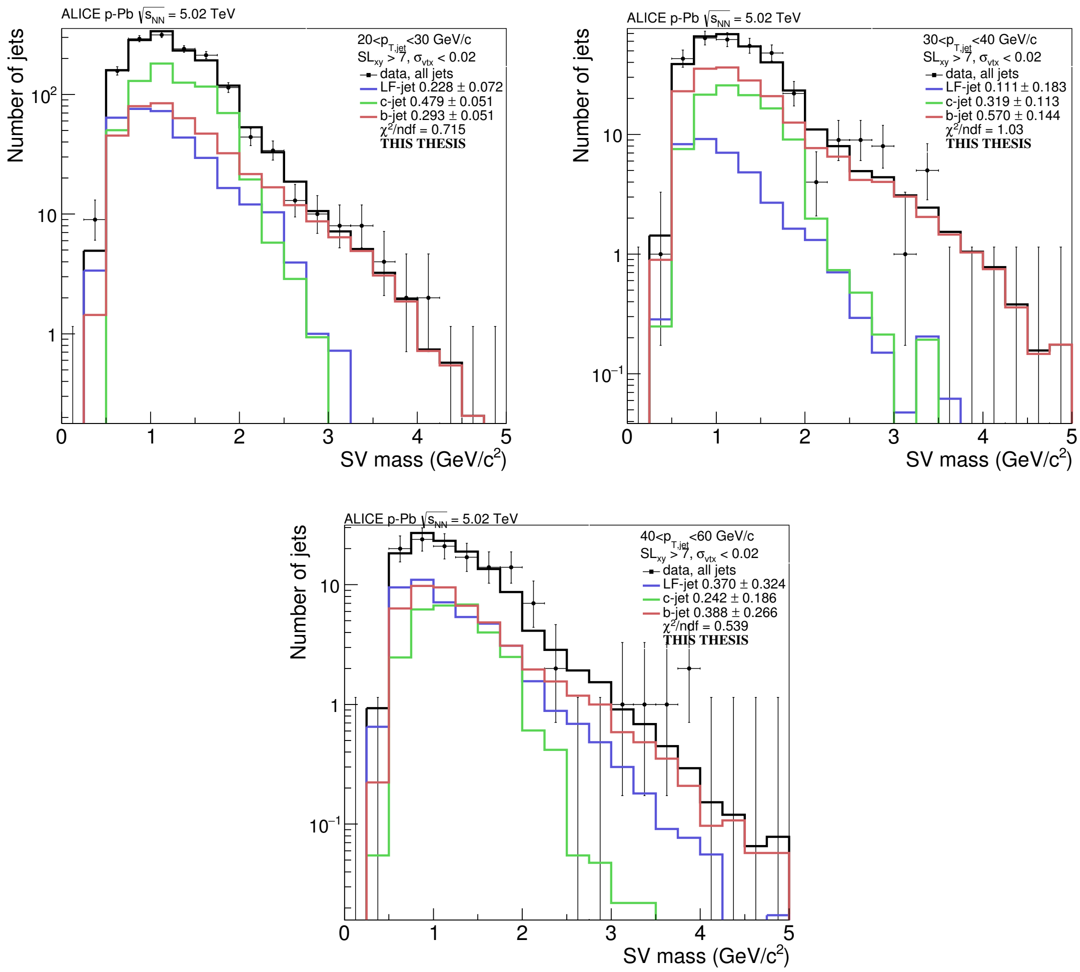

Figure B.7: Template fit to the secondary vertex invariant mass distribution in p-Pb collisions at $\sqrt{s_{\mathrm{NN}}} = 5.02$ TeV, tagged by dispersion of secondary vertex $\sigma_{vtx} < 0.02$ cm and significance of signed flight distance of secondary vertex $SL_{xy} > 7$ for jets with transverse momentum $20 < p_{\mathrm{T}} < 30$ GeV/c, $30 < p_{\mathrm{T}} < 40$ GeV/c and $40 < p_{\mathrm{T}} < 60$ GeV/c. Filled black points are data, while the colored lines denote distributions of beauty, charm, and light jets in red, green and blue, respectively, extracted from the template fit to data (black line). Statistical uncertainties from data are shown as black vertical bars. Simulated events, used to extract MC templates, are generated by Pythia+Hijing.

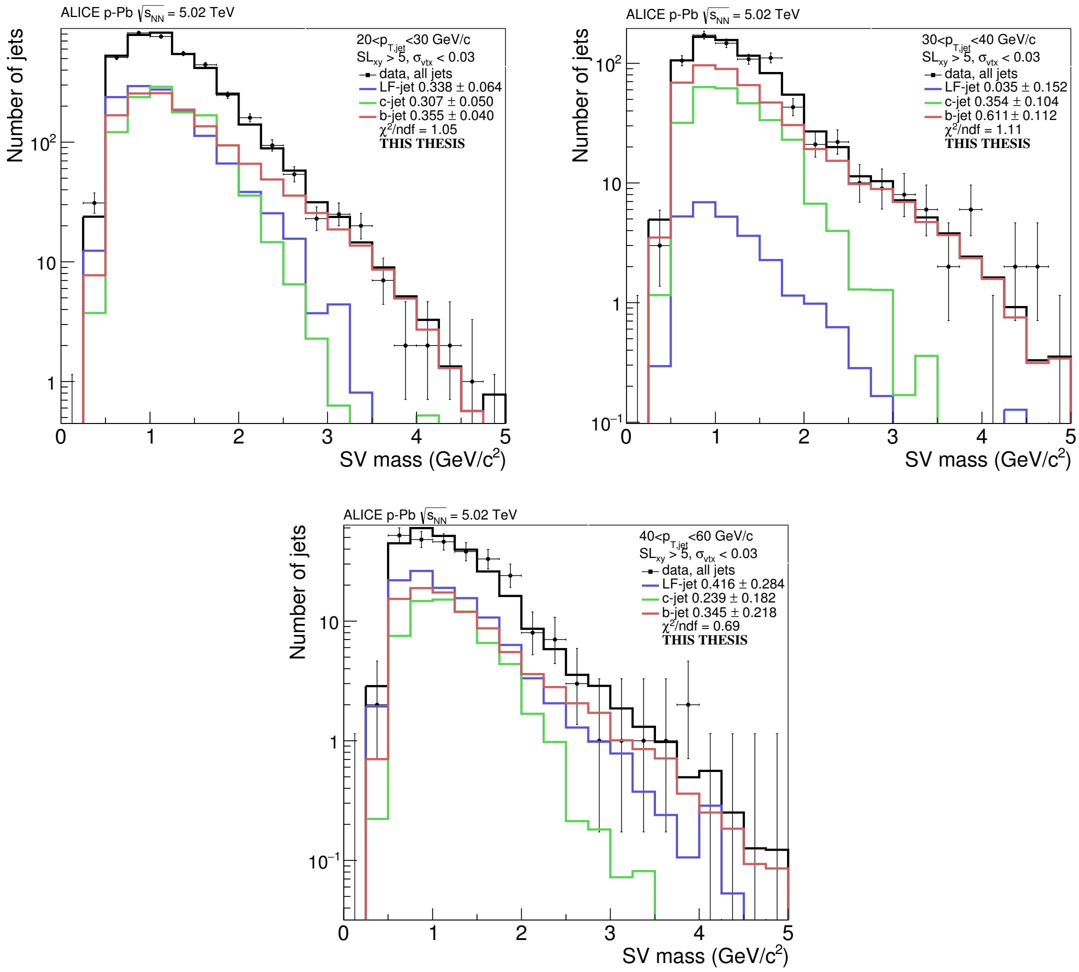

Figure B.8: Template fit to the secondary vertex invariant mass distribution in p-Pb collisions at $\sqrt{s_{\rm NN}} = 5.02$ TeV, tagged by dispersion of secondary vertex $\sigma_{vtx} < 0.03$ cm and significance of signed flight distance of secondary vertex $SL_{xy} > 5$ for jets with transverse momentum $20 < p_{\rm T} < 30$ GeV/c, $30 < p_{\rm T} < 40$ GeV/c and $40 < p_{\rm T} < 60$ GeV/c. Filled black points are data, while the colored lines denote distributions of beauty, charm, and light jets in red, green and blue, respectively, extracted from the template fit to data (black line). Statistical uncertainties from data are shown as black vertical bars. Simulated events, used to extract MC templates, are generated by PYTHIA+HIJING.

Appendix C

List of public presentations and proceedings

Presentations:

- L. Kramárik on behalf of the ALICE collaboration, *Performance of the ALICE secondary vertex b-tagging algorithm*, poster presentation, 54$^{\text{th}}$ International Winter Meeting on Nuclear Physics, Bormio, Italy, 25-29 January 2016.
- G. Eyyubova, L. Kramárik on behalf of the ALICE collaboration, *Performance of the ALICE secondary vertex b-tagging algorithm*, poster presentation, 4$^{\text{th}}$ International Conference on New Frontiers in Physics 2015, Creta, Greece, 23-30 August 2015. Content of this poster was the same as in the attached poster from International Winter Meeting on Nuclear Physics in Bormio, Italy.
- L. Kramárik on behalf of the ALICE collaboration, *Performance of the ALICE secondary vertex b-tagging algorithm*, Winter School on Heavy Ion Physics, Budapest, Hungary, 7-11 December 2015.

Proceedings:

- L. Kramárik on behalf of the ALICE collaboration, *Performance of the ALICE secondary vertex b-tagging algorithm*, 54$^{\text{th}}$ International Winter Meeting on Nuclear Physics, Bormio, Italy, 2016, to be approved and submitted to Proceedings of Science.
- G. Eyyubova, L. Kramárik on behalf of the ALICE collaboration, *Performance of the ALICE secondary vertex b-tagging algorithm*, 4$^{\text{th}}$ International Conference on New Frontiers in Physics 2015, Creta, Greece, to be published in European Physical Journal Web of Conferences, arXiv:1605.00143, 2016.

Performance of the ALICE secondary vertex b-tagging algorithm

Lukáš Kramárik on behalf of the ALICE collaboration
Faculty of Nuclear Sciences and Physical Engineering
Czech Technical University in Prague

54th International Winter Meeting on Nuclear Physics
25-29 January 2016, Bormio, Italy

Motivation

- Measure b-quark production cross section via the measurements of beauty (b) jets.
- Jets vs. heavy-flavour hadrons: access to the kinematics of partons produced in hard scattering in the initial stage of heavy-ion collisions.
- Colour and mass dependence of parton energy loss in the Quark-Gluon Plasma (QGP).

Analysis steps

- Jet-finding: jet reconstruction with charged tracks.
- Jet b-tagging: exploit long lifetime and large mass of beauty hadrons.
- Corrections: correction of jet transverse momentum p_T (or jet energy) for background and detector response (unfolding), corrections for b-tagging efficiency and charm/light jet contamination.
- *The studies presented in this poster are based on Monte Carlo (MC) simulations.*

Secondary vertex (SV) tagging algorithm

Benefits from long lifetime ($c\tau$ ~ 500 μm) of beauty hadrons.

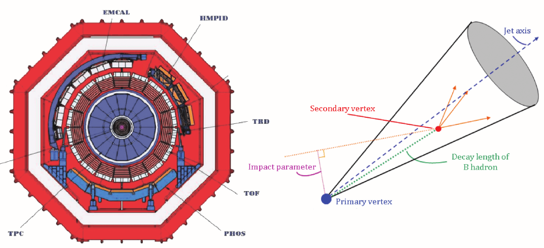

The Inner Tracking System (**ITS**) and Time Projection Chamber (**TPC**) are used for tracking and secondary vertex reconstruction. For all collision systems, ALICE measures the track impact parameter d_0 with a resolution better than 70 μm for p_T > 1 GeV/*c*.

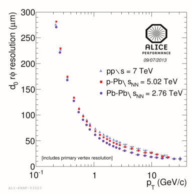

Track impact parameter resolution in the transverse plane vs p_T.

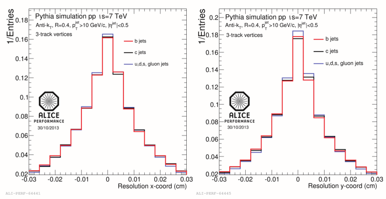

3-prong vertex resolution (in the *xy* plane).

- Jet reconstruction: FastJet Anti-k_T [1], R = 0.4
  $p_{T,\,track}$ > 0.15 GeV/*c*
- 3-prong SV are reconstructed using tracks in the jet, with $p_{T,\,prong}$ > 1 GeV/*c*.
- Discriminating variables: significance of signed SV distance of flight L_{xy}/σ_{Lxy} in the transverse plane and SV dispersion σ_{vtx}.

$$L_{xy} = L'_{xy} \times \mathrm{sign}(L_{xy} \cdot p_{T,jet})$$

$$\sigma_{vtx} = \sqrt{d_1^2 + d_2^2 + d_3^2}$$

$d_{1,2,3}$ are the distances of tracks from SV.

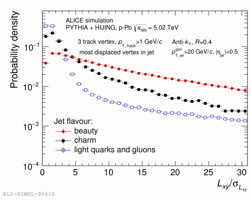

Signed flight distance significance of SV. Jets of different flavour defined in MC based on the presence of B- (D-) hadron.

[1] M. Cacciari and G. P. Salam, Phys. Lett. B 641 (2006) 57.

Secondary vertex algorithm performance in p-Pb collisions

$$\varepsilon_b(p_T) = \frac{dN_b^{tagged} / dp_T}{dN_b / dp_T}$$

Tagging efficiency: ratio of properly tagged jets and all jets of a given flavour.
It is obtained via MC studies.

The goal is to find the working point with high purity and reasonably high efficiency at the same time.

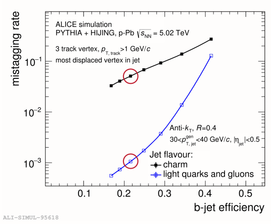

Tagging efficiency and mistagging rate with different cuts on L_{xy}/σ_{Lxy} of SV for 30 < $p^{gen}_{T,\,jet}$ < 40 GeV/*c*.

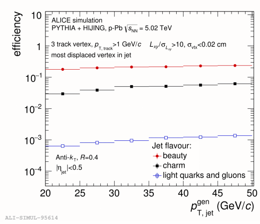

(Mis)Tagging efficiencies of SV algorithm for L_{xy}/σ_{Lxy} > 10 and σ_{vtx} < 0.02 cm.

Unfolding corrections

$$m(x') = \int dx A(x;x') t(x)$$

The measured spectrum *m(x')* is a convolution of a true spectrum *t(x)* and detector responce function *A(x;x')*. The true jet spectrum is found via unfolding procedure.

The Singular Value Decomposition (SVD) unfolding was used [2].

- The constant background density ρ_{CMS} (calculated with CMS method [3]) is subtracted from $p_{T,\,jet}$:

$$\rho_{CMS} = \mathrm{median}\left\{\frac{p_{T,i}}{A_i}\right\} \cdot C$$

$p_{T,i}$ are soft clusters, found by FastJet k_T, A_i is the jet area, *C* is the correction factor for the empty clusters.

- The background fluctuations δp_T are calculated with MC (HIJING) via random cone method:

$$\delta p_T = \sum p_{T,i} - \rho \cdot A_{cone}$$

The sum is over track $p_{T,i}$ in a cone.

- MC b-jet p_T spectrum is unfolded with the combined matrix: detector response and background fluctuations matrix. Same results are obtained when unfolding with detector response matrix of inclusive and b-jets
  → no strong influence of detector response in different fragmentation patterns of b- and inclusive jets.

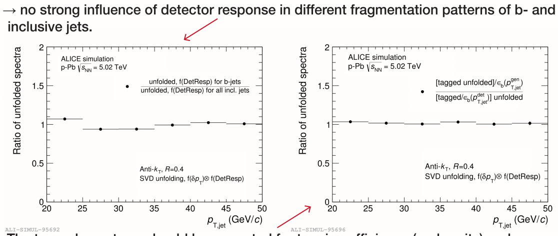

- The tagged spectrum should be corrected for tagging efficiency (and purity) and unfolded. It was verified with p-Pb simulations that the correction order does not give significant differences in the resulting spectrum.

[2] H. Hoecker, V.Kartverlishvili, Nucl. Instrum. Meth. A372 (1996) 469.
[3] CMS collaboration, JHEP 1208 (2012) 130.

Prospects with LHC/ALICE upgrades

- Upgrade of ITS (2019):
  improvement of the track impact parameter resolutions by a factor 3 (6) in the transverse (longitudinal) direction
  → better light-flavour rejection in b-tagging analysis.
  [CERN-LHCC-2012-012, CERN-LHCC-2012-013]
- ALICE read-out and LHC upgrades (2019):
  higher integrated luminosities: ~10 pb⁻¹ for pp collisions at $\sqrt{s}$ = 14 TeV and ~10 nb⁻¹ for Pb-Pb collisions at $\sqrt{s_{NN}}$ = 5.5 TeV required by the ALICE upgrade program
  → high precision heavy-flavour results, possibility to study on-line b-jet tagging.

Summary and ongoing studies

- The tagging cuts for SV algorithm are optimized for keeping beauty efficiencies as large as possible and at the same time charm and light-jet contamination small.
- Corrections for background and its fluctuations as well as for detector response are implemented. It was found that the b-jet spectrum can be corrected with a detector response matrix for all inclusive jets.
- The order of corrections (tagging efficiency vs unfolding) gives compatible results.

- MC and data-driven estimation of tagging purity is under study.
- Study of track selection for SV reconstruction in order to obtain higher purity is ongoing.

Acknowledgement
This work was supported by grant of Ministry of Education, Youth and Sports number LG13031.

PROCEEDINGS OF SCIENCE

Performance of the ALICE secondary vertex b-tagging algorithm

Lukáš Kramárik* **on behalf of the ALICE collaboration**
Department of Physics
Faculty of Nuclear Sciences and Physical Engineering
Czech Technical University in Prague
Břehová 7, 115 19 Prague 1, Czech Republic
E-mail: kramaluk@fjfi.cvut.cz

The hot and dense nuclear matter, that is produced in heavy-ion collisions, could be studied by jets originating from beauty quark. In-medium energy loss of these quarks provides information on several properties of the quark-gluon plasma. Reconstructed jets are powerful tool, since they offer access to kinematics of these energetic partons. Beauty hadrons are specific for their long lifetime, large mass and large-multiplicity decays. Due to long lifetime the beauty hadrons decay at secondary vertices. At the ALICE experiment, secondary vertex properties are used in one of the b tagging algorithms. The Study of Monte Carlo based performance of the b-tagging algorithm for charged jets in p-Pb collisions at $\sqrt{s_{\mathrm{NN}}} = 5.02$ TeV is discussed in this paper.

53rd International Winter Meeting on Nuclear Physics,
26-30 January 2015
Bormio, Italy

*Speaker.

1. Introduction

Heavy quarks (charm and beauty) are produced in hard scatterings in the initial stage of hadronic collisions. Later, they travel through the medium and loss their energy via gluon radiation and elastic collisions. Energy loss in the quark-gluon plasma (QGP), that is created in heavy-ion collisions, depends on the colour charge and mass of the traveling parton. In case of the gluon radiation, energy loss of light quarks and gluons is expected to be higher than for heavy quarks [1, 2], so transverse momentum spectra of heavy hadrons are less modified. However, for low transverse momentum, collisional energy loss may be important for heavy quarks in the QGP. Thus reconstructed jets, coming from heavy quarks fragmentation, are a powerful tool to study the properties of the QGP. For a quantitative studies of the QGP properties in Pb-Pb collisions, cold nuclear matter (CNM) effects, accessed by p-Pb collisions, are required to be taken into account.

The ALICE (A Large Ion Collider Experiment) detector [3] has great capability to reconstruct tracks, that are further used to reconstruct jets. Our goal is to tag jets coming from fragmentation of heavy b quark. Different tagging algorithms, based on properties of B decays, are studied at the ALICE. At the LHC (Large Hadron Collider) such study is done at the CMS (Compact Muon Solenoid) experiment [4]. At the ALICE, smaller transverse momentum of the jets is accessible. Here the Monte Carlo (MC) simulations based study of the performance of the b-jet tagging algorithm exploiting secondary vertex topologies for p-Pb collisions at $\sqrt{s_{\mathrm{NN}}} = 5.02$ TeV is presented.

2. Analysis details

Simulations used in this study for p-Pb collisions at $\sqrt{s_{\mathrm{NN}}} = 5.02$ TeV are represented by mix of event generators PYTHIA6 (Perugia 2011) [5], corresponding to hard physics, and HIJING [6] corresponding to p-Pb background. Collisions of protons at $\sqrt{s} = 5.02$ TeV, simulated by PYTHIA6, with tune Perugia 2011 with a Lorentz boost (to get the same rapidity shift as in p-Pb collisions), are used to study detector response for jets without underlying event. PYTHIA6, with tune Perugia 2011 [5], is employed for MC pp simulations. Response of the ALICE detector is simulated by GEANT3 [7].

Steps in this b-jet tagging analysis are as follows: track selection suitable for b-tagging, jet reconstruction from these tracks and underlying background subtraction under the jet area, tagging with a particular algorithm and, finally, corrections of the jet spectrum. Two main corrections of the raw tagged spectrum $\mathrm{d}N^{\mathrm{tag}}/\mathrm{d}p_{\mathrm{T}}$ have to be made. One of them is unfolding (for detector effects) and the other is for tagging efficiency and purity. Order of these operations is not straightforward and it is studied in more details to estimate its systematic influence. In case of p-Pb collisions, unfolding also includes a correction for fluctuations of the underlying background under the jet area.

Jet flavour in MC could be identified by different labeling methods. They use MC event history and they depend on parton shower implementation. In this analysis, MC jets are considered as b jets, if a B hadron is found in a cone $\Delta R < 0.7$ around jet axis. If no beauty hadron is present, but charm hadron was found in this cone, the jet is labeled as c-jet. All other jets are considered as light-flavour jets.

Extracted "true" number of b jets is used for algorithm efficiency and purity estimations. The efficiency of b-tagging is defined as the fraction of b jets in the sample after applying cuts (tagged sample), divided by the "true" number of b jets in data sample without any cuts. In addition, b tagging purity is fraction of b jets in the tagged sample and total number of jets in the sample.

The performance of the tagging algorithm is investigated via mistagging rate, which is the efficiency of mistakenly tagging as beauty a jet originating from a c-quark or a light-flavour parton. Mistagging rate studies are needed to extract sample with high purity of b jets. High purity allows to suppress the contamination of light-flavour and charm jets, which is important since the measured fraction of b jets to inclusive jets is at the level of 2-4% (as measured by CMS experiment), both in pp collisions at $\sqrt{s} = 7$ TeV [8] and in p-Pb collisions at $\sqrt{s_{\mathrm{NN}}} = 5.02$ TeV [4].

2.1 Track selection

For sufficient discriminating power of secondary vertex properties, beauty tagging use optimized track selection. Charged tracks, reconstructed with simulated responses of Inner Tracking System (ITS) and Time Projection chamber (TPC) in a pseudorapidity region $|\eta| < 0.9$ and transverse momentum $0.15 < p_{\mathrm{T}} < 100$ GeV/c, are required to have at least 70 (out of 159) points in TPC and at least one point in the Silicon Pixel Detector (SPD). Since some SPD regions are inefficient, the azimuthal distribution of these tracks is not completely uniform. This is why for jet reconstruction additional tracks without reconstructed track points in the SPD are considered.

2.2 Jet reconstruction and background estimation

For the estimation of the background density and fluctuations in jet reconstruction, a similar approach as it was applied by ALICE for charged jet measurements in p-Pb collisions [9] is used. Namely, the anti-k_{T} algorithm from the FastJet package [10] with resolution parameter of $R = 0.4$ is used to reconstruct charged jets. We use the CMS method [11], which is suited for more sparse environment in p-Pb collisions w.r.t Pb-Pb collisions, for the calculation of the background density ρ. The background fluctuations are calculated with a random cone approach as

$$\delta p_{\mathrm{T}} = \sum_i p_{\mathrm{T},i} - A_{cone} \cdot \rho,$$

where the sum is over the track p_{T} in a cone and A_{cone} is the cone area. For more details see [9]. Only jets with jet axis in the pseudorapidity interval $|\eta_{\mathrm{jet}}| < 0.5$ are considered, which ensures that the jet is fully located in the Time Projection Chamber acceptance. In this study the background fluctuations are measured with HIJING p-Pb events with particle transport through the ALICE detector. The background fluctuations under the jet area are found to be slightly smaller in the HIJING simulation than in the p-Pb data [9].

2.3 Correction for detector effects and background fluctuations

Jet momentum distribution corrections are performed using the detector simulation with environment GEANT. The detector response matrix is built by matching reconstructed jets at particle level without detector effects and jets at the detector level after particle transport through the ALICE detector. The unfolding of the momentum distribution at detector level with inverse response matrix leads to the true jet momentum distribution. In this study, the Singular Value Decomposition (SVD) [12] regularization method is used.

After subtracting the constant background in each event in order to correct the jet p_{T}, one has to keep in mind that the background is not necessary constant, but may differ for different jets in a given event. This is corrected statistically (not event by event) via an unfolding technique with a background fluctuation matrix $f(\delta p_{\mathrm{T}})$, where the background fluctuations δp_{T} are described in Sec. 2.2. The actual unfolding is done with a matrix which is a product of two matrices: detector response matrix and background fluctuation matrix.

The correction for detector effects is tested with two detector response matrices: the detector response for b-jets and the one for inclusive jets. Figure 1 shows the ratio of two unfolded b-jets p_{T}-spectra. In both cases the unfolding procedure yields similar result. This ensures that beauty and inclusive jets have similar detector response matrices and therefore the detectors response for inclusive jets can be used to unfold the tagged b-jet spectrum.

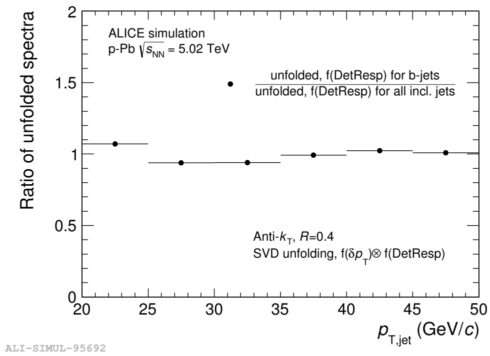

Figure 1: Comparison of SVD unfolding of b-jet spectrum with two matrices: detector matrix for inclusive jets and for b jets. Both matrices are combined with background fluctuation matrix from MC. The ratio of the two unfolded results is shown.

2.4 Secondary vertex tagging algorithm

This analysis describes performance of the secondary vertex b tagging algorithm. This algorithm exploits properties of beauty-hadron decays, that take place in secondary vertices. Firstly, all secondary vertices are reconstructed using tracks with properties mentioned above and with transverse momentum $p_{\mathrm{T,track}} > 1$ GeV/c. Secondary vertex is calculated as the point, for which the sum of the distances to the three such tracks is minimum. Then, for every jet, the secondary vertex, that is the furthermost from the primary vertex, is selected. Its properties are used to distinguish b jets from light flavour jets. Due to beauty properties, their decay vertex are expected to be displaced from the primary vertex of a collision.

Discriminating variables in our b-jet tagging analysis are secondary vertex dispersion and the significance of flight distance in a transverse plane. The dispersion of the tracks in the vertex is defined as $\sigma_{\mathrm{vtx}} = \sqrt{d_1^2 + d_2^2 + d_3^2}$, where $d_{1,2,3}$ are the distances of the three tracks from secondary vertex. It characterize quality of vertex reconstruction. The sign of the secondary vertex flight distance is defined w.r.t. the jet direction, so the signed length is $L = \left|\vec{L}'\right| \mathrm{sign}(\vec{L}' \cdot p_{jet})$, where $\vec{L}'$ is the SV position. The significance of flight distance in a transverse plane is then defined as $L_{xy}/\sigma_{L_{xy}}$. Cuts on these variables are applied on the selected (the furthermost) secondary vertex in jet.

The distribution of the signed flight distance significance for different flavours jets with transverse momentum $p_{\mathrm{T,jet}} > 20$ GeV/c is shown in Fig. 2. Its discriminating power is manifested by differences in shapes of its distribution for b jets and for light jets. Consequently, the larger the cut value of $L_{xy}/\sigma_{L_{xy}}$, the more light and charm jets are rejected compared to beauty jets.

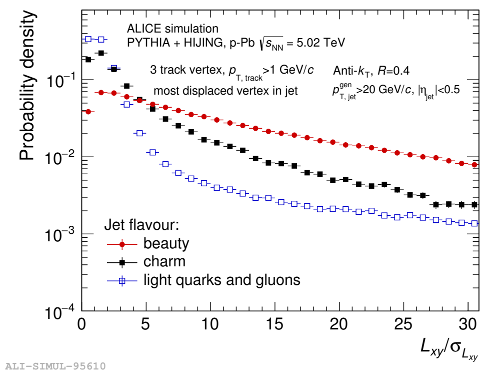

Figure 2: Probability distribution of the signed flight distance significance of the most displaced secondary vertex, found in charged jets with $p_{\mathrm{T}} > 20$ GeV/c in p-Pb simulations at $\sqrt{s_{\mathrm{NN}}} = 5.02$ TeV.

3. Performance of secondary vertex b-tagging algorithm

Different values of cuts on discriminating variables ($L_{xy}/\sigma_{L_{xy}}$ and σ_{vtx}) yield different algorithm performance. Our goal is to find the working point with sufficiently hight b-jet purity with the mistagging rate of light jets 100 times smaller than tagging efficiency to reduce background. This comes from the CMS measurements on the ratio of b jets to inclusive jets, in which the b-jet fraction was found to be at the level of 2-4% in pp collisions at $\sqrt{s} = 7$ TeV [8].

Figure 3, left, shows the performance plot (mistagging rate vs the b-tagging efficiency) in jet p_{T} range $30 < p_{\mathrm{T,jet}} < 40$ GeV/c for different operating points. These are obtained by varying the cuts on $L_{xy}/\sigma_{L_{xy}}$ (from 2 to 14), while the cut on $\sigma_{\mathrm{vtx}} < 0.02$ cm is fixed. In the considered region of the jet $p_{\mathrm{T,jet}}$, efficiencies are almost constant, however, in general they could fluctuate, especially in the wide ranges of $p_{\mathrm{T,jet}}$. Looser cuts result in larger statistics and higher tagging efficiency, but also higher mistagging rate, and therefore reduce purity of sample.

The tagging and mistagging efficiencies at particle level for the chosen operating point with $L_{xy}/\sigma_{L_{xy}} > 10$ and $\sigma_{\mathrm{vtx}} < 0.02$ cm are reported in Fig. 3, right. The b-tagging efficiency is around 20%, while the efficiency to tag light-flavour jets is two orders of magnitude lower and the efficiency to tag charm jet is about 3 to 5 times lower than the b-tagging efficiency.

The systematic influence of the order of unfolding and corrections on purity and efficiency is studied. The stability is tested in two scenarios:

- the measured tagged b-jet spectrum is first unfolded for detector response and background fluctuations, then corrected for the b-tagging efficiency as a function of $p_{\mathrm{T}}^{\mathrm{gen}}$ (at particle level).

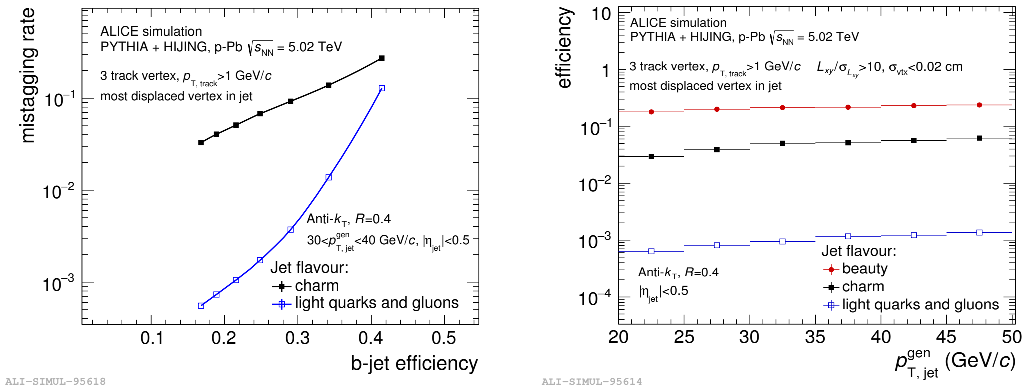

Figure 3: Left: Mistagging rate vs the b-tagging efficiency of SV tagging algorithm for different operating points for p_T range $30 < p_{T,jet} < 40$ GeV/c. Right: The $p^{gen}_{T,jet}$ dependence of the b-tagging efficiency and mistagging rate for $L_{xy}/\sigma_{L_{xy}} > 10$ and $\sigma_{vtx} < 0.02$ cm.

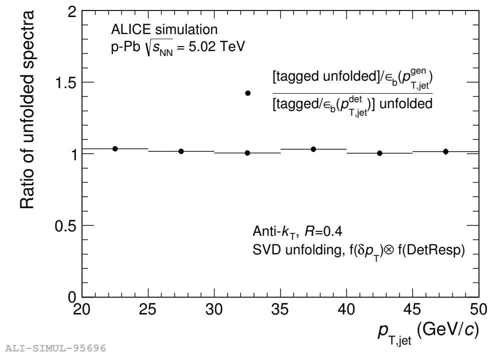

Figure 4: Comparison of two sequences of corrections: SVD unfolding and correction for tagging performance and vice versa. The ratio of the two corrected spectra is shown.

- the measured tagged b-jet spectrum is first corrected for the b-tagging efficiency as a function of p^{det}_T and then unfolded for detector response and background fluctuations.

Figure 4 displays comparison of the spectra obtained by the two scenarios. As it can be observed, they are in agreement with each other, suggesting that both scenarios can be applied in p-Pb collisions.

4. Summary

Study of the performance of the b-jet tagging algorithm based on displaced secondary vertices with MC simulation of p-Pb events for ALICE detector in the jet p_T range $20 < p_{T,jet} < 50$ GeV/c was presented.

As discriminating variables, secondary vertex dispersion and the significance of flight distance in a transverse plane were chosen. The working point, selected by cuts on discriminating variables, offers b-jet efficiency at the level 20%, suppressing light-flavour jets contamination by two orders of magnitude. Thus, purity of this selection should be also satisfying. The tagging purity itself is not discussed here.

Corrections for detector response and background fluctuations were studied. It was found that the b-jet spectrum can be corrected with a detector response matrix for inclusive jets. Furthermore, systematic influence of the correction order is minimal.

Other ways to reduce the background are being studied, for example the rejection of tracks with V0 topology. To stabilize performance of the algorithm, study of different cuts for different jet transverse momentum is going, as well as estimation of efficiency with data-driven methods.

5. Acknowledgment

This work was supported by grant number LG15052 of Ministry of Education, Youth and Sports of Czech Republic and by Grant Agency of the Czech Technical University in Prague, grant No. SGS16/242/OHK4/3T/14.

References

[1] Y. L. Dokshitzer, D. E. Kharzeev, Phys. Lett. **B519**, 199 (2001).

[2] N. Armesto, C. A. Salgado, U. A. Wiedemann, Phys. Rev. **D69**, 114003 (2004).

[3] ALICE Collaboration, B. Abelev et al., Int. J. Mod. Phys. **A29**, 1430044, (2014).

[4] V. Khachatryan *et al.* [CMS Collaboration], arXiv:1510.03373 (2015).

[5] T. Sjoestrand, S. Mrenna, P. Skands, JHEP **05**, 026 (2006);
P. Z. Skands, Phys. Rev. **D82**, 074018, (2010).

[6] X.N. Wang, M. Gyulassy, Phys.Rev. **D44**, 3501, (1991).

[7] R. Brun, F. Carminati, CERN Program Library Long Writeup W5013, (1993).

[8] S. Chatrchyan *et al.* [CMS Collaboration], JHEP 04 (2012) 084.

[9] J. Adam *et al.* [ALICE Collaboration], Phys. Lett. **B749**, 68 (2015).

[10] M. Cacciari, G. P. Salam, Phys. Lett. **B641**, 57, (2006).

[11] S. Chatrchyan *et al.* [CMS Collaboration], JHEP **1208**, 130, (2012).

[12] A. Hocker, V. Kartvelishvili, Nucl. Instrum. Meth. **A372**, 469, (1996).

EPJ Web of Conferences will be set by the publisher
DOI: will be set by the publisher

Performance of the ALICE secondary vertex b-tagging algorithm

G. Eyyubova[1,2,a] and L. Kramarik[1,b] on behalf of the ALICE collaboration

[1] *FNSPE, Czech Technical University in Prague*
[2] *SINP MSU, Russia*

Abstract. The identification of jets originating from beauty quarks in heavy-ion collisions is important to study the properties of the hot and dense matter produced in such collisions. A variety of algorithms for b-jet tagging was elaborated at the LHC experiments. They rely on the properties of B hadrons, i.e. their long lifetime, large mass and large multiplicity of decay products. In this work, the b-tagging algorithm based on displaced secondary-vertex topologies is described. We present Monte Carlo based performance studies of the algorithm for charged jets reconstructed with the ALICE tracking system in p-Pb collisions at $\sqrt{s_{\rm NN}} = 5.02$ TeV. The tagging efficiency, rejection rate and the correction of the smearing effects of non-ideal detector response are presented.

1 Introduction

Jet reconstruction provides access to the kinematics of partons produced in hard scatterings in the initial stage of heavy-ion collisions and that later suffer energy loss in the medium via gluon radiation and elastic collisions. Reconstructed jets are therefore a powerful tool to study the properties of the quark-gluon plasma (QGP) created in heavy-ion collisions at high energy. The parton energy loss in the QGP depends on the colour charge and mass of the parton. Due to the larger colour charge factor for gluons, energy loss via gluon radiation should be larger for gluon jets than quark jets. For heavy quarks it is expected that radiative energy loss is suppressed due to coherence effects [1, 2]. This should lead to a smaller modification of the transverse momentum spectra for particles containing heavy quarks than for inclusive charged hadrons. On the other hand, for heavy quarks in the QGP, collisional energy loss may be important at low transverse momentum $p_{\rm T}$. The jet quenching phenomenon and the properties of produced matter can be further understood by measuring beauty jets at low jet transverse momentum in comparison with that of light-flavour jets [3].

The ALICE detector [4] is capable to discriminate jets originating from b quarks with different tagging algorithms. Here, we study the performance of the b-jet tagging algorithm based on displaced secondary-vertex topologies for p-Pb collisions at $\sqrt{s_{\rm NN}} = 5.02$ TeV. The p-Pb collisions serve as a test for cold nuclear effects which are important in measurements of jet quenching in Pb-Pb collisions. The study is based on Monte Carlo (MC) simulations.

[a] e-mail: Gyulnara.Eyyubova@fjfi.cvut.cz
[b] e-mail: Lukas.Kramarik@cern.ch

2 Analysis details

In this analysis we use MC with simulated responses of ALICE detector by GEANT3 [5] for p-Pb collisions at $\sqrt{s_{\mathrm{NN}}} = 5.02$ TeV. A MC simulation for pp collisions at $\sqrt{s} = 5.02$ TeV with a Lorentz boost to get the same rapidity shift as in p-Pb collisions is used to study detector response for jets without underlying event. PYTHIA6, with tune Perugia 2011 [6], is employed for MC pp simulations. The MC for p-Pb collisions is represented by a cocktail of event generators PYTHIA6 (Perugia 2011) + HIJING [7] which correspond to hard physics and p-Pb background, respectively.

Schematically, the analysis of b jets can be represented by the following analysis steps: track selection suitable for b-tagging, jet reconstruction from these tracks and underlying background subtraction under the jet area, tagging with a particular algorithm and, finally, corrections of jet spectrum. Corrections of the raw tagged spectrum $\frac{\mathrm{d}N^{\mathrm{tag}}}{\mathrm{d}p_{\mathrm{T}}}$ have to be made for detector effects (unfolding) and for tagging efficiency and purity. In case of p-Pb collisions, unfolding also includes a correction for fluctuations of the underlying background under the jet area.

The efficiency of b-tagging, ϵ_{b}, and the purity, f_{b}, are defined as the fraction of "true" b jets after tagging w.r.t total number of "true" b jets before tagging and w.r.t. total number of tagged jets, respectively. In order to estimate the efficiency and the purity, we use the "true" underlying flavour of a jet, which can be identified in MC by different labelling methods. The performance of the tagging algorithm is investigated via mistagging rate, which is the efficiency of mistakenly tagging as beauty a jet originating from a c-quark or a light-flavour parton. Mistagging rate studies are needed to extract sample with high purity of b jets. High purity allows to suppress the contamination of light-flavour and charm jets, which is important since the measured fraction of b jets to inclusive jets is at the level of 2-4% (as measured by CMS experiment), both in pp collisions at $\sqrt{s} = 7$ TeV [8] and in p-Pb collisions at $\sqrt{s_{\mathrm{NN}}} = 5.02$ TeV [9]. Below, we discuss the analysis steps in more details.

2.1 Track selection

In the MC simulations, charged tracks are reconstructed with simulated responses of Inner Tracking System (ITS) and Time Projection chamber (TPC) in a pseudorapidity region $|\eta| < 0.9$ and transverse momentum $0.15 < p_{\mathrm{T}} < 100$ GeV/c. The track selection is optimized for the reconstruction of beauty jets. The main track cuts are the minimum number of points in the TPC (70 out of 159) and the maximum distance of closest approach to primary vertex (in xy-plane and in z direction). Tracks are also required to have at least one point in the Silicon Pixel Detector (SPD). Because of inefficient regions in the SPD, the azimuthal distribution of these high-quality tracks is not completely uniform. This anisotropy is compensated by considering in addition tracks without reconstructed track points in the SPD. Track fit for these tracks is not constrained to the primary vertex. For the tracks used for secondary vertex reconstruction in jets, the point in SPD is required.

2.2 Jet reconstruction and background estimation

For the estimation of the background density and fluctuations in jet reconstruction, we use a similar approach as it was applied by ALICE for charged jet measurements in p-Pb collisions [10]. Namely, the anti-k_{T} algorithm from the FastJet package [11] with resolution parameter of $R = 0.4$ is used to reconstruct charged jets. We use the CMS method [12], which is suited for more sparse environment in p-Pb collisions w.r.t Pb-Pb collisions, for the calculation of the background density, ρ. The background fluctuations are calculated with a random cone approach as:

$$\delta p_{\mathrm{T}} = \sum_{i} p_{\mathrm{T},i} - A_{cone} \cdot \rho,$$

where the sum is over the track p_{T} in a cone and A_{cone} is the cone area. For more details see [10]. Only jets with jet axis in the pseudorapidity interval $|\eta_{\mathrm{jet}}| < 0.5$ are considered, which ensures that the jet is fully located in the TPC acceptance. In this study, the background fluctuations are measured with HIJING p-Pb events with particle transport through the ALICE detector. The background fluctuations under the jet area are found to be slightly smaller in the HIJING simulation than in the p-Pb data [10].

2.3 Correction for detector effects and background fluctuations

The jet momentum distribution is distorted by the detector mainly due to tracking inefficiency and momentum resolution. In order to correct for detector effects the detector simulation with GEANT is performed. Reconstructed jets at particle level without detector effects and jets at the detector level after particle transport through the ALICE detector are matched and based on it the detector response matrix is built. From the inverse response matrix and the momentum distribution at detector level one finds the true jet momentum distribution. The unfolding procedure has to be carrefully scrutinized since small perturbations in the measured distribution lead to large fluctuations in the solution. Several regularization methods exist. The Singular Value Decomposition (SVD) approach [13] is used in this performance study.

After subtracting the constant background in each event in order to correct the jet p_{T}, one has to keep in mind that the background is not necessary constant, but may differ for different jets in a given event. This is corrected statistically (not event by event) via an unfolding technique with a background fluctuation matrix $f(\delta p_{\mathrm{T}})$, where the background fluctuations δp_{T} are described in Sec. 2.2. The actual unfolding is done with a matrix which is a product of two matrices: detector response matrix and background fluctuation matrix.

2.4 Secondary vertex tagging algorithm

Due to the long life-time of B hadrons (≈ 500 μm), in most cases their decay vertex is displaced from the primary vertex of a collision. This algorithm reconstructs secondary vertices (SV) in a jet and uses their properties to discriminate b jets among lighter flavour jets. The tracks participating in SV reconstruction are tracks belonging to a jet with additional requirements: the point in the SPD (as mentioned above) and $p_{\mathrm{T,track}} > 1$ GeV/c. Only secondary vertices made of three tracks are considered. All combinations of three tracks, satisfying the requirement, are used to build secondary vertices in a jet. The quality of vertex reconstruction is characterized by the dispersion of the tracks in the vertex $\sigma_{\mathrm{vtx}} = \sqrt{d_1^2 + d_2^2 + d_3^2}$, where $d_{1,2,3}$ are the distances of the three tracks from SV. The sign of the SV flight distance is defined w.r.t. the jet direction, so that the signed length is $L = |\vec{L'}|\mathrm{sign}(\vec{L'} \cdot p_{jet})$, where $\vec{L'}$ is the SV position. The cuts on the most displaced SV found in the jet, namely SV dispersion, σ_{vtx}, and the significance of flight distance in a transverse plane, $L_{xy}/\sigma_{L_{xy}}$, are used for b-jet tagging in this analysis.

2.5 MC labelling

To assign the "true" flavour of reconstructed jets in the MC simulations, the MC event history is used. The labelling procedure is not unambiguous and is not strictly identical for different MC generators (it depends on parton shower implementation). Here, we treat a jet as coming from a beauty quark, if a B hadron was found in a cone $\Delta R < 0.7$ around jet axis. If no beauty hadron is present, but charm hadron was found in a cone $\Delta R < 0.7$, the jet is labelled as c-jet. All other jets are considered as light-flavour jets.

3 Performance of SV b-tagging algorithm

The discrimination power of the signed flight distance significance can be judged by the distribution of this variable for jets of different flavours, which is shown in Fig.1. Secondary vertices are searched in jets with $p_{\mathrm{T,jet}} > 20$ GeV/c and the most displaced vertex in a jet is considered. The larger the cut value of $L_{xy}/\sigma_{L_{xy}}$, the more light and charm jets are rejected compared to beauty jets. As mentioned above, the tagging procedure uses cuts on $L_{xy}/\sigma_{L_{xy}}$ and σ_{vtx} of SV. Different values of cuts yield different algorithm performance. For a particular algorithm an operating point is defined based on inclusive b-tagging efficiency and mistagging rate.

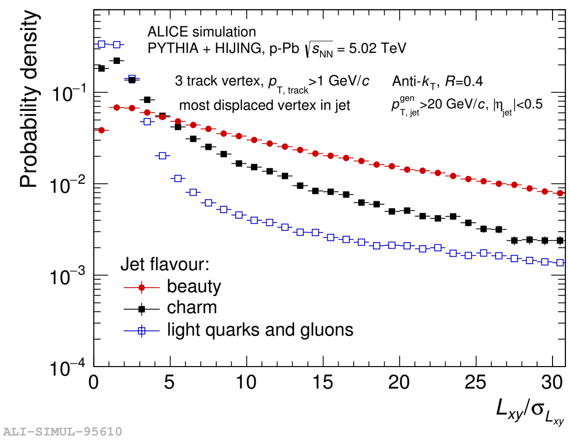

Figure 1. Probability distribution of the signed flight distance significance of the most displaced secondary vertex, found in charged jets with $p_{\mathrm{T}} > 20$ GeV/c in p-Pb simulations at $\sqrt{s_{\mathrm{NN}}} = 5.02$ TeV. The different jet flavours are assigned as described in Sec. 2.5.

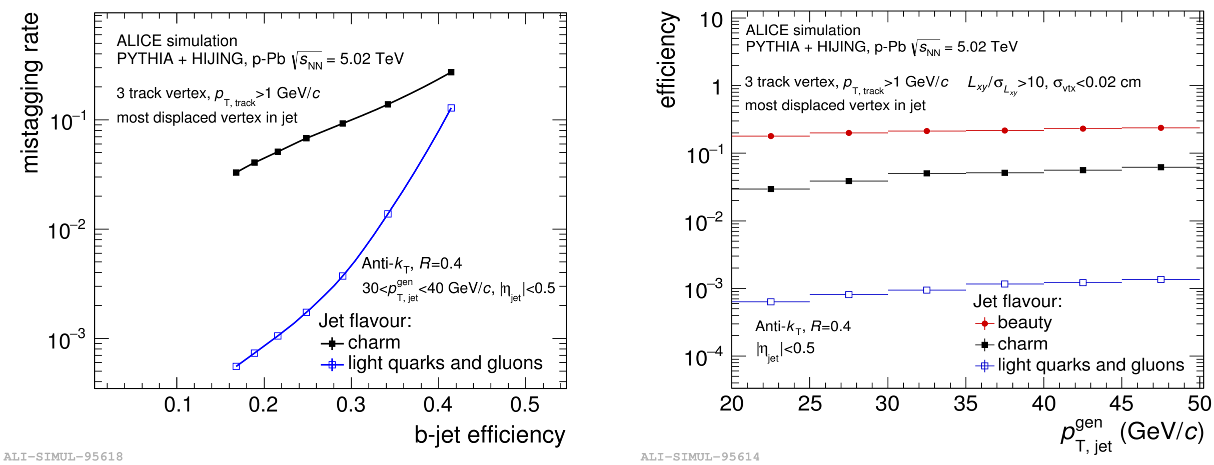

Figure 2. Left: Mistagging rate vs the b-tagging efficiency of SV tagging algorithm for different operating points for p_{T} range $30 < p_{\mathrm{T,jet}} < 40$ GeV/c. Right: The $p^{\mathrm{gen}}_{\mathrm{T,jet}}$ dependence of the b-tagging efficiency and mistagging rate for $L_{xy}/\sigma_{L_{xy}} > 10$ and $\sigma_{\mathrm{vtx}} < 0.02$ cm.

Figure 2, left, shows the mistagging rate vs the b-tagging efficiency in jet p_{T} range $30 < p_{\mathrm{T,jet}} < 40$ GeV/c for different operating points, which are obtained by varying the cuts on $L_{xy}/\sigma_{L_{xy}}$ (from 2 to 14), while the cut $\sigma_{\mathrm{vtx}} < 0.02$ cm is kept fixed. The performance may depend on $p_{\mathrm{T,jet}}$. In the considered region, $30 < p_{\mathrm{T,jet}} < 40$ GeV/c, the mistagging and tagging efficiencies are almost flat. Looser cuts result in larger statistics and higher tagging efficiency, but also higher mistagging rate, and therefore reduce purity of sample. The operation point is chosen in a way that the mistagging efficiency for light-flavour jets would be about two orders of magnitude lower than the tagging efficiency. This comes from the CMS measurements on the ratio of b jets to inclusive jets, in which the b-jet fraction was found to be at the level of 2-4% in pp collisions at $\sqrt{s}$ = 7 TeV [8]. The tagging and mistagging efficiencies $\epsilon(p_{T,jet}^{gen})$ at particle level for the chosen operating point with $L_{xy}/\sigma_{L_{xy}} > 10$ and $\sigma_{\rm vtx} < 0.02$ cm are reported in Fig. 2, right. The b-tagging efficiency is at the level 0.2. The efficiency to tag light-flavour jets is two orders of magnitude lower and the efficiency to tag charm jet is about 3 to 5 times lower than the b-tagging efficiency.

The correction for detector effects is tested with two detector response matrices: the detector response for b-jets and the one for inclusive jets. Figure 3 shows the ratio of two unfolded b-jets $p_{\rm T}$-spectra. In both cases the unfolding procedure yields similar result. This ensures that beauty and inclusive jets have similar detector response matrices and therefore the detectors response for inclusive jets can be used to unfold the tagged b-jet spectrum.

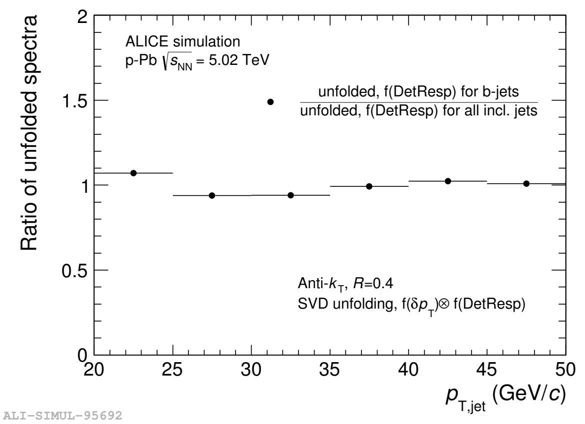

Figure 3. Comparison of SVD unfolding of b-jet spectrum with two matrices: detector matrix for inclusive jets and for b jets. Both matrices are combined with background fluctuation matrix from MC. The ratio of the two unfolded results is shown.

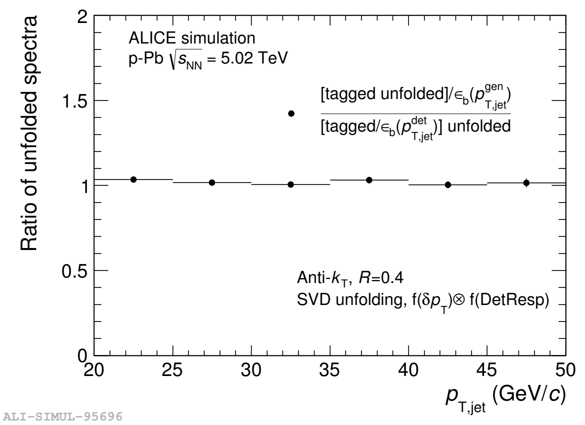

Figure 4. Comparison of two sequences of corrections: SVD unfolding and correction for tagging performance and vice versa. The ratio of the two corrected spectra is shown.

The different sequences of corrections are further studied in order to estimate the impact of background fluctuations on the stability of results. We perform the two scenarios of corrections:

1. The measured tagged b-jet spectrum is first unfolded for detector response and background fluctuations, then corrected for the b-tagging efficiency as a function of $p_{\rm T}^{\rm gen}$ (at particle level).

2. The measured tagged b-jet spectrum is first corrected for the b-tagging efficiency as a function of $p_{\rm T}^{\rm det}$ and then unfolded for detector response and background fluctuations.

The comparison of these two scenarios is shown in Fig. 4 as the ratio between the two corrected spectra. The two spectra are in agreement with each other, suggesting that both scenarios can be applied in p-Pb collisions.

4 Summary

The performance of the b-jet tagging algorithm based on displaced secondary vertices was studied with MC simulation of p-Pb events for ALICE detector. The presented results were carried out in the jet p_T range $20 < p_{T,jet} < 50$ GeV/c.

For the selected operating point the tagging efficiency is at the level 20% while the mistagging efficiency for light-flavour jets is two orders of magnitude lower, which should result in high purity of the algorithm. The rejection of tracks with V0 topology is expected to enhance the algorithm performance by reducing light-flavour contamination and is currently under investigation.

Corrections for detector response and background fluctuations were studied. It was found that the b-jet spectrum can be corrected with a detector response matrix for inclusive jets. The order of corrections (tagging efficiency vs unfolding) gives compatible results.

The tagging purity itself is not discussed here. Studies to estimate it via MC and data-driven approaches are ongoing.

5 Acknowledgment

This work was supported by the European social fund within the framework of realizing the project "Support of inter-sectoral mobility and quality enhancement of research teams at Czech Technical University in Prague", CZ.1.07/2.3.00/30.0034 and by Grant Agency of the Czech Technical University in Prague, grant No. SGS13/215/OHK4/35/14.

References

[1] Y. L. Dokshitzer, D. E. Kharzeev, Phys. Lett. **B519**, 199 (2001).
[2] N. Armesto, C. A. Salgado, U. A. Wiedemann, Phys. Rev. **D69**, 114003 (2004).
[3] J. Huang, Z. Kang, I. Vitev, Phys.Lett. **B726**, 251 (2013).
[4] ALICE Collaboration, B. Abelev et al., Int. J. Mod. Phys. **A29**, 1430044, (2014).
[5] R. Brun, F. Carminati, CERN Program Library Long Writeup W5013, (1993).
[6] T. Sjoestrand, S. Mrenna, P. Skands, JHEP **05**, 026 (2006);
P. Z. Skands, Phys. Rev. **D82**, 074018, (2010).
[7] X.N. Wang, M. Gyulassy, Phys.Rev. **D44**, 3501, (1991).
[8] S. Chatrchyan *et al.* [CMS Collaboration], JHEP 04 (2012) 084.
[9] V. Khachatryan *et al.* [CMS Collaboration], arXiv:1510.03373 (2015).
[10] J. Adam *et al.* [ALICE Collaboration], Phys. Lett. **B749**, 68 (2015).
[11] M. Cacciari, G. P. Salam, Phys. Lett. **B641**, 57, (2006).
[12] S. Chatrchyan *et al.* [CMS Collaboration], JHEP **1208**, 130, (2012).
[13] A. Hocker, V. Kartvelishvili, Nucl. Instrum. Meth. **A372**, 469, (1996).